Response and Recovery of Turbulent Pipeflow Past Square Bar Roughness Elements

by

Shubham Goswami

a thesis submitted in partial fulfilment of the requirements for the degree of

master of science

Department of MECHANICAL ENGINEERING

University of Alberta

ABSTRACT

This dissertation looks at the response and recovery of turbulent pipeflow past square bar roughness elements with two heights at Reynolds numbers of 5×10^3 and 1.56×10^5. The response of turbulent pipeflow to multiple square bar roughness elements is also evaluated at the higher Reynolds number using different Reynolds-Average-Navier-Stokes (RANS) models. Two roughness heights are considered for this study based on their relative position inside the boundary layer: $h/D = 0.05$ and 0.1, where h is the bar height and D is the pipe diameter. A validation and verification analysis enabled creating a benchmark on the performance of different RANS-based turbulence models in simulating perturbed wall bounded turbulent flows. Using $k-\varepsilon$ RANS model, which performed the best in the benchmark performance study, the effects of multiple roughness elements are examined using two separation patterns: periodic and scattered. The flow response and recovery are evaluated based on the variations in the mean and turbulent fields. It is determined that the mechanism of recovery is prolonged in the pipeflow perturbed by smaller roughness element of height $h/D = 0.05$. Increasing the number of roughness elements further prolong the flow recovery until it becomes asymptotic with three periodically separated square bars. The separation pattern of roughness elements has a negligible effect on the overall turbulent pipeflow response and recovery at a high Reynolds number. This study is then extended to the examination of viscoelastic effects on the response and recovery of turbulent pipeflow past a single roughness element with two heights using the Finitely Extensible Non-linear Elastic-Peterlin (FENE-P) rheological model incorporated into Direct Numerical Simulations (DNS) at Reynolds number of 5×10^3. These simulations revealed the importance of viscoelastic characteristics in significantly altering the overall flow response and recovery compared to Newtonian flow. The viscoelastic fluid properties correspond to a high polymer-additive concentration solution. For both bar heights examined here, the viscoelastic flow experiences significant reduction in the size of the recirculation region, which is also translated to a considerably faster recovery compared to the Newtonian flow. Moreover, the near-wall turbulence is reduced significantly due to the viscoelastic effects, which contributes to a lower wall friction, and thus, a lower drag.

PREFACE

The results from Chapter 3 are published in the Journal of Physics of Fluids with the following citation:

Goswami, S., Hemmati, A. (2020). Response of turbulent pipeflow to multiple square bar roughness elements at high Reynolds number. Physics of Fluids, 32(7), 075110.

All the simulations, data analysis and interpretation of results in this thesis were performed by Shubham Goswami under the supervision of Dr. Arman Hemmati. The simulations are completed using the resources of Compute Canada.

ACKNOWLEDGEMENTS

I convey my deepest gratitude to my advisor, Dr. Arman Hemmati for your excellent guidance, support and patience. You believed in me and guided me to rise above the ordinary and achieve the extraordinary. From working on a capstone project as an M.Eng. student, to now writing a M.Sc. dissertation, what an exciting journey it has been and it is all because of you. I feel lucky and grateful for the wonderful research environment and opportunities that I enjoyed under your tutelage and truly thankful for introducing me to this wonderful world of fluids, mathematics and physics.

I am most grateful to Mr. Suyash Verma, who provided me with much needed guidance in understanding OpenFOAM, CFD and much more. I truly appreciate your patience in teaching me and supporting me. I would have been lost without you.

Finally, I would like to thank Alberta Innovates and the Canada First Research Excellence for their generous financial support of this work.

To Mom and Dad, my brother and my love,

for your support, patience and motivation

Contents

List of Tables

List of Figures

LIST OF ABBREVIATIONS, SYMBOLS, AND NOMENCLATURE

Latin Symbols

h	Height
D	Diameter
w	separation distance
R	Radius
Re	Reynolds number
Re_τ	friction Reynolds number
Re_h	Reynolds numebr based on height (h)
k	turbulence kinetic energy
U_b	free-stream or bulk velocity
U_τ	shear of friction velocity
t	time
u	Cartesian $x-$wise velocity component
p	pressure
p_∞	free-stream pressure
x_i	Cartesian coordinate component along the i^{th} base vector
P_k	turbulence kinetic energy production
L_r	Recitculation length
C_p	Coefficient of pressure
C_f	skin friction coefficient
Wi	Weissenberg number

L^2	Polymer extensibility

Greek Symbols

δ_o	Boundary layer thickness
ε	Turbulent kinetic energy dissipation rate
ω	Turbulence specific dissipation rate
τ	Stress tensor
τ_w	Wall Shear Stress
$\dot{\gamma}$	Shear rate
η	Kolmogorov length scale
ρ	density
μ	dynamic viscosity
ν	kinematic viscosity

Other Symbols

∇	Gradient operator
$\overline{\square}$	Mean (time-averaged)
∂	Partial derivative
$\square \cdot \square$	Dot product
Δ	Difference
$\approx$	i approximately
$[\ ]^T$	Transpose
$O[\ ]$	Order of

Abbreviations

2D	Two Dimensional
CFD	Computational Fluid Dynamics
FVM	Finite Volume Method
DNS	Direct Numerical Simulation
LES	Large Eddy Simulation
DES	Detached Eddy Simulation
RANS	Reynolds Averaged Navier Stokes
SST	Shear Stress Transport
PIV	Particle Image Velocimetry
LDA	Laser Doppler Anemometery
CFL	Courant-Friedrichs-Levy Number
DRA	Drag Reducing Agent
FENE-P	Finitely Extensible Non-linear Elastic-Peterlin
SIMPLE	Semi-Implicit Method for Pressure Linked Equations
PISO	Pressure Implicit with Splitting of Operators

Chapter 1

INTRODUCTION

This study looks at the dynamics, response and recovery of pipeflow perturbed by a single and multiple square bar roughness elements using computational fluid dynamics (CFD) simulations. Two roughness element heights with $h/D = 0.05$ and 0.1 are examined at Reynolds numbers of $Re_D = \rho D U_b/\mu = 5 \times 10^3 - 1.56 \times 10^5$. This work builds on the experimental investigations of Smits et al. (2019) and Liu et al. (2019) on pipeflow past square bar roughness elements. Particularly, it looks at the the implications of roughness elements, their size and separation patterns, on reducing stresses in near-wall region and lowering turbulence levels in wall bounded flows. Furthermore, this work investigates the implications of viscoelastic or non-Newtonian polymer additives in response and recovery of pipeflow.

1.1 The Overview

Since development of the boundary layer theory by Ludwig Prandtl in 1904 (Schlichting and Gersten, 2016), there has been extensive research in the field of separated flows to characterize (Bradshaw and Wong, 1972; Kim et al., 1980; Balachandar, 1990), model (Launder and Spalding, 1983; Johnson and King, 1985; Wilcox et al., 1998a; Menter et al., 2003) and scale (Roache, 1982; Zagarola and Smits, 1998) various dynamic behaviours. The phenomenon of flow separation is commonly encountered in both internal (Simpson, 1989) and external flows (Von Kármán, 1963;

Hemmati et al., 2018). It is a subject of particular relevance to numerous practical engineering applications with respect to pressure losses, added turbulence, heat and mass transfer, and reduced rates of erosion and corrosion. Such flow dynamics find ubiquitous applications in aerodynamic flows around aircraft wings (Ravindran, 1999; Gursul et al., 2014) and turbines (Lin et al., 1991; Corten, 2001), flow around buildings (Paterson and Apelt, 1989; Baskaran and Kashef, 1996), flow over vehicles (Dominy, 1992; Hucho and Sovran, 1993; Katz, 2006; Choi et al., 2014) and in underwater marine applications (Verma and Hemmati, 2020), as well as internal flows in pipes (Shah et al., 2012; Yamagata et al., 2014; Dutta et al., 2016) and channels (Kim et al., 2001). The dynamics of flow separation due to abrupt changes in surface conditions is particularly important in studies related to the flow over forward or backward facing steps. Turbulent flow over sudden changes in surface roughness, or step change in the flow, represents a class of perturbed or non-equilibrium flow, the behavior of which is typically complex (Smits et al., 1979, 2019). The abrupt surface variations, especially in the form of step-change, creates a contraction in the flow, which leads to an overshoot in flow characteristics, such as formation of larger pressure gradients and higher Reynolds shear stresses, in the vicinity of the step change. It also results in long lasting changes in turbulent structures in the wake. The response of flow in the vicinity of the perturbation, and the recovery of the flow characteristics in the downstream wake, have motivated extended research in this field, such as channel flow dynamics (Martinuzzi and Tropea, 1993; Leonardi et al., 2003; Roussinova, 2009), flow over bluff bodies (Hussein and Martinuzzi, 1996; Wang et al., 2014; Wang and Lam, 2019), and pipeflow over wall mounted obstacles (Smits et al., 1979; Durst and Wang, 1989; Yamagata et al., 2014; Smits et al., 2019).

The flow separation due to abrupt surface changes or wall-mounted obstacles have been the focus of researchers for decades. One of the more commonly studied geometries in this field is the backward facing step. This flow is particularly attractive to researchers because it inhibits a single separation point and generates wake dynamics that is undisturbed by downstream geometrical perturbations. The step change in case of a backward facing step is considered to be a "large-step" since its height (h) surpasses the width of the boundary layer (δ_o): $h/\delta_o \gg 1$. A considerable

amount of work is done on characterizing the wake and overall flow dynamics of such large-step flow conditions: e.g., Bradshaw and Wong (1972); Vogel and Eaton (1985); Adams and Johnston (1988); Simpson (1989); Jovic and Driver (1995). However, the investigation of flow over small steps, defined as $h/\delta_o \ll 1$, have received limited attention.

Durst and Tropea (1983) and Perić and Tropea (1993) experimentally investigated the flow over backward facing step and other planer axisymmetric geometries with small-step conditions. Furthermore, Durst and Wang (1989) performed experimental and numerical study of turbulent flow over axisymmetric wall mounted thin obstacles. However, there have been only two major studies on flow over small steps (Jiménez, 2004; Smits et al., 2019), both of which were performed experimentally. Jiménez (2004) revealed that small steps act as isolated roughness elements and they cause significant changes to the downstream wake. This was expanded on by Smits et al. (2019), who performed experiments on roughness elements of two heights, $h/D = 0.05$ and 0.1, at high Reynolds number of 1.56×10^5. The work of Smits et al. (2019) was comprehensive in terms of analyzing the response and recovery of flow perturbed by roughness elements and revealed intriguing features of downstream wake. However, their experiments were limited in downstream analysis and did not fully detail the recovery. To this end, Smits et al. (2019) hinted at the need for further investigation and characterization of perturbed wall bounded flows. Moreover, there are several studies that extensively investigate the flow over multiple wall-mounted obstacles, such as Leonardi et al. (2003), Cui et al. (2003) and Leonardi et al. (2007). However, there are no comprehensive studies, to best knowledge of the author, that look at the effect of multiple tandem roughness elements ($h/\delta_o \ll 1$) in turbulent pipeflow.

This study focuses on characterizing the response and recovery of turbulent pipeflow over roughness elements of two heights ($h/D = 0.05$ and 0.1) over a range of Reynolds numbers ($Re = 5 \times 10^3 - 1.56 \times 10^5$). It addresses a major gap in literature on the lack of a quantitative characterization of downstream recovery in such flows. The study of Smits et al. (2019) hypothesized that as the flow progresses in the far-downstream region, the pipe radius (R) becomes the dominant length scale affecting the recovery mechanism. While the experimental study of Smits

et al. (2019) was limited to a small ($\sim 100h$) test section, the numerical simulations performed here are for a very long pipe ($\sim 200D$). The longer test section allows the analysis of recovery in the far-downstream region, contrary to the limited experimental test section. One of the novelties in this study involve understanding the impact of multiple tandem roughness element configurations, including their size and separation pattern, on the overall recovery in the near and far-downstream regions. The applications of multiple tandem repetitive structures are myriad, such as in sub-sea installations and as a method of passive flow control.

This work has major applications and interest in transport pipelines. Particularly, flow disturbance due to roughness elements has major contributions to improving the design of bitumen pipelines for energy transport, water sewage systems and transport systems for other fluids including slurry, water and chemicals. Especially in pipelines transporting heavy crude and petroleum products, the corrosion and erosion of pipes is a major issue (Ilman et al., 2014). Since crude and oil products are highly viscous, the shear stresses on pipe walls increase, leading to higher wall friction. Initiating abrupt flow disturbances through roughness elements inspires a novel method of dissipating near wall stresses and lowering the wall friction in the region behind the roughness element (Smits et al., 2019). Furthermore, the roughness element increases turbulence and mixing in the pipe. Such systems implemented in slurry and sewage transport pipes can induce mixing, while reducing the formation of slogs that causes blockades in pipes (Mendes et al., 1999). Long lasting changes occur in turbulence structures in the wake due to overshoot of flow response in the vicinity of the roughness (Durst and Wang, 1989; Smits et al., 2019). Such overshoot behaviour creates a long region of low skin friction behind the roughness element, leading to lower turbulence in the near-wall region (Smits et al., 2019). Periodically initiating such abrupt changes in the flow inspires a novel method of flow control to prolong the flow response and recovery, aimed at lowering drag and minimizing pressure losses.

The flow over roughness elements is also commonly encountered in the aerodynamics study of large vehicles and buildings. For example in recent years, the outer surfaces of military submarines and ship hulls are covered with anechoic tiles (Bai et al., 2019) to improve their stealth

features. Anechoic tiles are rubber or synthetic polymer tiles that absorb submarine noise, and thus reduce the distortion of their signals. The mismatch in heights of these rubber tiles, due to their placement, acts as a roughness element. Even the flow around high-rise buildings incorporate such conditions. The glass-panes of high-rise buildings are lined with rubber edge spacers or gaskets (Van Den Bergh et al., 2013). Due to contraction between two glass-panes, the rubber gaskets on the sides squeeze together and protrude out. The aspect ratios of these protrusions is the same as that of roughness elements.

The last part of this thesis focuses on the implications of viscoelastic or non-Newtonian fluid on flow disturbances associated with roughness elements and their recovery. It has been established that adding certain high molecular-weight polymers to highly viscous fluids, in different concentrations, would result in damping of turbulence, lower stresses, and reduced pressure losses (Ptasinski et al., 2001; Dubief et al., 2013; Shaban et al., 2018; Eshghinejadfard et al., 2017). Due to lower turbulence intensity, the overall frictional drag on the pipe walls is greatly reduced, which leads to a lower risk of erosion on pipe walls. These polymer additives are referred to as Drag-Reducing-Agents (DRA) and fluid containing DRAs exhibits elastic behavior combined with viscous effects, hence the name Viscoelastic fluid. This work investigates the influence of viscoelastic fluid on pipeflow over roughness elements of two heights at Reynodls number of $Re = 5 \times 10^3$. Particularly, it studies the viscoelastic effects on the flow response and recovery compared to Newtonian flow. The novelty of this work is the analysis of viscoelastic effects on small-steps or roughness elements.

Viscoelastic fluids are known to exhibit shear-thinning characteristics in certain polymer concentrations (Shaban et al., 2018). Shear thinning can be encountered in everyday life, for example in spreading of peanut butter or mayonnaise on a bread. If the peanut butter or mayonnaise is left on the bread, it hardly moves until it is spread using a knife (Macosko, 1994). This phenomenon is referred to as the "shear-thinning" process, in which viscosity of the fluid strongly depends on the applied or asserted shear stresses on the fluid. Most shear-thinning fluids are lubricating in nature. The study by Smits et al. (2019) showed that small-steps, in response to perturbation, produce

higher velocity gradients, and as a result higher turbulence in the wake. Due to high gradients produced by the roughness, the shear stress in the vicinity of the roughness increases. With viscoelastic fluids, this overshoot exerts stresses on the fluid that lead to lower stresses in the near-wall region due to shear thinning.

1.2 Motivations and Objectives

The study of different aspects of flow over wall-mounted obstacles has been the subject of research for decades (Schofield and Logan, 1990; Martinuzzi and Havel, 2000; Farhadi and Rahnama, 2006; Doolan and Moreau, 2016; Yin et al., 2020). A considerable amount of work has been done to study the characteristics of flow separation (Dimaczek et al., 1989; Jovic and Driver, 1995), formation of separation bubble (Kiya and Sasaki, 1983; Mollicone et al., 2017), reattachment of separated shear layers (Bradshaw and Wong, 1972; Kim et al., 1980), and initial flow recovery (Smits et al., 1979; Simpson, 1989) for flow over large steps, $h/\delta_o \gg 1$, where h is the height of the element and δ_0 is the boundary layer thickness. However, limited studies focus on small steps, despite their common application in various industries. Small-step conditions or roughness elements, defined as $h/\delta_o \ll 1$, involve the obstacle being immersed in the boundary layer. Such small steps have significant effects on drag production, noise generation, and the response and recovery mechanisms of the flow that are distinct compared to large steps. The lack of analysis in this area implies a major gap in literature. Furthermore, the behavior of flow in plane channel with infinite-span perturbation is different from that of pipeflows. In case of the latter, nature of the wake, flow interactions and the overall recovery of the turbulent flow is intuitively different due to axisymmetric nature of the perturbation. The flow response to axisymmetric contraction becomes quiet different from that of plane contractions, as seen experimentally by Dimaczek et al. (1989). *Thus, the first objective of this work is to analyze the response and recovery of turbulent pipeflow perturbed by axisymmetric small-step perturbations ($h/\delta_o \ll 1$) at moderate and high Reynolds numbers.*

The study of flow over multiple tandem (wall-mounted) roughness elements have been an active area of research in recent years, due to a wide range of applications in marine research (Barman et al., 2019; Yin et al., 2020), heat-transfer (Miyake et al., 2001; Akbari et al., 2015), and as a method for passive flow control (Smits et al., 2019; Liu et al., 2019). The majority of these investigations focus on the heat transfer associated with such flow, while limited studies consider the effects of flow response and recovery with such repetitive structures. Two important variables influence these flows: the number of wall-mounted structures, and the separation distance and pattern between them (Liu et al., 2019). While many past studies have investigated the effects of periodic separation in the flow over an array of wall-mounted obstacles, there is a gap in investigating the influence of separation patterns in flow over multiple tandem roughness elements. Furthermore, there are no comprehensive studies that explore the effect of the number of elements on flow recovery and response. *Hence, the second objective of this thesis is to quantify the impact of increasing the number of wall-mounted roughness elements, with different separation patterns, on the flow response and recovery*.

There are several numerically and experimentally studies that examine turbulent flow response and recovery. Experimental studies using Particle Image Velocimetry (PIV) and Laser Doppler Anemometery (LDA) involve higher Reynolds numbers, while numerical studies based on Direct Numerical Simulations (DNS), Large Eddy Simulations (LES), and Raynolds-Averaged Navier-Stokes (RANS) simulations are limited to moderate and low Reynolds numbers. Particularly, the analysis using DNS in pipeflows are limited to lower Reynolds numbers since they require large computational resources and time. Since industrial applications at high Reynolds numbers are ubiquitous, they rely on computationally inexpensive methods such RANS models. Various studies involving RANS-based turbulence models report discrepancies in predicting high pressure gradient flows(Fogaing et al., 2019). *This motivates the third objective of this thesis to benchmark the performance of four traditional RANS-based turbulence models (Standard $k-\varepsilon$, Realizable $k-\varepsilon$, $k-\omega$, and SST $k-\omega$) in predicting perturbed flows*.

The transport of heavy-oil products by pipelines constitute the safest method for displacement of energy (CAPP, 2019). Since these energy products are highly viscous, high-molecular weight polymers additives are used to attain shear-thinning in the flow, and to reduce the near wall turbulence and control the erosion of pipe walls.In engineering context, no surface is considered hydraulically smooth, even pipes and channels used in transport of oil and crude products. Thus, it is important to study the mechanism of response and recovery in viscoelastic fluid flow over roughness elements.*This constitutes the fourth objective of this thesis to quantify the implications of viscoelastic fluid on turbulent pipeflow over roughness elements at moderate Reynolds numbers (e.g.,* $Re = 5 \times 10^3$*).*

1.3 Novelty

The novelty of this study is twofold. First, it allows understanding the impact of multiple tandem roughness elements, based on their number, size and separation pattern, on the overall flow response and recovery in the near and far-downstream regions. Second, this work enables the characterization of viscoelastic effects on small-steps or roughness elements. Another major contribution of this thesis is benchmarking the performance of four different RANS models for a comprehensive study of complex turbulent pipeflows at high Reynolds numbers.

1.4 Structure of the thesis

This thesis begins with a review of the literature in Chapter 2 that focuses on a brief overview of OpenFOAM, as the main CFD platform for the simulations. This chapter also provides details on turbulence modeling and viscoelastic modeling of the flow. The methodology and procedures for achieving each objective are outlined individually per study in Chapters 3 and 4. Particularly, a description of the simulation setup and main characterization of turbulent pipflow over multiple wall-mounted square bar roughness elements at high Reynolds numbers are provided in Chapter 3. This includes a detailed review of the existing literature on non-equilibrium flow over multiple tan-

dem wall mounted perturbations. This addresses a fundamental gap in literature, which specifies the novelty of this study. A detailed validation is provided for the grid resolution, and the performance of different turbulence models are analyzed in predicting large pressure gradients past the roughness elements.

Chapter 4 describes the simulation setup and results for the study of viscoelastic fluid flow past square bar roughness element using DNS. Wake characteristics behind the roughness element, evolution of Reynolds shear stresses, distribution of surface pressure and skin friction, and comparison of turbulence energy budget terms are presented to study the implications of viscoelastic fluid in terms of flow response and recovery. The results are compared to the base simulations performed using a Newtonian flow at the same Reynolds number using a similar computational setup.

Finally, the conclusions are provided in Chapter 5, along with a discussion of the new ideas and recommended future developments to extend this study.

Chapter 2

BACKGROUND

This thesis employs Computational Fluid Dynamics (CFD) to study fundmanetal aspects of flow response and recovery in turbulent pipeflow dynamics. CFD is a branch of fluid mechanics that uses numerical analysis and data structures to solve or approximate the governing equations of fluid motion, i.e., Navier-Stokes equations. High Performance Computation (HPC) systems are used to perform complex mathematical calculations for fluid flows bounded by boundary conditions. The computational results are then validated against targeted experiments or analytical solutions[1]. Most CFD codes utilize Finite Volume Method (FVM), where the system of equations are solved by discretizing the domain into various control volumes, or what is referred to as "mesh". FMV has advantages in memory usage and solution speed, especially for large problems such as solving high Reynolds number turbulent flows. Various commercial and open-source CFD packages are available. Commercial packages include robust CFD toolboxes such as ANSYS CFX, ANSYS Fluent, STAR-CCM+, Polyflow and COMSOL Multiphysics. Open-source CFD codes include OpenFOAM, SU[2] and Fire Dynamics Simulator. In the studies discussed in this thesis, OpenFOAM is used as the main platform to complete CFD simulations.

[1] Analytical or empirical solutions are not available for complex flow phenomenons.

2.1 OpenFOAM

Open Field Manipulation and Operation (OpenFOAM) was originally developed by Jasak (1996) at the Imperial Collage London, and further expanded by Weller et al. (1998). It is an open-source, finite volume method framework for computational fluid dynamics supporting polyhedral meshes. OpenFOAM consists of a bundle of $C++$ libraries and codes to solve complex fluid flow phenomena such as turbulence, combustion, magneto-hydrodynamics, chemical reaction and many more. It also consists of pre- and post-processing applications employed for mesh generation, field manipulation, field decomposition and data sampling. OpenFOAM applications are divided into two main categories: *solvers* and *utilities*. Solvers perform calculations in solving the flow equations, while utilities provide a range of pre- and post-processing functionalities.

One of the key feature of OpenFOAM is its extensibility. The source code is built on $C++$ and object oriented programming, and the architecture is available freely as an open-source code. Because of object-oriented programming, the implemented equations and solvers are easier to understand. For example, fluid flow momentum equation such as,

$$\frac{\partial \rho \mathbf{u}}{\partial t} \; + \; \nabla \cdot \varphi \mathbf{u} \; - \; \nabla \cdot \mu \nabla \mathbf{u} \; = \; -\nabla p, \tag{2.1}$$

is represented by the code as,

```
solve
(
          fvm::ddt(rho, U)
        + fvm::div(phi, U)
        - fvm::laplacian(mu, U)
          ==
        - fvc:grad(p)
)
```

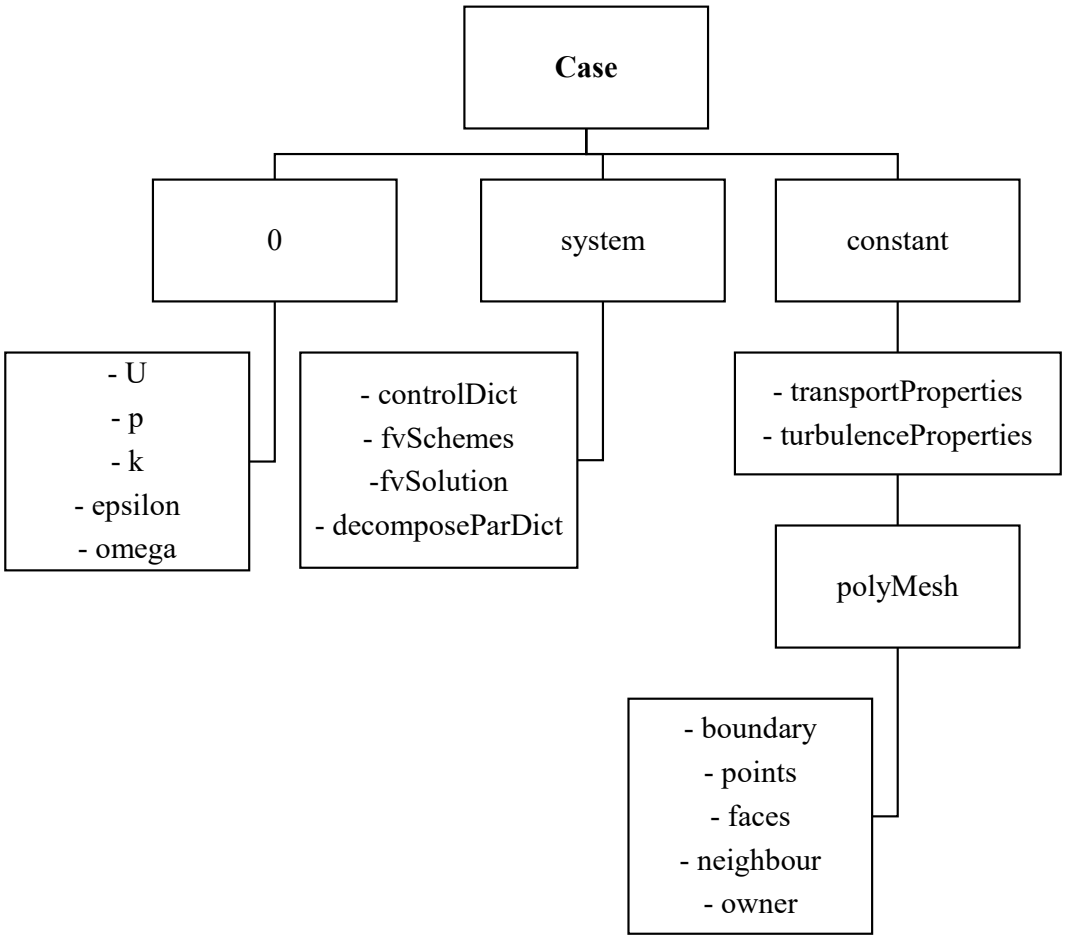

Figure 2.1: Case structure in OpenFOAM

One of the disadvantages of OpenFOAM is a lack of Graphics User Interface (GUI). It works using a structure of input files for each case, as shown in Figure 2.1. Here, the case is divided in to three directories:

- "*0*" is a time directory containing initial and boundary conditions required for the simulation, along with individual files containing the data for particular fields such as velocity ("U"), pressure ("p"), etc.

- "*system*" directory contains the setting parameter files associated with the solution procedure. It should have at least 3 files: "*controlDict*", where the simulation control parameters are defined including start/end time and time step; "*fvSchemes*", where the discretization schemes are set; "*fvSolution*", where the algorithm and solver tolerances are set.

- "*constant*" directory contains the files describing the fluid properties and specifying turbulence modelling. It also contains the full description of the domain mesh in a sub-directory named "*polyMesh*".

OpenFOAM contains an impressive range of solvers, including simpleFoam and pimpleFoam, which are mainly used in this thesis. SimpleFoam solver is a steady-state solver for incompressible turbulent flow, incorporating the SIMPLE (Semi Implicit Pressure Linked Equation) algorithm (OpenCFD, 2019) that is utilized in Chapter 3. PimpleFoam solver is utilized in Chapter 4, which is a transient solver for incompressible, turbulent flow incorporating the PIMPLE (combination of Pressure-Implicit with Splitting of Operators, PISO, and SIMPLE) algorithm (OpenCFD, 2019).

2.2 Turbulence Modeling

Simulations in Chapter 3 utilize different RANS-based turbulence models, detailed formulations of which are provided here. It is computationally expensive to resolve a wide range of time and length scales observed in turbulent flows at high Reynolds numbers. Any flow variable (φ) can be decomposed into mean ($\overline{\varphi}$) and fluctuating (φ') components as follows,

$$\varphi(x_i,t) \;=\; \overline{\varphi}(x_i,t) \;+\; \varphi'(x_i,t), \tag{2.2}$$

Reynold-Averaged Navier-Stokes (RANS) turbulence model aims to solve the mean flow variable ($\overline{\varphi}$), and the ensemble average term appearing in the equation above is defined as (George, 2013),

$$\overline{\varphi}(x) \;=\; \lim_{T\to\infty} \; \frac{1}{T}\sum_{i=1}^{T} \; \varphi_i(x,t), \tag{2.3}$$

where T is the averaging interval.

The final form of the governing equations following the implementation of Reynolds decomposition and averaging give the equations below, which are referred to as Reynolds-Averaged Navier-

Stokes equations or simply RANS equations:

$$\frac{\partial \overline{\boldsymbol{u_i}}}{\partial x_i} = 0, \tag{2.4}$$

$$\overline{\boldsymbol{u_j}}\frac{\partial \overline{\boldsymbol{u_i}}}{\partial x_j} = -\frac{1}{\rho}\frac{\partial \overline{p}}{\partial x_i} + \nu\frac{\partial \overline{\boldsymbol{u_i}}}{\partial x_i \partial x_j} - \frac{\partial \overline{\boldsymbol{u_i}'\boldsymbol{u_j}'}}{\partial x_j}, \tag{2.5}$$

Here, Eq. 2.5 can be rewritten as,

$$\rho\left(\overline{\boldsymbol{u_j}}\frac{\partial \overline{\boldsymbol{u_i}}}{\partial x_j}\right) = \frac{\partial}{\partial x_j}\left[-\overline{p}\delta_{ij} + \mu\left(\frac{\partial \overline{\boldsymbol{u_i}}}{\partial x_j} + \frac{\partial \overline{\boldsymbol{u_j}}}{\partial x_i}\right) - \rho\overline{\boldsymbol{u_i}'\boldsymbol{u_j}'}\right], \tag{2.6}$$

where the term in square brackets represents the sum of three stresses: $\overline{p}\delta_{ij}$ from the mean pressure field, viscous stress, and *Reynolds shear stress* ($-\overline{u_i' u_j'}$), which is defined in a tensor form as,

$$\boldsymbol{\tau}_{ij} = -\overline{\boldsymbol{u_i}'\boldsymbol{u_j}'} = \begin{bmatrix} -\overline{u_x' u_x'} & -\overline{u_x' u_y'} & -\overline{u_x' u_z'} \\ -\overline{u_y' u_x'} & -\overline{u_y' u_y'} & -\overline{u_y' u_z'} \\ -\overline{u_z' u_x'} & -\overline{u_z' u_y'} & -\overline{u_z' u_z'} \end{bmatrix} \tag{2.7}$$

This gives rise to the problem of closure in turbulence, where the number of equations do not match the number of variables. In order to "Close" the RANS equations (e.g., Eq. 2.6), τ_{ij} term is modeled using a combination of Boussinesq and Eddy viscosity approximations. The methods of estimating, or modeling, stress tensor parameters differs between turbulence models and may be the source of their accuracy or the lack of it.

In the context of this dissertation, four two-equation turbulence models are tested, including Standard k$-\varepsilon$, Realizable k$-\varepsilon$, k$-\omega$, and SST k$-\omega$ model using OpenFOAM. The initial conditions and transport equations of these turbulence models, as implemented in OpenFOAM(OpenCFD, 2019), are described below. These turbulence models are solved using SIMPLE algorithm, that allows steady-state approximations of governing equations using iterative procedure.

2.2.1 Initial Conditions

Accoridng to Vold (2017), the turbulent kinetic energy (k) for isotropic turbulence can be estimated by:

$$k = \frac{3}{2}(I \ u_\infty)^2, \tag{2.8}$$

where I is the turbulence intensity, and u_∞ is the free-stream velocity. Similarly, the turbulence dissipation rate (ε) can be estimated by:

$$\varepsilon = \frac{C_\mu{}^{\frac{3}{4}} \ k^{\frac{3}{2}}}{L}, \tag{2.9}$$

where C_μ is a model constant equal to 0.09 and L is turbulent length scale, given as $L = 0.038D$ where D is the hydraulic diameter of the pipe. Finally, the turbulence specific dissipation rate (ω) is estimated by:

$$\omega = \frac{C_\mu{}^{\frac{-1}{4}} \ k^{\frac{1}{2}}}{L}. \tag{2.10}$$

2.2.2 Standard k$-\varepsilon$ Model

For the Standard k$-\varepsilon$ mode, the turbulence kinetic energy equation is given as (Cappelli and Mansour, 2013a),

$$\frac{\partial}{\partial x_i}(k\overline{\boldsymbol{u_i}}) = \frac{\partial}{\partial x_i}\left(\frac{\nu_t}{\sigma_k}\frac{\partial k}{\partial x_i}\right) + P_k - \varepsilon, \tag{2.11}$$

where the turbulence kinetic energy dissipation rate is determined by

$$\frac{\partial}{\partial x_i}(\varepsilon\overline{\boldsymbol{u_i}}) = \frac{\partial}{\partial x_i}\left(\frac{\nu_t}{\sigma_\varepsilon}\frac{\partial \varepsilon}{\partial x_i}\right) + \frac{C_1\varepsilon}{k}\left(P_k + C_3\frac{2}{3}k\frac{\partial \boldsymbol{u_i}}{\partial x_i}\right) - C_2\frac{\varepsilon^2}{k}. \tag{2.12}$$

Here, ν_t is the eddy viscosity, defined as $\nu_t = C_\mu \frac{k^2}{\varepsilon}$, and C_1, C_2, C_3, σ_k and σ_ε are model closure coefficients, the values for which are,

$$C_1 = 1.44;\ \ C_2 = 1.92;\ \ C_3 = 0.0;\ \ \sigma_k = 1.0;\ \ \sigma_\varepsilon = 1.3. \tag{2.13}$$

2.2.3 Realizable k$-\varepsilon$ Model

The transport equations for the Realizable k$-\varepsilon$ Model remain the same as Equations 2.11 and 2.12, while the formulations for closure constants are changed as follows (Cappelli and Mansour, 2013a):

$$C_\mu \ = \ \frac{1}{A_0 + \frac{kU_\infty}{\varepsilon}}, \tag{2.14}$$

where $A_0 = 4.0$, and the other model constants are given as (Cappelli and Mansour, 2013a):

$$C_1 = 1.44;\ \ C_2 = 1.9;\ \ C_3 = 0.0;\ \ \sigma_k = 1.0;\ \ \sigma_\varepsilon = 1.2. \tag{2.15}$$

2.2.4 Standard k$-\omega$ Model

One of the two traditional RANS models is the Standard k$-\omega$ Model. Here, the transport equation for k remains the same as Equation 2.11, while the equation for turbulence specific dissipation rate (ω) is given as,

$$\frac{\partial}{\partial x_i}(\omega \overline{u_i}) \ = \ \frac{\partial}{\partial x_i}\left[(\nu + \alpha_\omega \nu_t)\frac{\partial \omega}{\partial x_i}\right] \ + \ \alpha \frac{\omega}{k}\nu_t P_k \ - \ \beta\omega^2 \ + \ \frac{2\nu_t}{\sigma_{\omega k}}\frac{\partial \omega}{\partial x_i}\frac{\partial k}{\partial x_i}. \tag{2.16}$$

Here, the closure model coefficients are given as,

$$\alpha_\omega = 0.5;\ \ \alpha = 0.52;\ \ \beta = 0.072. \tag{2.17}$$

2.2.5 SST k$-\omega$ Model

The Shear Stress Transport (SST) k$-\omega$ model combines the k$-\omega$ and k$-\varepsilon$ models. In the near-wall region, k$-\omega$ model is used, while in the fully turbulent regions, k$-\varepsilon$ model is used for modeling the flow. Here, the transport equation for k and ω remain the same as Eqs. 2.11 and 2.16, respectively, while more closure coefficients are added to properly model the last term of Equation 2.16 (Cappelli and Mansour, 2013a):

$$\alpha_{\omega 1} = 0.5;\ \ \alpha_{\omega 2} = 0.856;\ \ \alpha_{k1} = 0.85;\ \ \alpha_{k2} = 1;\ \ \beta_1 = 0.072;\ \ \beta_2 = 0.0828;$$
$$\beta^* = 0.09;\ \ a_1 = 0.31;\ \ b_1 = 1. \qquad (2.18)$$

2.3 Viscoelastic Modeling

Simulations in Chapter 4 utilize DNS along with constitutive equations to model the rheological properties of the viscoelastic polymer-additives. A brief description of formulations and viscoelastic models is provided here.

Most metals exhibit linear elastic behaviour when subjected to low intensity stresses, while at high intensities of stress they undergo plastic deformation. For elastic material, the normal stress (σ) is the function of normal strain (ε), given as $\sigma = \sigma(\varepsilon)$. A similar relationship exists between shear stress (τ) and shear strain ($\dot{\gamma}$) (Hooke, 1678). A separate group of materials exist, such as some plastics, biological materials and some metals, that exhibit gradual deformation and recovery when subjected to loading and unloading (Macosko, 1994). This behaviour is dependent on how quickly the loads are applied and removed (called relaxation time), and the extent of deformation is the function of the rate at which the deformation-causing loads are applied. Such time-dependent behaviour is called viscoelasticity. A viscoelastic material possesses both viscous and elastic behaviour. For such material, the stress (σ) is not only the function of strain (ε), but it

is also a function of strain-rate ($\dot{\varepsilon}$), defined as

$$\boldsymbol{\sigma} \;=\; \sigma(\varepsilon, \dot{\varepsilon}) \tag{2.19}$$

The governing equations for incompressible viscoelastic fluid are continuity and momentum equations (Balasubramanya et al., 2016):

$$\nabla \cdot \boldsymbol{u} \;=\; 0, \tag{2.20}$$

$$\frac{\delta \rho \boldsymbol{u}}{\delta t} + \nabla \cdot (\rho \boldsymbol{u}\boldsymbol{u}) - \nabla \cdot \boldsymbol{\tau_s} \;=\; -\nabla \cdot p + \nabla \cdot \boldsymbol{\tau_p}, \tag{2.21}$$

where, using the split-stress-tensor approach the stress tensor is split into Newtonian ($\boldsymbol{\tau_s}$) and Non-Newtonian ($\boldsymbol{\tau_p}$) components: $\boldsymbol{\tau} = \boldsymbol{\tau}_s + \boldsymbol{\tau}_p$. The Newtonian stress contribution is defined as,

$$\boldsymbol{\tau_s} = 2\eta \boldsymbol{D}, \tag{2.22}$$

and D is the deformation-rate tensor, given as (Balasubramanya et al., 2016),

$$\boldsymbol{D} = \frac{1}{2}\left(\nabla \cdot u + \mid \nabla \cdot u \mid^T\right). \tag{2.23}$$

The non-Newtonian stress component is defined in multi-mode form as (Balasubramanya et al., 2016),

$$\sum_{k=1}^{n} \boldsymbol{\tau}_{pk} = 0, \tag{2.24}$$

where the symmetric tensor ($\boldsymbol{\tau}_{pk}$) is obtained from the sum of contributions of individual relaxation modes. Constitutive relations are required to calculate the polymeric stress tensor in Equation 2.24 and model the rheological properties of viscoelastic fluid.

Finitely Extensible Non-linear Elastic - Peterlin (FENE-P) model is one such constitutive model utilized in Chapter 4 along with direct numerical simulations. Detailed description and formulations of FENE-P model are provided in Section 4.3.

Chapter 3

MULTIPLE ROUGHNESS ELEMENTS

3.1 Introduction

The response and recovery of turbulent pipeflow over multiple square bar roughness elements with periodic and staggered patterns are examined at Reynolds number of 1.56×10^5. The square bar roughness elements have a height of $h/D = 0.05$ and 0.1. Two, three and four periodically separated bar elements are considered using the smaller height of 0.05, along with one with staggered separation between four tandem elements. The results and discussions provided in this chapter provide a benchmark on performance of RANS-based models, which is then used as a tool to provide insight into the implications of multiple bar roughness elements on response and recovery of turbulent pipeflow. This chapter addresses the first three objectives of the thesis outlined in Section 1.2. This Chapter is prepared in such a way that the problem description in Section 3.3 is followed by the numerical validation in Section 3.4 and the results in Section 3.5. A summary of the main conclusions are outlined in Section 3.6.

3.2 Background

The abrupt pipe surface variations at high Reynolds number constitutes a class of non-equilibrium flows that have not received sufficient attention in recent years. These types of flow have exten-

sive engineering applications for example in marine vehicles, such as ships and submarines, aerial vehicles, high-speed trains, and even buildings inside an atmospheric boundary layer. Energy and fluid transport through pipes and ducts also involve similar turbulent flow over rough surfaces. In engineering context, even ducts or pipes cannot be regarded as hydraulically smooth (Langelandsvik et al., 2008), especially at high Reynolds numbers. The behavior of non-equilibrium and perturbed flows is typically complex, since perturbations or step changes cause contraction in the flow and significant turbulent variations. This has motivated several numerical and experimental studies on the mean flow features and flow response to abrupt changes to surface conditions in various applications (Smits et al., 2019; Durst and Wang, 1989; Yamagata et al., 2014; Leonardi et al., 2003; Morrison et al., 1993; Shah et al., 2012; Kaneda et al., 2003; Van Buren et al., 2019; Jiménez, 2004; Durst et al., 1989; Nygård and Andersson, 2013; Smits et al., 1979).

The numerical studies on flow over abrupt changes to the surface of a pipe involve Direct Numerical Simulations (DNS) (Leonardi et al., 2003; Nygård and Andersson, 2013), Large Eddy Simulations (LES) and Reynolds-averaged Navier-Stokes (RANS) models (Cappelli and Mansour, 2013b). The experiments using Particle-Image-Velocimetry (PIV) (Smits et al., 2019) and Laser-Doppler-Anemometry (LDA) (Durst et al., 1989) focus on flows at a higher range of Reynolds number: $Re_D = U_b D/\nu = 10^4 - 10^6$, where U_b is the bulk velocity and D is the hydraulic diameter. The extensive computational requirements for detailed numerical analysis, such as DNS, intuitively limit the range of Re considered in these studies, while LES and RANS models are alternatives that enable simulations at higher ranges of Re, i.e., 10^4 to 10^6. However, the results from LES and RANS exhibit discrepancies compared to the experimental studies. These are attributed to the numerical modeling effects, the most important of which is the turbulence modeling technique (Hemmati et al., 2018). Fogaing et al. (2019) examined the performance of different RANS and Unsteady RANS models in simulating turbulent flow past a normal flat plate. They identified that in the presence of large pressure and velocity gradients, unsteady RANS models perform better than steady RANS models. This is particularly valid if the flow is inhiritely unsteady, similar to the wake of a normal plate at moderate Reynolds numbers. However, discrepancies were observed in

comparison to DNS. In cases without the large pressure gradients and unsteady behavior, however, the RANS models may be performing satisfactorily.

There were several studies on perturbed and non-equilibrium flows that investigated different aspects of the flow physics. Smits et al. (1979) investigated the effects of change in surface conditions, such as the introduction of a short region of concave curvature, on the flow response and recovery. It was determined that the flow displayed a second-order response due to interaction between shear stress and mean shear, which caused a rapid amplification of Reynolds stresses followed by a long lasting collapse. This indicated that such abrupt changes in the flow causes long lasting changes in turbulent structure. Later, Durst and Wang (1989) experimentally and numerically studied turbulent pipeflow with a thin and thick wall-mounted ring-type obstacle over a range of Reynolds numbers. Experiments were carried out using LDA and simulations were based on the Standard $k-\varepsilon$ RANS model. The results indicated that there exists an overshoot of flow response in the vicinity of the obstacle with longer reattachment lengths compared to flows with sudden expansion. This overshoot extended to downstream of the obstacle before a sudden decay in Reynolds stresses. The $k-\varepsilon$ model predicted the flow features in good agreement with experiments. Later on, Jiménez (2004) investigated the effects of turbulent flow over rough walls, concluding that small steps (defined by $h/\delta_0 \ll 1$, where h is the step height and δ_0 is the boundary layer thickness) cause significant changes in the flow by behaving as isolated roughness elements. More recently, Smits et al. (2019) expanded this study by quantifying the response and recovery of the flow perturbed by a roughness element, introducing it as a novel method for flow control. Using PIV to study the flow over two bar height elements with $h/D = 0.05$ and 0.1 at $Re = 1.56 \times 10^5$, Smits et al. (2019) identified that the flow did not recover fully within the measurement domain of $100h$ at such high Re. The Reynolds shear stresses near the roughness element were amplified and their collapse was slow, which led to a long recovery process. The distributions of shear stress portrayed a large turbulent diffusion away from the wall, which hints at a mechanism of passive flow control. Furthermore, this study observed a longer reattachment length compared to flows over backward facing step at similar Reynolds numbers. The sudden contraction and expansion

of the incoming flow, due to presence of the square bar roughness element, resulted in a longer reattachment length. Similar observations were also reported by Dimaczek et al. (1989) Dimaczek et al. (1989), who investigated the turbulent flow over two-dimensional plane and axisymmetric surface-mounted obstacles at $Re_h = U_b h/\nu = 5 \times 10^3 - 5 \times 10^4$, where h is the obstacle height. They determined that the reattachment lengths obtained by different geometries were influenced by the state of the upstream flow.

Leonardi et al. (2003) studied the flow response over an array of wall mounted square bars separated by rectangular cavities to determine the effects of flow separation and their response under adverse downstream pressure gradients. Three roughness heights were studied ($k/H = 0.1, 0.15$ and 0.2, where H is the half-height of channel) over a range of cavity width to roughness height ratios. They determined that for a large enough ratio, the reattachment length is altered by an adverse pressure gradient imposed by the vertical downstream wall of the roughness element. Hemmati et al. (2019) observed a similar behavior while investigating the relation between surface pressure distribution and wake characteristics for a thin flat plate. Further, they identified that the flow only starts experiencing adverse pressure gradients downstream of the center of the separation zone. This flow behavior is also observed in pipeflows with thin wall-mounted perturbations with a wide range of application in fluid systems such as orifice-type flow meters. Orifice-type flow meter is widely used in the energy industry (Sifferman et al., 1989), which operates based on a sudden contraction and expansion of the flow. This leads to a sudden change in pressure across the orifice along with a separation that need to be captured properly to characterize the flow. The design and operation of such systems in the energy industry rely on computationally inexpensive methods such as RANS modeling (Yamagata et al., 2014; Shah et al., 2012; Eiamsa-ard et al., 2008).

Yin et al. (2020) studied the flow over two square and trapezoidal wall-mounted structures in tandem on a horizontal flat wall at $Re = 1.19 \times 10^5$ using Shear Stress Transport (SST) k$-\omega$ model. They studied the influence of separation ratio between two structures, and the effects of slope angles of the side walls on hydrodynamic quantities such as drag and lift coefficients. A range of separation ratios were studied, which identified that the flow had an impinging effect

on subsequent structures with smaller separation distance. Due to this impinging influence of the primary structure, the recirculation length behind the subsequent structure was significantly shorter. Cui et al. (2003) investigated the effects of $d-$type roughness, $k-$type roughness and an intermediate roughness in a channel with transverse wall mounted ribs on one wall using LES. The fundamental difference between the two types of roughness is related to the separation distance between the two ribs. The $d-$type roughness has a separation that equals the rib height, while the $k-$type roughness has a longer separation between two elements. This study found that the mean flow features, such as recirculation, reattachment and mean velocity, show significant differences between $d-$type and $k-$type rib arrangements. Such abrupt changes caused prolonged effects, which propagated in far-downstream regions. Similar findings were reported by Leonardi et al. (2007) on the properties of flow over $d-$type and $k-$type roughness, which provided insight into the significant differences in pressure drag and stresses.

In recent years, there has been several studies that investigated the effects of abrupt step-change and wall-shape change on large scale motions and very large scale motions in pipe flow. These motions and entailing secondary structures constitute a large fraction of Reynolds shear stresses and flow recovery (Balakumar and Adrian, 2007). Van Buren et al. (2017) investigated the response of turbulent pipe flow to abrupt changes in pipe shape, designed to manipulate large scale and very large scale motions. The outcome of this study showed that manipulation of near-wall flow structures could lead to lower turbulence and lower skin friction near the wall. The large scale motions and very large scale motions generated, transverse far in the downstream region, prolonging the recovery mechanism. Similarly, Chan et al. (2018) investigated the effects of wall mounted sinusoidal roughness, where the height and wavelength of roughness are systematically varied, on turbulent flow structures in pipe flow. This study observed that a secondary flow is generated due to the roughness in the near-wall region, which leads to lower stresses in the roughness canopy and the wall. Several studies concentrate on the effects of periodic roughness on mean flow features in pipe flow. Senturk and Smits (2019) studied the impact of periodic square roughness elements on fully developed laminar pipe flow. A range of roughness heights and periodic separation dis-

tances were considered. It was determined that for larger separation distances and larger roughness heights, the effective wall friction increases significantly. Liu et al. (2019) expanded on the study with the aim of elucidating more clearly the effects of changing roughness height and spacing, on fully developed laminar flow. This study further developed scaling laws for the fully developed length and friction factor, which helped to identify the relative effects of the changing parameters. Despite these studies, the case of small bar height roughness elements at high Reynolds numbers remain unexplored, especially in terms of turbulent pipe flow for tandem elements and the effect of their separation patterns.

A similar flow behaviour is observed in the wake of two- and three-dimensional bluff bodies in tandem arrangement. The notable difference between flow over such bluff bodies and axisymmetric geometries (i.e., bar roughness elements in a pipe) are the presence of three-dimensional coherent structures resulting from the vortex shedding and the formation of horse-shoe vortices. Such three-dimensional structures entail different flow responses behind the body. These types of wake dynamics have been studied extensively in the past decades in the form of flow over wall-mounted cylinders, such as Hussein and Martinuzzi (1996), Wang et al. (2014), Diaz-Daniel et al. (2017), and Wang and Lam (2019). In case of the wake of tandem bluff bodies, there are several studies, the most relevant of which are Paik et al. (2009) and Wang et al. (2014). In their numerical study, Paik et al. (2009) examined the flow around two tandem wall-mounted cubes using Detached Eddy Simulations (DES) at $Re = 2.2 \times 10^4$ to benchmark the performance of different DES models. They observed that the separation distance between the tandem cubes significantly influence the mean (velocity) and fluctuating (turbulent) flow fields. It was determined that, due to an impinging influence of the incoming flow on the second cube, the flow separation was delayed. This resulted in the formation of second horse-shoe vortices around the second cube. Wang et al. (2014) expanded on this by conducting experiments on the flow around two tandem square cylinders placed near a plane wall. With varying inter-cylinder separation ratio and the wall-to-cylinder separation ratio, they confirmed the existence of three flow regimes: Shielding, Reattachment and impinging regime, formed due to changing separation distances. Thus, it is feasible to argue that

the flow around two tandem square bar roughness elements may be affected by their separation distance. However, the nature of their wake, interactions and the overall recovery of the turbulent pipeflow is intuitively different due to their axisymmetric nature.

The study of flow over multiple wall-mounted structures, contrary to those limited to a single structure, have received limited attention despite its wide range of application in marine research and sub-sea installations. Studies pertaining to flow over multiple wall-mounted structures, such as wall mounted ribs and fins, focus mainly on heat-transfer phenomenon in channel flows (Ashrafian et al., 2004; Nagano et al., 2004; Okamoto et al., 1993; Miyake et al., 2001). There are limited studies related to the response and recovery of the turbulent pipeflow due to wall-mounted repetitive structures. In this study, we examine the flow response and recovery by simulating turbulent pipeflow past multiple square-bar roughness elements placed in a tandem arrangement at $Re = 1.56 \times 10^5$. Particularly, we expand on the the experimental work of Smits et al. (2019) by evaluating the flow recovery and quantifying the length scale of recovery for tandem placement of square bar roughness elements for the first time in far-downstream regions. Furthermore, we study the influence of periodic and staggered separation patterns to determine their effect on the mean flow features. The flow response and recovery are evaluated by determining the mean wake characteristics, such as the mean recirculation length and distribution of Reynolds shear stresses.

3.3 Problem Description

The response and recovery of turbulent pipeflow over square bar roughness elements of two different heights are studied at $Re = 1.5 \times 10^5$. First, a validation study was conducted to benchmark the performance of four turbulence models in simulating the flow past a single square bar roughness element. This was followed by studying the effects of bar-height on overall recovery process using the best performing RANS model. Finally, the flow dynamics, response and recovery are examined in the case of different tandem arrangements for multiple bar roughness elements. The

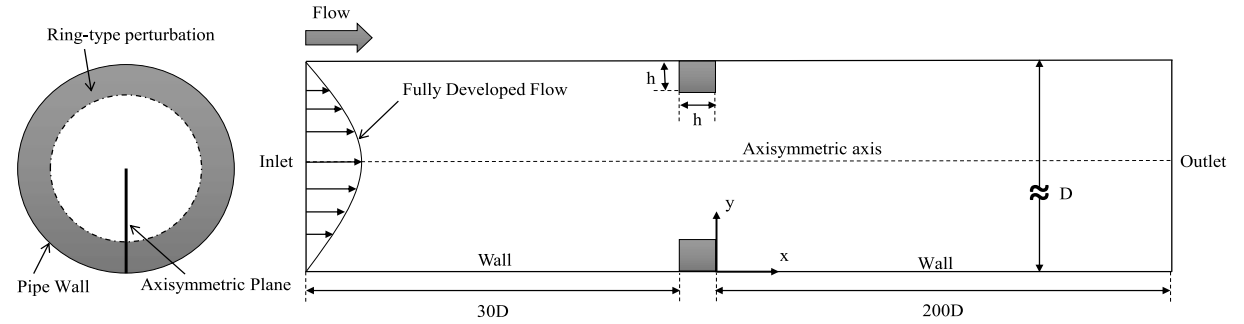

(a)

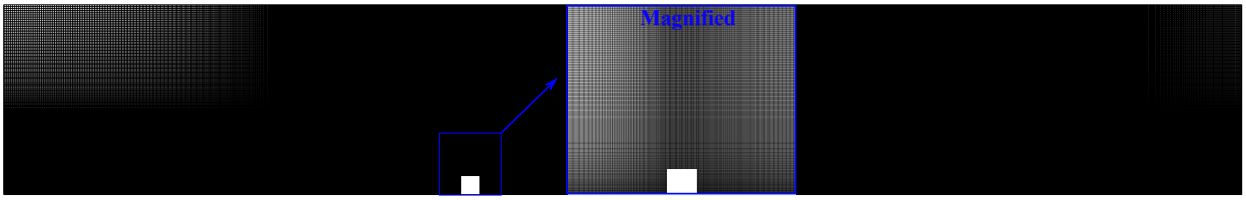

(b)

Figure 3.1: Schematic definition of the (a) computational domain and (b) spatial grid, magnified at region of interest. Shown is the lower half of the pipe. Darker regions are the result of higher density grid.

implications of the separation distance between tandem square bar elements on turbulent pipeflow dynamics were determined by placing the elements in periodic and staggered patterns.

The computational domain was designed to follow the experimental setup of Smits et al. (2019) and Yamagata et al. (2014). The axisymmetric perturbation was introduced by placing a square cross-section ring with heights of $h/D = 0.05$ and 0.1 in the pipe. Here, the square bar roughness element has a height of h and the inner diameter of the pipe is D. All simulations were performed in a 2D-axisymmetric plane. Figure 3.1a shows the schematics of the pipe with the origin of the coordinate system placed on the lower wall of the pipe downstream of the leeward face of the square bar. The domain extended from $-30D$ to $+200D$ in the $x-$direction (axial) and $R = D/2$ in the $y-$direction (wall-normal). A fully developed inflow condition is employed at the Inlet, while outlet boundary is located far from the roughness element so that it does not affect the flow recovery. This domain size allows the study of far downstream behavior of the turbulent pipeflow using RANS models.

A non-homogeneous spatial grid with a total of 2.95×10^6 hexahedral elements was used to discretize the domain. The grid distribution was such that finer mesh was generated near the roughness element and larger elements were placed close to the boundaries (see Figure 3.1b). A grid setup similar to Yamagata et al. (2014) is designed, in which the average value of y^+ is below 25. This facilitates the use of high Reynolds number wall modeling methods in the logarithmic-law region (Liu, 2016). The maximum grid expansion ratio remained below 1.03 in the entire domain. The spatial grid close to the inlet was sufficiently refined to allow for stable transition of the fully developed flow profile. For the inlet, we carried out a simple pipeflow simulation using a smooth pipe with a length of over $200D$ to generate the fully developed flow conditions. The outlet flow profile from this initial simulation was then used at the inlet of the main simulations. The no-slip wall boundary conditions, along with a high-Reynolds number standard wall function (Liu, 2016) was set at the walls and the roughness element. The outflow Neumann-type condition was imposed on the outlet, based on which $\partial\varphi/\partial n = 0$, where φ is any flow variable. The boundary conditions for turbulent quantities are initialized and set fixed at inlet. Using the friction factor correlation given by McKeon et al. (2004), the upstream friction velocity corresponded to the friction Reynolds number of $Re_\tau = u_\tau D/\nu = 7100$. The Reynolds number based on the square bar height was 7.80×10^3 and 1.56×10^4 for $h/D = 0.05$ and 0.1, respectively. The linear expansion ratio was 1.11 for the former bar height, and 1.25 for the latter.

The Reynolds Averaged Navier-Stokes (RANS) equations (Versteeg and Malalasekera, 2007) were solved using OpenFOAM, an open-source finite-volume-method platform. The four turbulence models used for the validation study were: the Standard k$-\varepsilon$ model (Case1 and Case5), the Realizable k$-\varepsilon$ model (Case2 and Case6), the k$-\omega$ model (Case3 and Case7), and the SST k$-\omega$ model (Case4 and Case 8). Details regarding these models, including the coefficients and model constants, can be found in Section 2.2 and the following literature (Launder and Spalding, 1983; Wilcox et al., 1998b; Menter et al., 2003; Shih et al., 1994). All discretized equations were solved using SimpleFoam, a steady-state solver for incompressible, turbulent flow, incorporating the SIMPLE (Semi Implicit Pressure Linked Equation) algorithm (OpenCFD, 2019). The

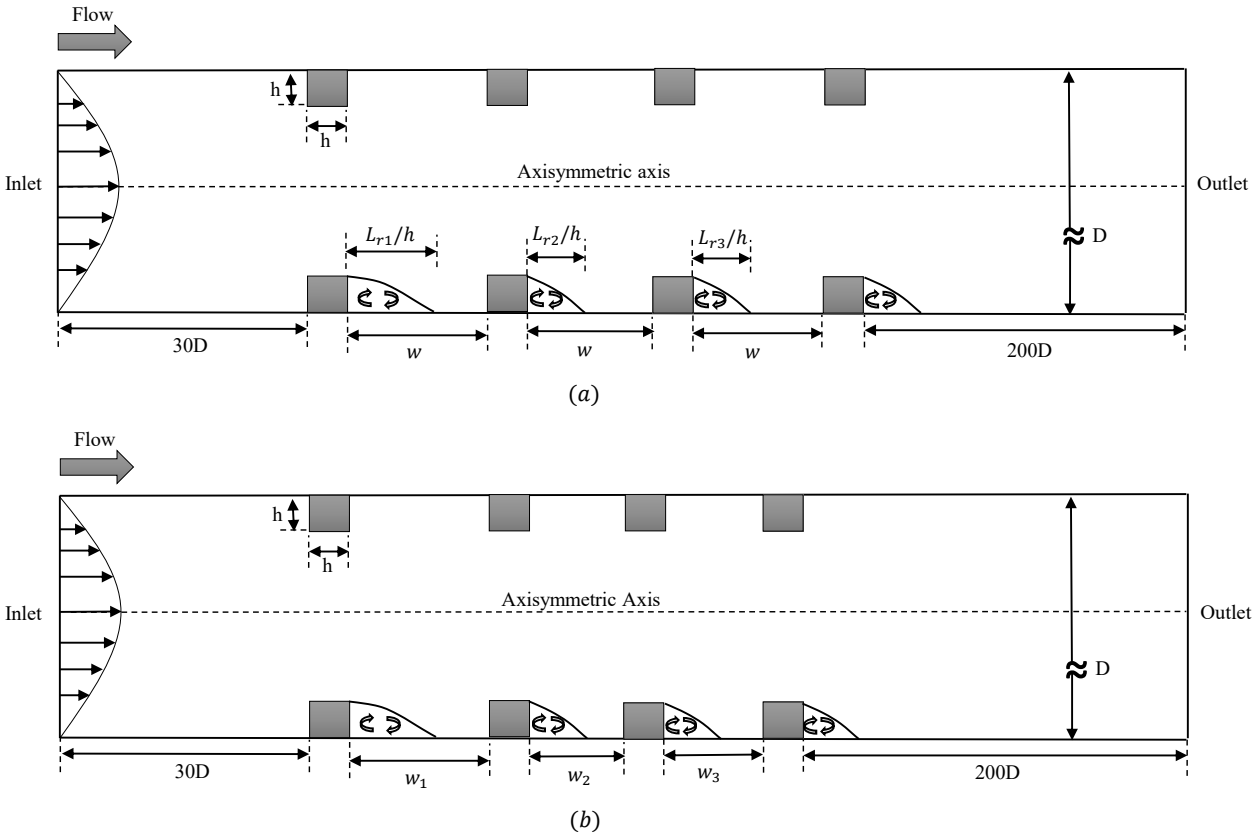

Figure 3.2: Schematic definition of the multiple squarebar cases with periodic separation (a), and staggered separation (b), of roughness elements.

second-order accurate and bounded numerical discretization schemes were employed for solving the advection and diffusion terms. The convergence criteria was set as the root-mean-squared of momentum residuals of 10^{-5}. All simulations were completed using 16 CPUs and 32 GB of memory on Compute Canada clusters.

3.3.1 Multiple Tandem Bar Roughness Configuration

We investigated the effect of multiple bar roughness configuration in tandem arrangement on the recovery of turbulent pipeflow. Figure 3.2 shows the schematics of multiple square bar roughness with periodic and staggered separation patterns. The roughness height of $h/D = 0.05$ was considered for this study based on the performance of RANS models, which will be discussed later. The simulation setup closely followed that of a single bar roughness element. Here, however, we first

studied the effect of increasing the number of roughness elements on the mean flow characteristics by placing two, three and four elements with a periodic separation along the pipe. This is followed by examining the effect of staggered separation using four roughness elements.

The separation distance (w) was defined as a function of the reattachment length (L_r/h) obtained by the flow over one roughness element. The periodic separation distance between two consecutive elements was $w = 3L_r/h$. Figure 3.2a shows the schematics of four square bar elements placed using a periodic pattern. In case of the staggered placement of roughness elements in Figure 3.2b, the separation distances are a function of the reattachment lengths behind individual square bars obtained from the periodic spacing study. The separation distance was defined as $w_i = 3L_{ri}/h$, where the subscript i identifies the square bar number.

3.4 Verification and Validation

The simulations are first validated and their accuracy verified to establish a benchmark for the best-performing RANS model in simulating pipeflow under adverse pressure gradients. The simulation results for all RANS models are compared with the experiments of Smits et al. (2019) at the same Reynolds number. To this end, this comparison generates a benchmark on how accurately the RANS models predict the behavior of perturbed or non-equilibrium flows. Hereafter, all length metrics are normalized by either h or $R = D/2$, where the scaling is specifically stated. The velocity field is normalized using the maximum value on the based flow profile, where U_b and u_r are the maximum mean and fluctuating velocities at the inlet, respectively.

3.4.1 Grid Sensitivity Study

A grid sensitivity analysis was completed to verify the adequacy of our spatial grid quality. Three grids with the same in-homogeneous distribution and quality were used based on the Standard k$-\varepsilon$ model and the bar height of $h/D = 0.05$ (Case1). The total number of elements for Grid 1 was 2.97×10^5, for Grid 2 was 1.17×10^6, and for Grid 3 was 2.95×10^6. The grid sensitivity analysis was based on tracing the effects of grid size on mean axial velocity and Reynolds shear stresses

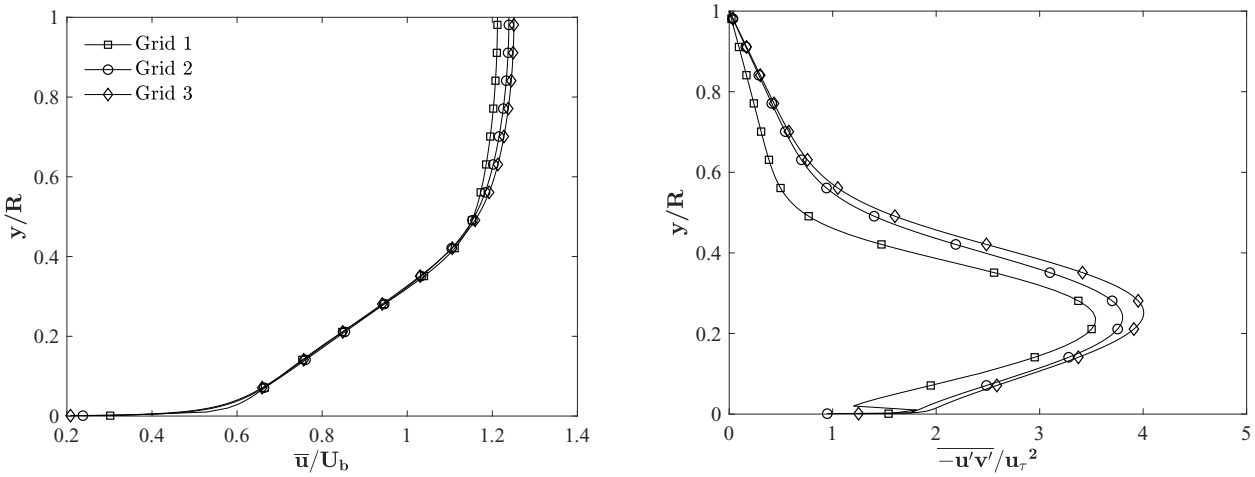

(a) (b)

Figure 3.3: Effect of grid size on (a) mean axial velocity and (b) Reynolds shear stress, at $x/D = 2$.

in the flow at $x/D = 1$, 2 and 5. Here, we only focus on the results at $x/D = 2$ for brevity. The velocity profiles in Figure 3.3a show that the difference between Grid 2 and Grid 3 is less than 5%. This is an indicator that the spatial mesh of Grid 3 is sufficient for capturing the mean flow features. Similarly, the comparison of Reynolds shear stresses amongst the three grids reveal a difference of less than 5% between Grid 2 and Grid 3, which indicates that even Grid 3 is sufficient for capturing the turbulent field.

3.4.2 Performance of RANS models

We begin by comparing the performance of four traditional RANS models in predicting the turbulent pipeflow response and recovery to square bar roughness. Particularly, we focus on determining the mean recirculation length and the nature of the mean flow field using the streamline flow profiles. This is followed by comparison of the turbulent field characteristics in the flow. Figures 3.4 and 3.5 show the mean streamline plots for both bar height cases. All turbulence models succeed in capturing the mean wake features, such as the separation point, the recirculation zone and the reattachment point. The flow separation occurs at the upstream edge of the roughness element, and the lateral width (height) of the recirculation zone exceed the bar height slightly by $\sim 10\%$. This

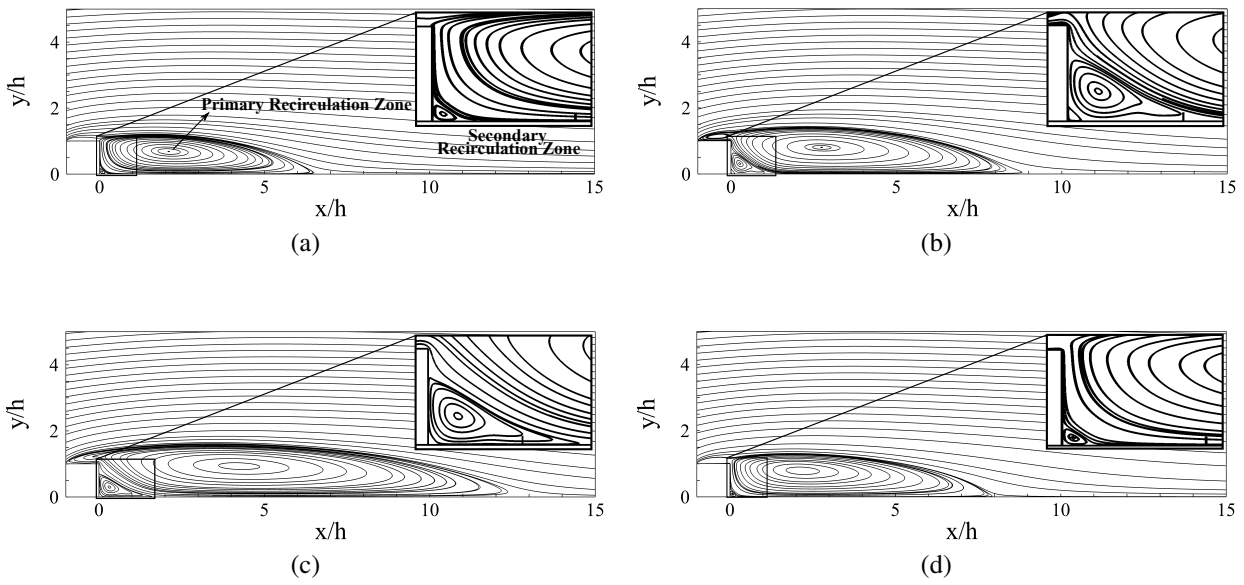

Figure 3.4: Streamline plot of turbulent pipeflow with square bar roughness with $h/D = 0.05$ using different RANS models: (a) Standard k$-\varepsilon$, (b) Standard k$-\omega$, (c) SST k$-\omega$, and (d) Realizable k$-\varepsilon$.

is consistently observed in all the simulations considered here. The mean recirculation length is identified to be under-predicted by the Standard k$-\varepsilon$ model and over-predicted by the other turbulence models in comparison to experimental data (Smits et al., 2019). This difference is attributed to the prediction of pressure gradients and velocity gradients immediately behind the perturbation. This is consistent with the numerical study by Fogaing et al. (2019), where RANS models had difficulties in predicting the mean flow correctly when there exists a large pressure gradient in the wake of a sharp-edge bluff body. Furthermore, Leonardi et al. (2003) and Hemmati et al. (2019) have similar observations, in which eddy-viscosity approximation cannot predict the correct flow gradients when the flow starts experiencing adverse pressure gradients downstream of the center of the recirculation zone. Another reason for such discrepancies are the High-*Re* effects in complex flows, which are difficult to be modeled numerically (Hultmark et al., 2012). All models resolved the secondary recirculation region, which forms within the primary recirculation zone. This secondary recirculation region was not observed properly through experiments due to the limited resolution of PIV measurements as discussed by Smits et al. (2019). Durst and Wang

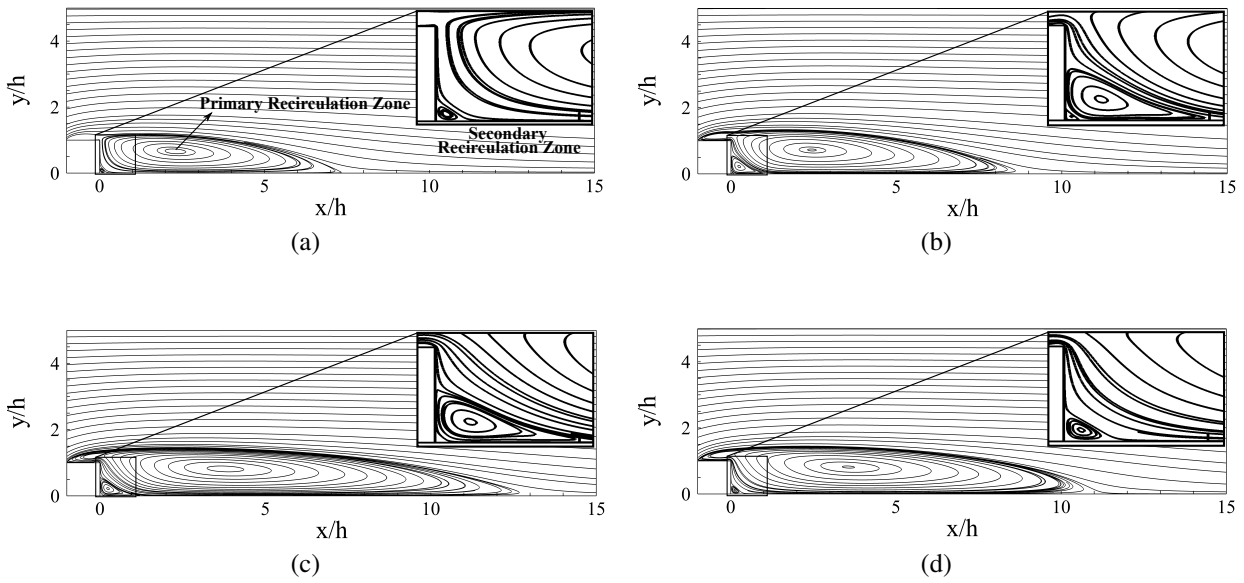

Figure 3.5: Streamline plot of turbulent pipeflow with square bar roughness with $h/D = 0.1$ using different RANS models: (a) Standard k$-\varepsilon$, (b) Standard k$-\omega$, (c) SST k$-\omega$, and (d) Realizable k$-\varepsilon$.

(1989) also reported a similar observation. Thus, all RANS models considered here could predict the existence of positive vorticity as shown by the experiments of Smits et al. (2019).

A quantitative comparison of our numerical results with experiments of Smits et al. (2019) is presented in Table 3.1, which focuses on the prediction of the mean recirculation length. As mentioned earlier, Realizable k$-\varepsilon$ (Case2 and Case6), k$-\omega$ (Case3 and Case7) and SST k$-\omega$ (Case4 and Case8) models over-predict the reattachment length. Realizable k$-\varepsilon$ model (Case2) shows close prediction for $h/D = 0.05$ with minor deviation, while over-predicting for $h/D = 0.1$ (Case6). This motivates further wake analysis to identify the key differences that lead to inaccuracies in capturing the flow field by the Realizable k$-\varepsilon$ model. Both standard k$-\varepsilon$ and Realizable k$-\varepsilon$ models are High-*Re* models, while the realizable formulation takes into account the near wall treatment. The standard k$-\omega$ model (Case3 and Case7) resulted in the third best solution, and the SST k$-\omega$ model (Case4 and Case8) returned the largest over-estimation.

The experimental study of Dimaczek et al. (1989) on the flow over two-dimensional surface-mounted obstacles revealed that the reattachment length was affected by the separation at the lead-

Table 3.1: Comparing the mean recirculation length ($\overline{L_r}$) obtained using different RANS models.

Study	h/D	**Method**	$\overline{L_r}/h$	$\Delta\overline{L_r}[\%]$
Case 1	0.05	Standard k$-\varepsilon$	7.64	-6.6
Case 2	0.05	Realizable k-ε	8.02	$+1.9$
Case 3	0.05	k$-\omega$	9.82	$+20.04$
Case 4	0.05	SST k$-\omega$	14.53	$+77.62$
Smits et al. (2019)	0.05	Experiment (PIV)	8.18	-
Case 5	0.1	Standard k$-\varepsilon$	7.90	-16
Case 6	0.1	Realizable k-ε	11.23	$+19.34$
Case 7	0.1	k$-\omega$	10.07	$+7.01$
Case 8	0.1	SST k$-\omega$	14.41	$+53.13$
Smits et al. (2019)	0.1	Experiment (PIV)	9.41	-

ing edge. The Re_h and linear expansion ratio for Dimaczek et al. (1989) was similar to the present study. The flow separation induces higher velocity gradients near the leading edge, the value of which is larger for $h/D = 0.1$ compared to $h/D = 0.05$. Fogaing et al. (2019) observed similar inconsistencies in prediction of the reattachment length by different RANS models. These were attributed to the limitations of RANS models in predicting flows with larger gradients. Inconsistency in prediction of the reattachment length by the Realizable k$-\varepsilon$ model is therefore related to its inability to capture the leading edge separation correctly. To further examine the turbulent field, we focus on the distribution of Reynolds stresses, turbulent kinetic energy and terms of the energy budget.

The distribution of Reynolds shear stresses at $x/h = 80$ and $x/h = 100$ are compared in Figures 3.6 and 3.7. The profiles obtained by different RANS models are compared to the experimental data of Smits et al. (2019) and the theoretical fully-developed total shear stress profile (Kaneda et al., 2003). Significant differences are observed for both bar heights. First, higher than normal shear stress values are predicted by the Standard and Realizable k$-\varepsilon$ models (Case1, Case2, Case5 and Case6). The Standard k$-\varepsilon$ model formulation excludes near-wall treatment, which can be a reason for higher stress values near the wall. The Realizable k$-\varepsilon$ model shows a better performance than the standard model, yet predicting higher Reynolds stresses. Furthermore, Standard k$-\omega$ and SST k$-\omega$ models provide close prediction at near-wall region since they incorporate en-

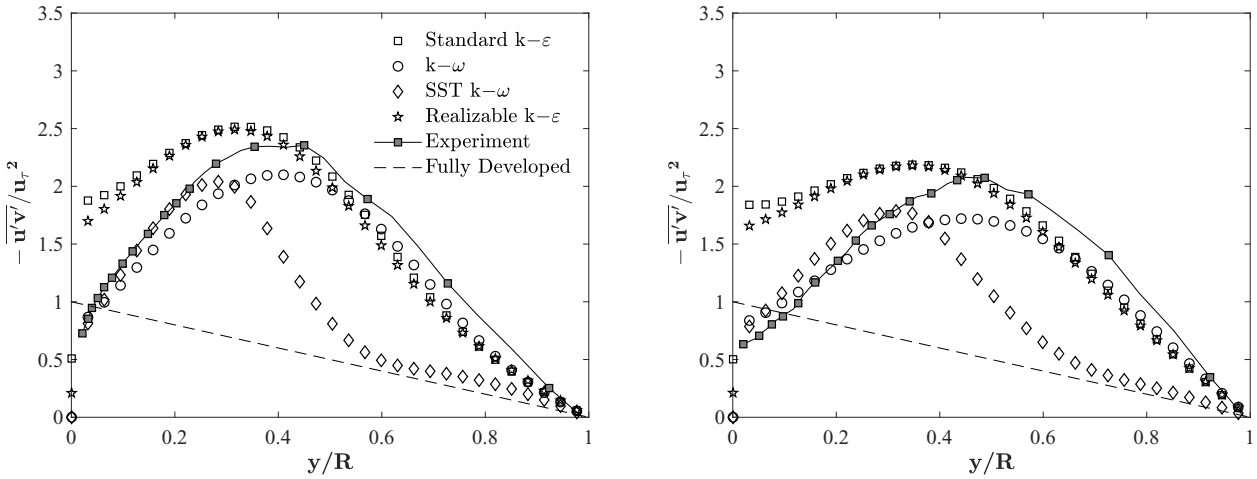

Figure 3.6: Comparison of Reynolds shear stresses for bar height $h/D = 0.05$ at axial locations (a) $x/h = 80$ and (b) $x/h = 100$. Reynolds shear stress is normalized by friction velocity (u_τ).

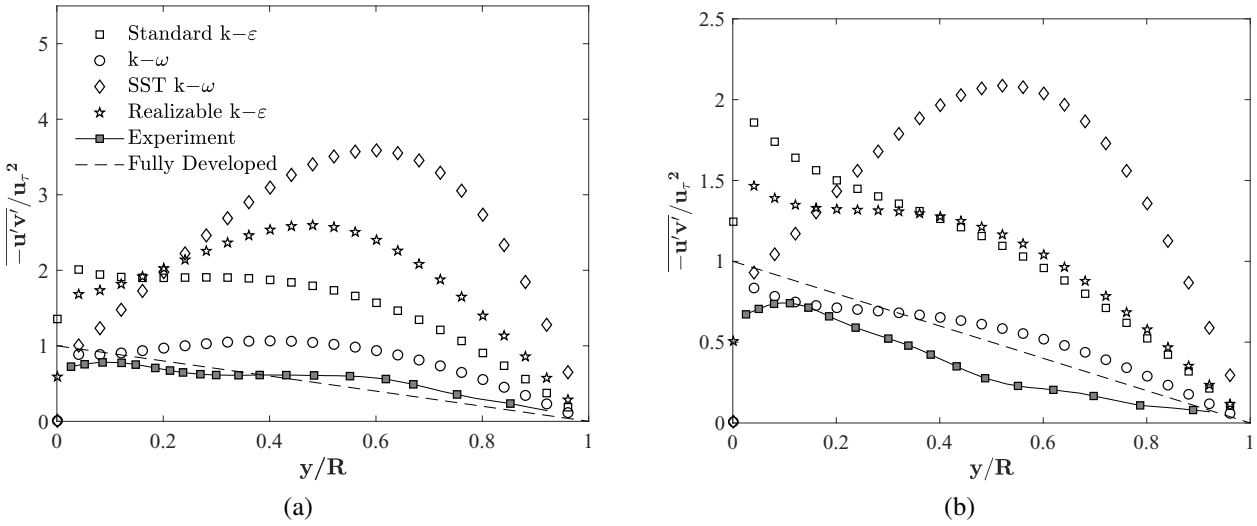

Figure 3.7: Comparison of Reynolds shear stresses for bar height $h/D = 0.1$ at axial locations (a) $x/h = 80$ and (b) $x/h = 100$. Reynolds shear stress is normalized by friction velocity (u_τ).

hanced near-wall treatment (Menter and Esch, 2001). In case of $h/D = 0.05$ (Figure 3.6), Standard k$-\omega$ model depicts a closer trend to the experimental values, while SST k$-\omega$ model portrayed a collapse in stresses halfway to the centerline. For the case of $h/D = 0.1$ in Figure 3.7, all turbulence models over-predict shear stresses, with SST k$-\omega$ model showing the largest deviation. The thicker bar roughness height produces a relatively stronger contraction in the flow, creating

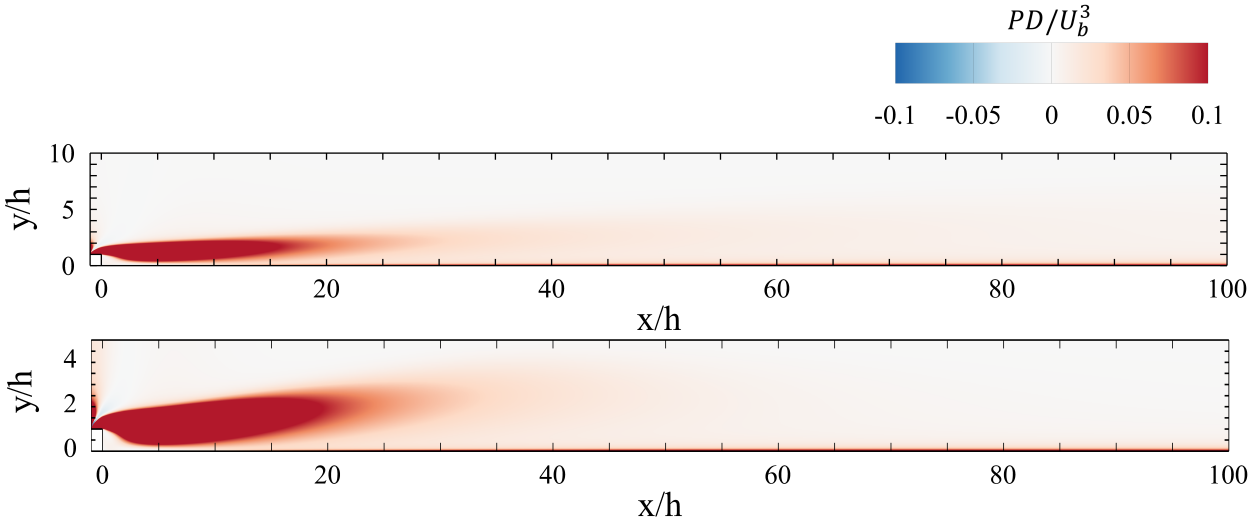

Figure 3.8: Turbulence kinetic energy production contours compared for bar heights $h/D = 0.05$ (Top) and $h/D = 0.1$ (Bottom), obtained by standard k$-\varepsilon$ model. Production (P) is normalized with pipe diameter (D) and bulk velocity (U_b).

higher velocity gradient near the roughness element. This intuitively corresponds to a higher turbulence production shown in Figure 3.8. Hence, the overshoot of Reynolds shear stresses in case of $h/D = 0.1$ can be attributed to the limitation of RANS models in predicting flows with large gradients (Fogaing et al., 2019) and turbulent energy production in small regions of the flow. The re-adjustment of the energy terms in the budget due to this shortcoming is observed through the over- and under-prediction of different flow characteristics.

$$P_k = -\overline{u_i' u_j'} \frac{\partial \overline{u_i}}{\partial x_j}, \tag{3.1}$$

$$\varepsilon = \nu \overline{\frac{\partial u_i}{\partial x_j} \frac{\partial u_i}{\partial x_j}}, \tag{3.2}$$

The recovery of the turbulent flow, downstream of the recirculation region, is examined by looking at the evolution of the turbulence production (P_k), dissipation (ε) and transport along the bar wake centerline in Figures 3.9 and 3.10. The definitions of Production and dissipation thers are given in Equation 3.1 and 3.2. Since the models predict different recirculation lengths, the coordinate axes are normalized by the mean recirculation length ($\overline{L_r}$) obtained by each model. A

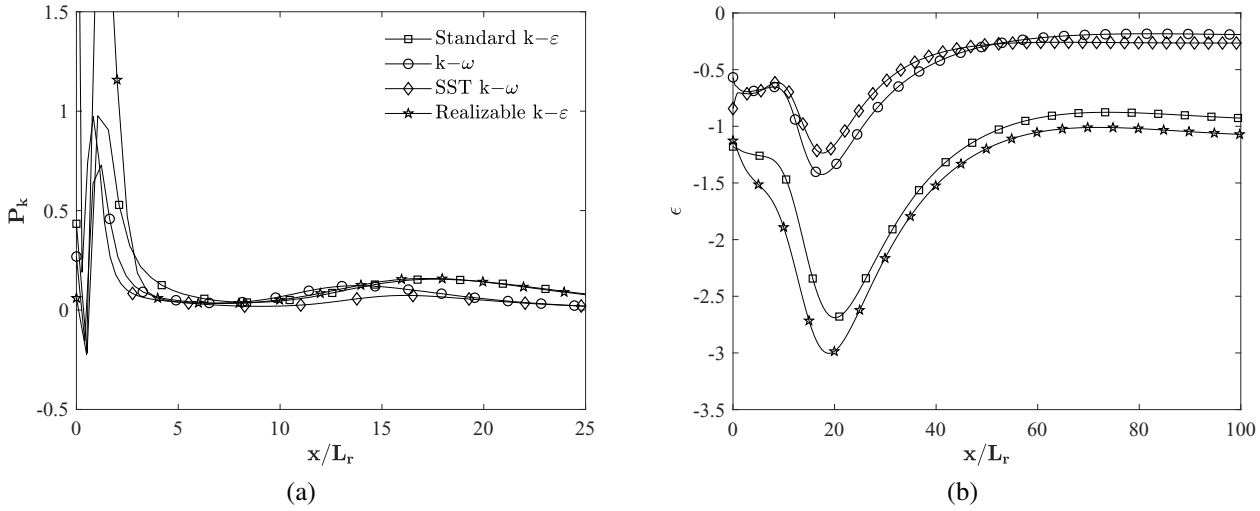

Figure 3.9: The turbulent kinetic energy production (a) and dissipation (b) for bar height $h/D = 0.05$, along wake centerline. x is normalized by mean recirculation length.

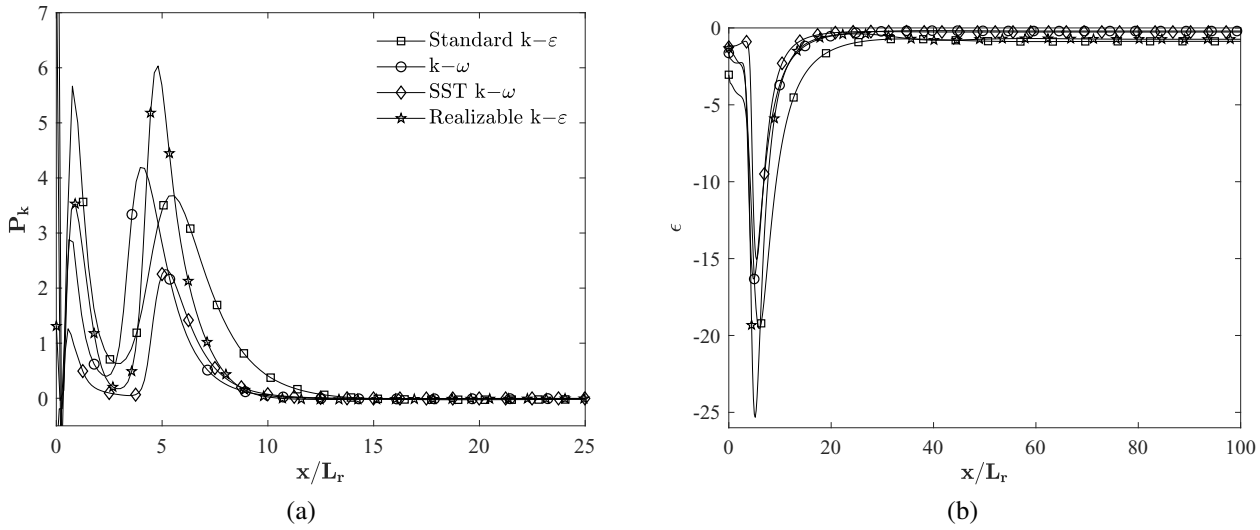

Figure 3.10: The turbulent kinetic energy production (a) and dissipation (b) for bar height $h/D = 0.1$, along wake centreline. x is normalized by mean recirculation length.

similar, and expected, trend is observed for both bar heights, in which the initial drop in turbulence production is followed by a recovery and overshoot at $x \approx \overline{L_r}$. For the thicker bar roughness case ($h/D = 0.1$), there is a second peak observed in the turbulence production along the wake centerline. This second peak is significantly more subtle as the bar height reduces to $h/D = 0.05$. This implies that the turbulence production subsides in the downstream region of the recirculation zone faster with a thicker bar roughness element. Experiments of Smits et al. (2019) also identify

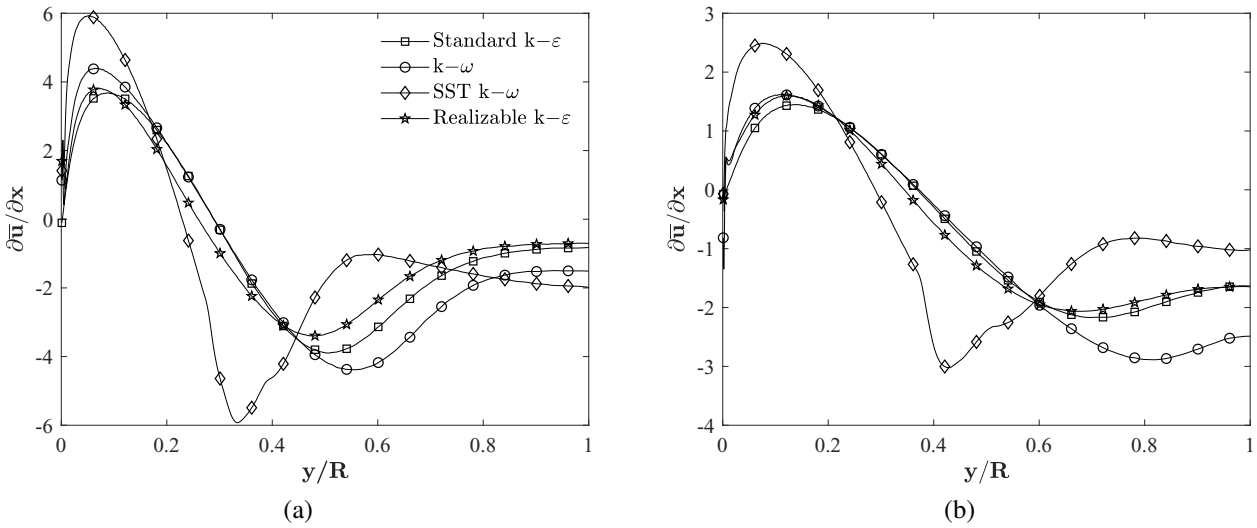

Figure 3.11: Comparison of mean streamwise velocity gradient in the wake, for bar height $h/D = 0.05$ at axial locations (a) $x/h = 60$ and (b) $x/h = 100$.

such behavior as a second-order response to abrupt changes in the flow. Earlier, Smits et al. (1979) investigated such second-order responses in the flow, which they determined that it causes an initial amplification in Reynolds stresses, similar to the observations in Figure 3.6, followed by a rapid decay further downstream. All RANS models could predict this complex flow behavior despite their limitations in capturing large flow gradients.

The peak in the production and dissipation of turbulence obtained by the Standard k$-\varepsilon$ model (Case1 and Case5), for both bar heights, is moved further downstream compared to other models. The Realizable k$-\varepsilon$ model predicts a two fold rise near the stagnation point for $h/D = 0.05$, compared to the standard model. For both bar heights, k$-\omega$ and SST k$-\omega$ models predict a higher rate of diffusion compared to the Standard k$-\varepsilon$ and Realizable k$-\varepsilon$ models. This could account for the overestimation of the recirculation length by these models since they try to balance the energy budget.

Figures 3.11 and 3.12 present the distribution of streamwise velocity gradients calculated by different RANS models at two axial locations: $x/h = 60$ and 100. All models predict higher velocity gradients near the wall. These gradients appear to be suppressed near the centerline. Moreover, the SST k$-\omega$ model show a deficit in gradients for $h/D = 0.1$ earlier than other models,

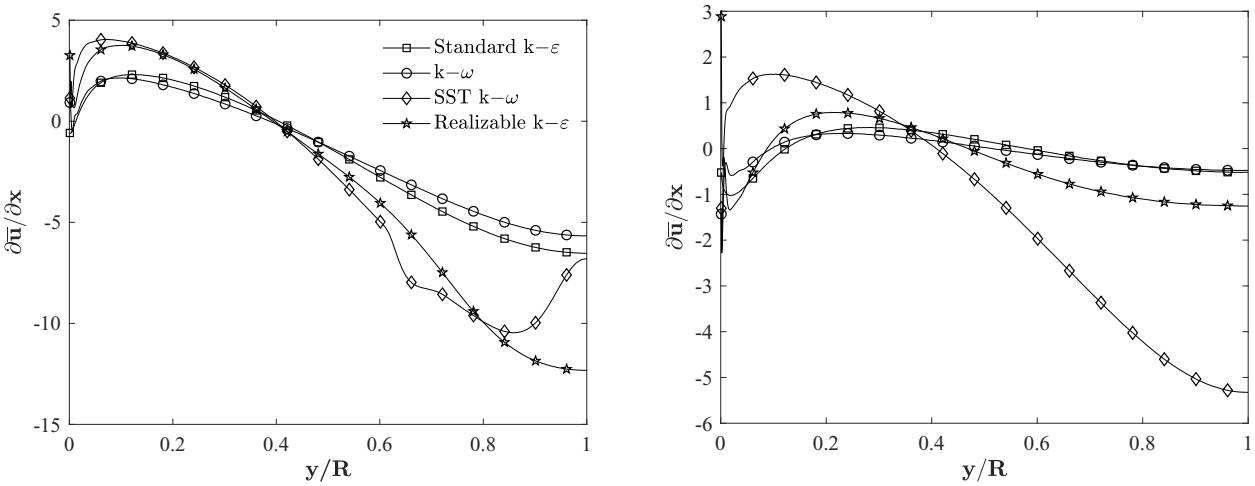

Figure 3.12: Comparison of mean streamwise velocity gradient in the wake, for bar height $h/D = 0.1$ at axial locations (a) $x/h = 60$ and (b) $x/h = 100$.

the location of which correlate to that of the peak in Reynolds stresses in Figure 3.7. Smits et al. (2019) showed that due to stronger contraction produced by roughness elements, an overshoot of velocity gradients can be observed in the wake, a trend which is evident in Reynolds stresses. Thus, the differences in prediction hints at limitation of these models in predicting flows with strong gradients again. For bar height of $h/D = 0.05$, all models show a slow recovery towards the centerline for $x/h = 60$ and 100, which suggests a long recovery process. However, there is a sharp decay towards the pipe centerline in the same region for $h/D = 0.1$, which is consistent with the findings of Smits et al. (2019).

The validation study showed that the Standard k$-\varepsilon$ model performed the best overall, and especially well for $h/D = 0.05$. The reattachment length for the case of $h/D = 0.05$ shows less than 7% deviation from the experiments. A consistent trend is observed in prediction of Reynolds stresses, in terms of intensity and location of the peak. The good agreement between the results of the Standard k$-\varepsilon$ model and experiments of Smits et al. (2019) is collaborated by the similar observations in previous studies, including Durst and Wang (1989) and Shah et al. (2012). This provides us with sufficient confidence that the Standard k$-\varepsilon$ model can properly capture the physics of the flow despite inevitable discrepancies that may exist. Therefore, the Standard k$-\varepsilon$ model is utilized

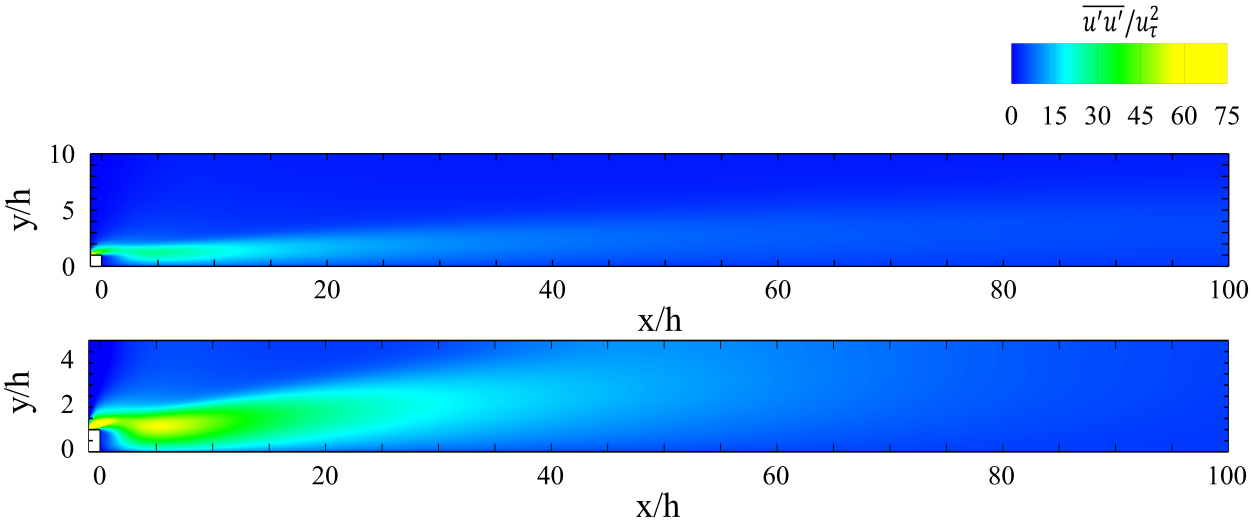

Figure 3.13: Comparison of Reynolds normal stresses for bar heights $h/D = 0.05$ (Top) and $h/D = 0.1$ (Bottom). The Reynolds stresses are normalized by the friction velocity (u_τ).

further to study the effects of multiple square bar roughness elements and separation patterns on the mean flow properties and the recovery of turbulent pipeflow.

3.5 Results & Discussion

We begin by looking at the flow behavior over a single bar roughness element as our reference case to establish the difference imposed by the additional elements in the pipe. We then proceed by adding 2, 3 and 4 roughness elements in the pipe using a periodic and staggered pattern. For brevity, we only show the implications of the staggered pattern using 4 bar roughness elements.

3.5.1 Recovery of Mean Flow Over Single Roughness Element

The recovery of turbulent pipeflow over two bar heights ($h/D = 0.05$ and 0.1) is studied by tracing the turbulent and mean flow fields downstream of the perturbation. The Reynolds normal stresses ($\overline{u'u'}$) and Reynolds shear stresses ($-\overline{u'v'}$) are compared over the same span downstream of the roughness elements, to investigate the transport of turbulent stresses. Due to a strong contraction created by the thicker bar, a higher velocity gradient was observed near $y = h$. This leads to a larger

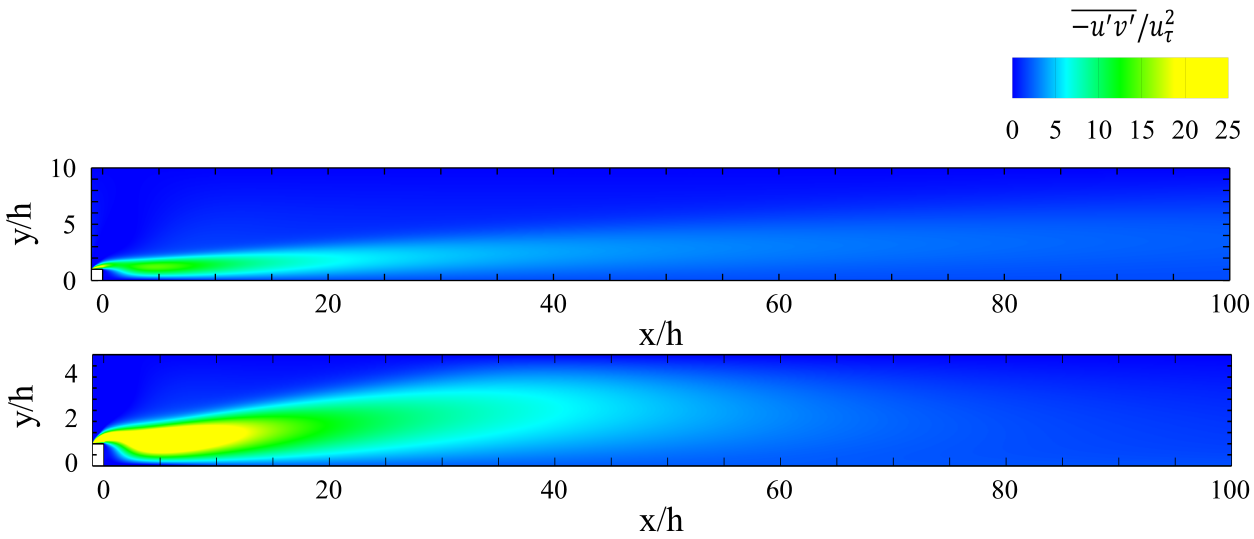

Figure 3.14: Comparison of Reynolds shear stresses for bar heights $h/D = 0.05$ (Top) and $h/D = 0.1$ (Bottom). The Reynolds stresses are normalized by the friction velocity (u_τ).

turbulent production, which is evident from Figures 3.13 and 3.14. Furthermore, the transport of the stresses, in both bar heights, is away from the wall. For $h/D = 0.05$, the shear stresses transport away from the wall and towards the centerline with decreasing intensity and increasing width. The transport is slow, which extends its effects upto $x/h = 100$. For the case of $h/D = 0.1$, a faster transport of stresses is observed. The peak intensity reaches the centerline near $x/h = 40$, merging and mixing with the contributions from the top half of the pipe.

The recovery process is examined quantitatively by tracing the location of the maximum Reynolds shear stress (Y_M) downstream of the roughness element. Figure 3.15 shows the profile of Y_M scaled with bar height (h) and the pipe radius (R), as a function of downstream distance (x/h). Initially, the Reynolds shear stresses stay close to $y = h$ for both roughness heights (see Figure 3.15a). After $x/h = 10$, the stresses start diffusing towards the centerline and away from the wall. At $10 \leq x/h \leq 40$, the transport of $-\overline{u'v'}$ is twice as fast for $h/D = 0.1$ compared to $h/D = 0.05$, which suggests a larger rate of turbulence production for the thicker bar element. At $x/h = 70$, the shear stresses diffuse away from the centerline for the thicker roughness element, and the peak collapses as we move closer to the wall. This suggests a second-order response. For $h/D = 0.05$, stresses transport towards the centerline until $x/h = 100$, suggesting a prolonged

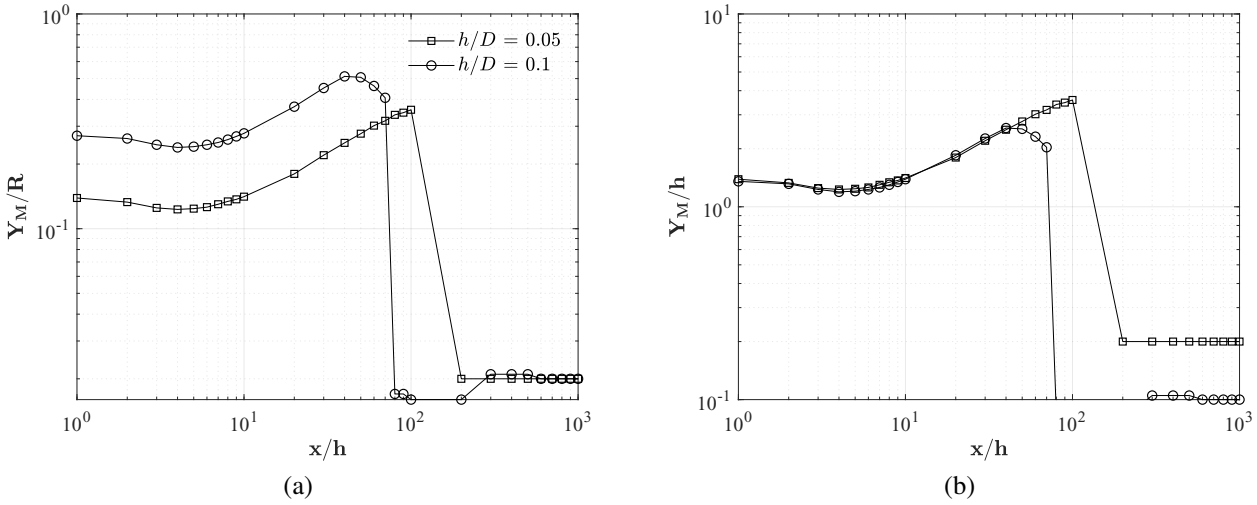

Figure 3.15: Location of maximum Reynolds Shear stress, Y_M, downstream of square-bar roughness element, (a) scaled with R and (b) scaled with h.

transport of stresses away from the wall. The flow recovery differs for axisymmetric geometries compared to the flow over three-dimensional wall mounted structures. For example, the recovery reported here is longer than that of the flow over a wall-mounted cube immersed in a turbulent boundary layer, based on the study of Diaz-Daniel et al. (2017). Scaling Y_M with the square bar height (h) in Figure 3.15b leads to an overall collapse of the data in the vicinity of the square bar element, while a similar collapse is observed in the far downstream region when Y_M is scaled with the pipe radius. This indicates that the square bar element height (h) is the correct length-scale for describing the flow characteristics near the vicinity of the roughness element. In far downstream region, the pipe radius (R) interferes with the established length scale, and becomes dominant in describing the recovery behavior. This observation serves as a confirmation to the assumption discussed by Smits et al. (2019), in which the pipe radius (R) is the correct length-scale for the flow recovery. Furthermore, a prolonged transport behavior away from the wall is observed in case of a smaller bar compared to the larger one. Thus, the smaller bar height of $h/D = 0.05$ is utilized further to study the effects of multiple elements and the influence of separation pattern between elements.

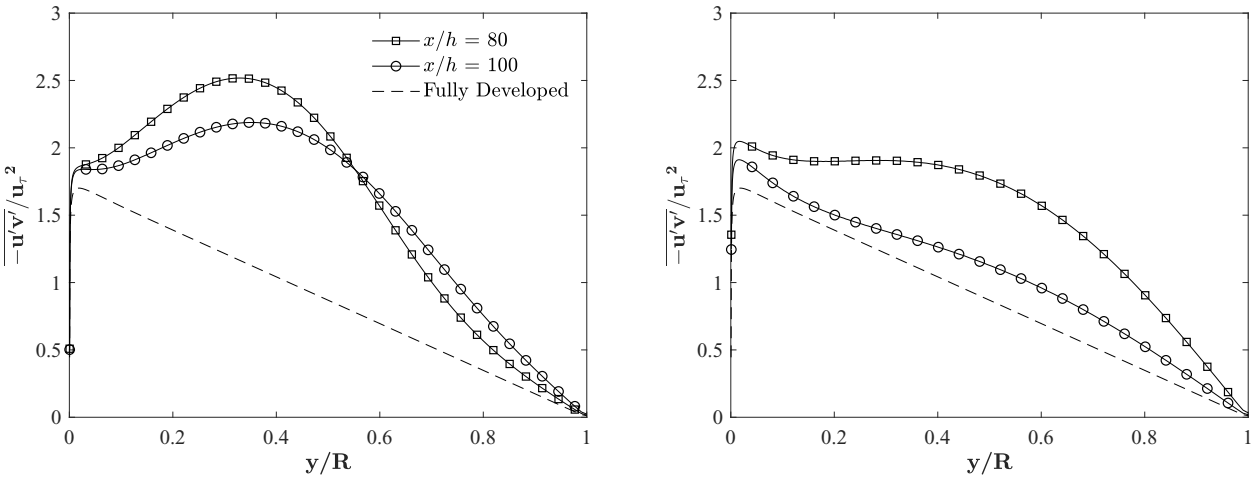

Figure 3.16: Comparison of Reynolds shear stresses, normalized by friction velocity (u_τ), at different axial locations, for (a) $h/D = 0.05$ and (b) $h/D = 0.1$.

Figure 3.16 shows the profile of Reynolds shear stresses at two streamwise locations for both bar heights compared with the theoretical profile of a fully-developed flow. For the case of $h/D = 0.05$, a slow diffusion of peak intensity is observed towards the centerline as the flow progresses from $x/h = 80$ to 100. As mentioned earlier, the intensity of shear stresses transport towards the centerline decreases, while the width increases. The intensity of Reynolds shear stresses is higher compared to the theoretical fully developed state, which leads to a longer recovery process beyond $x/h = 100$. Over the same streamwise distance, a collapse is observed towards the fully developed conditions for the case of $h/D = 0.1$, while the near-wall values remain large. Such a collapse in stresses suggests a second-order response of the recovery process, which is consistent with the findings of Smits et al. (1979).

It is apparent from the results presented thus far that the smaller bar height of $h/D = 0.05$ prolongs the mechanism of recovery downstream of the perturbation, in contrary to faster recovery obtained from $h/D = 0.1$. Based on this observation, combined with the better agreement of RANS model results with experiments for the case of a smaller bar height, we focus on using the smaller bar height elements to investigate the effect of multiple elements and their separation patterns on turbulent pipeflow recovery.

3.5.2 Multiple Bar Roughness Elements

We examine the effects of adding multiple square bar roughness elements in the pipe on the recovery and response of turbulence pipeflow using only the bar height of $h/D = 0.05$. The three cases used for this study include using a system of two periodically separated elements (SIM 2), three periodically separated elements (SIM 3), and four periodically separated elements (SIM 4). The reference case of a single bar element is referred to as SIM 1. This is followed by evaluating the influence of separation pattern between the elements. A case with four square bar roughness elements separated based on an staggered pattern (SIM 5) is also investigated.

The mean streamline plots are shown in Figure 3.17 for the periodic and staggered separation patterns. Similar to the case of a single bar element (SIM 1), the flow separation occurs at the leading edge of the square bar element. The reattachment of the shear layer occurs before the midway point between the two roughness elements, while the streamlines in the near-wall region remain horizontal. As the flow approaches the next element, streamlines are tilted upwards, forming a smaller separation region at the junction between the wall and the upstream edge of the second element. This is in close agreement with the flow visualization by Leonardi et al. (2003) at a lower Reynolds number.

As shown in Table 3.2, the mean recirculation length behind the first element exhibits a slight difference ($\sim 0.9\%$) compared to SIM 1 for all cases. For the periodic separation pattern, the mean recirculation length is shorter by $\sim 39\%$ behind second element compared to the first element. It reduces further by $\sim 2\%$ behind subsequent elements. The mean recirculation lengths behind first three elements in case of SIM 3 and SIM 4 are relatively similar, which suggests an asymptotic nature of the upstream flow conditions. A similar study using two bars with a larger height ($h/D = 0.1$) following the setup of SIM2 revealed similar flow behavior, which are not shown here for brevity.

In case of the staggered separation pattern (SIM 5), the mean recirculation length behind the first element is longer than the corresponding element in SIM4 by $\sim 0.3\%$, while the change grows sharply for the second, third and forth elements. Compared to SIM 4, the mean recirculation length

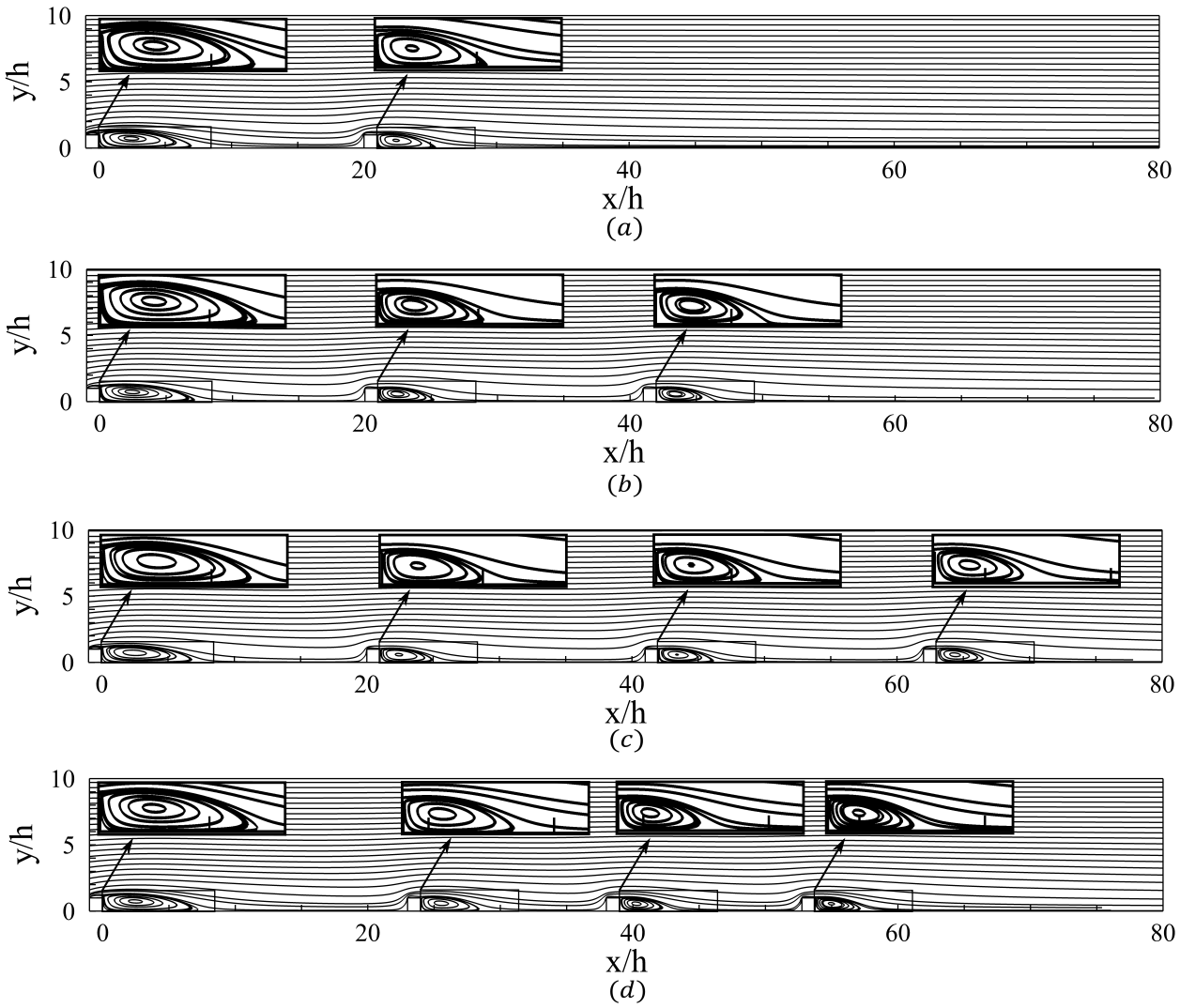

Figure 3.17: Streamline plot of the flow past multiple roughness elements of $h/D = 0.05$. Shown is (a) SIM 2, (b) SIM 3, (c) SIM 4, and (d) SIM 5.

behind the second element increases by $\sim 6\%$. It then reduces for the third and fourth elements by $\sim 10\%$. In case of the staggered pattern, the separation distances between the second and third, and the third and fourth elements have reduced since they are a functions of the mean recirculation lengths obtained from the periodic pattern bar placement in SIM4. The reduced distance between bar elements create an adverse pressure gradient, hinting at an impinging influence of the upstream element on the subsequent elements. While similarities are observed with the flow over tandem wall-mounted square cylinders (Wang et al., 2014), the wake and downstream recovery differ between the two geometries. This is mainly attributed to the axisymmetric nature of

Table 3.2: The recirculation length ($\overline{L_r}/h$) of each bar elements. Here, i denotes the element number.

Case $i=$	**1**	**2**	**3**	**4**
SIM 1 (Case1)	7.64	-	-	-
SIM 2	7.66	4.67	-	-
SIM 3	7.69	4.68	4.58	-
SIM 4	7.69	4.68	4.58	4.42
SIM 5	7.72	4.97	4.12	3.98

the pipeflow with square bar roughness elements. These observations suggest that the upstream flow conditions, arising in response to the perturbations, play an important role in determining the reattachment length.

Contours of Reynolds shear stresses are shown in Figure 3.18 over the same normalized downstream distance of $0 \leq x/h \leq 100$ to differentiate the effects of multiple elements for all cases. Initially, the stresses in the vicinity of the first element start to transport away from the wall. A sudden rise in the stresses is observed at $y = h$ for each subsequent element. The wake then merges and mixes with the contributions from the previous element, while the stresses diffuse away from the wall. Thus, there is a faster transport of $-\overline{u'v'}$ towards the centerline with increasing width and decreasing intensity as the number of elements increases. The value of stresses increases at the pipe centerline faster as the number of elements increases. For the case of staggered separation pattern, the intensity of stresses increases slightly compared to the periodic pattern of SIM 4. However, the effect on the overall recovery process is negligible.

The Reynolds stresses enable quantifying different recovery behavior of the flow with increasing number of implemented roughness elements. Figure 3.19 provides a quantitative comparison of the flow recovery for multiple bar roughness cases. All the profiles are normalized by the pipe radius (R) to study the flow recovery in far downstream region. Initially, $-\overline{u'v'}$ remains fairly similar amongst all periodic separation pattern cases (SIM 1 to SIM 4) at and near $y = h$ in Figure 3.19a. The stresses start to diffuse towards the centerline after $x/h = 5$, which as mentioned by Smits et al. (2019) may lead to a long region of lower skin friction and lower turbulence near the pipe walls. Thus, initiating such abrupt changes periodically in a wall-bounded flow may be

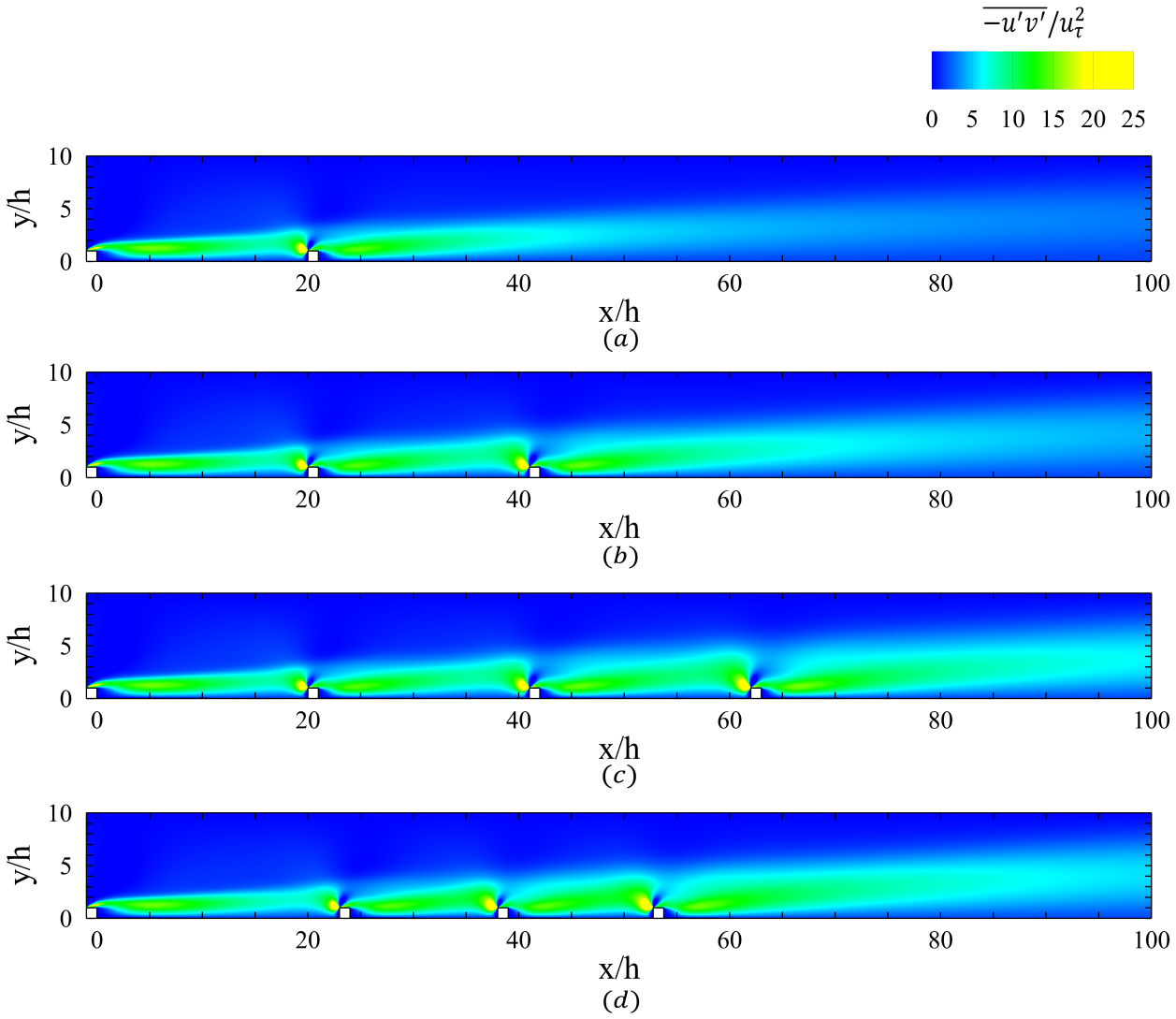

Figure 3.18: Comparison of Reynolds shear stresses for flow past multiple roughness elements. Reynolds shear stresses are normalized by friction velocity (u_τ). Shown is (a) SIM 2, (b) SIM 3, (c) SIM 4, and (d) SIM 5.

used as a form of passive flow control to lower the energy-transport requirements due to lower drag as a result of lower turbulence near the pipe walls. At $10 \leq x/h \leq 100$, the rate of transport of stresses towards the centerline increases with implementation of more roughness elements. However, there exists an asymptotic point after three tandem elements (SIM 3), where the variation is less than 2% compared to SIM 4. This suggests that the mean flow characteristics, downstream of three or more tandem elements, have reached an asymptotic trend. In far-downstream region

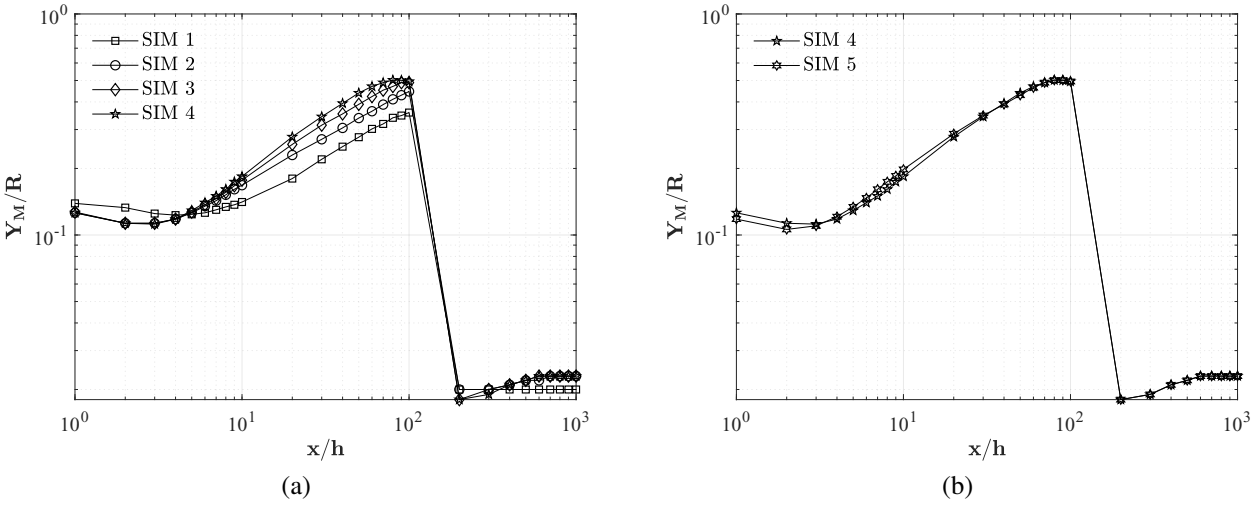

Figure 3.19: Location of maximum Reynolds Shear stress, Y_M, downstream of the last roughness elements. Y_M is normalized by R, for (a) Periodic separation and (b) Staggered separation.

($500 \leq x/h \leq 1000$), the recovery profiles coincide, further providing evidence of the asymptotic recovery behavior in turbulent pipeflow with multiple bar roughness elements.

Figure 3.19b compares the recovery of turbulent pipeflow with multiple bar roughness elements in periodic and staggered separation patterns. Initially, the stresses for SIM 5 are closer to the wall compared to SIM 4. The diffusion of stresses towards the centerline is slightly faster with the staggered pattern. Further downstream, however, the trends appear to be fairly similar. This is to say, the separation pattern has negligible effect on the recovery behavior in far downstream region if downstream elements are placed outside the mean recirculation region of upstream elements such that the streamlines recover to their horizontal streamwise pattern. A sharp collapse of Reynolds stresses is observed between $x/h = 100$ and 110, where the high intensity of stresses drop towards the wall and below the equilibrium value. This suggests a second-order response, similar to a single bar roughness case discussed earlier.

Since the bar roughness height (h) is the correct length scale of recovery in the vicinity of the roughness element, the recovery of stresses will be different for different cases at the same normalized distance (x/h) downstream of the last roughness element. Figure 3.20 compares the profiles of Reynolds shear stresses at two streamwise locations downstream of the last square

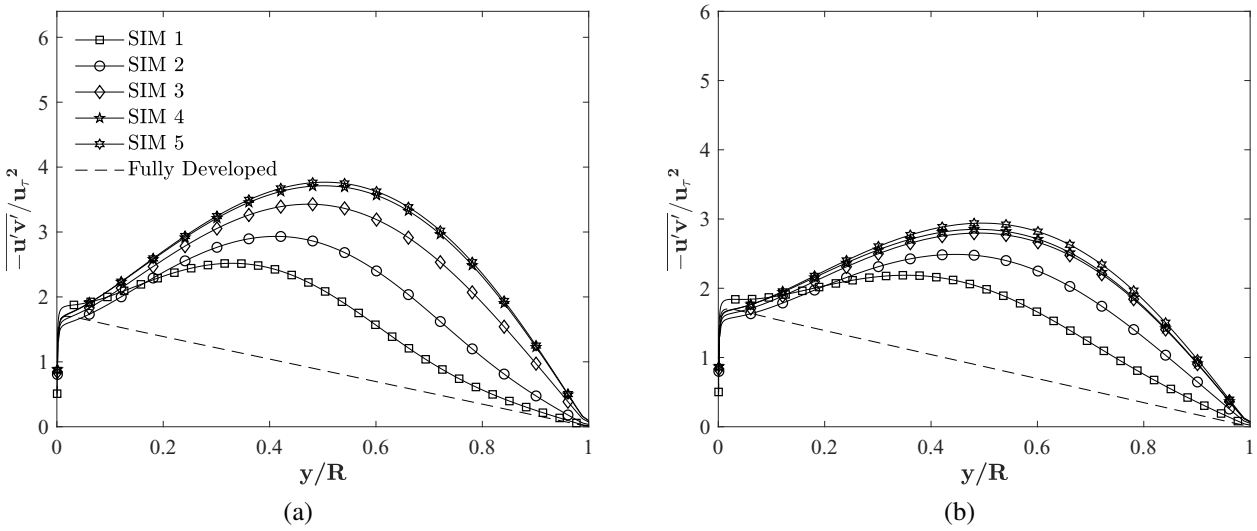

Figure 3.20: Effect of multiple roughness elements and separation distance on Reynolds shear stresses, at (a) $x/h = 80$ and (b) $x/h = 100$. Reynolds shear stresses are normalized by friction velocity (u_τ).

bar roughness element. Clearly, the profile of stresses significantly exceed the fully developed profile for all cases. As the number of elements increases, the profile of stresses shift towards the centerline ($y/R = 0.5$) faster. For SIM 3, the peak is located close to the centerline at $x/h = 80$, while the profile shifts towards $y = R$ for SIM 4 and SIM 5. At $x/h = 100$, stresses for the case of multiple elements slowly shift towards $y = R$ due to $-\overline{u'v'}$ being transported towards the centerline. At this junction, the difference in intensities between SIM 3, SIM 4 and SIM 5 is within 5%. Comparing SIM 4 and SIM 5, there is only a slight change ($\sim 1.5\%$) in the magnitude of stresses, which further hints that the effect of separation pattern is rather negligible compared to the dominance of the element height.

3.6 Summary

A benchmark study was carried out on the performance of four traditional RANS models, including the Standard k$-\varepsilon$, Realizable k$-\varepsilon$, Standard k$-\omega$ and SST k$-\omega$ models, for the turbulent pipeflow with a square bar roughness element at $Re = 1.56 \times 10^5$. Two bar element heights were

studied with $h/D = 0.05$ and 0.1. The correct prediction of the wake structures behind the roughness element proved to be challenging for most models compared to the experiments of Smits et al. (2019). All RANS models succeeded in predicting the mean wake features such as flow separation, recirculation and reattachment. The Standard k$-\varepsilon$ model performed the best overall, followed by the Realizable k$-\varepsilon$ model. The results from the SST k$-\omega$ model had the largest deviation from experiments. The difficulties in the computations using RANS models are partly attributed to the high-*Re* effects, and partly to the limitations in modeling flows with large pressure gradients.

The recovery of turbulent pipeflow over a square bar roughness element with a height of $0.05D$ and $0.1D$ was studied using the Standard k$-\varepsilon$ model. The rate of transport of shear stresses in case of $h/D = 0.1$ was higher compared to the thinner roughness element. The behavior and recovery of stresses exhibited the characteristics of a second-order flow response. In case of $h/D = 0.05$, this recovery was prolonged due to the slow transport of stresses towards the centerline. The tracing of the location of maximum Reynolds shear stresses downstream of the perturbation further provided evidence of prolonged recovery in case of a thinner bar roughness element. The correct length scale of recovery in the vicinity of roughness element is the bar-height (h), while in far-downstream region, the pipe radius (R) becomes the dominant scale for the flow recovery.

The flow response and recovery for multiple tandem bar roughness elements were examined using the thinner bar element with $h/D = 0.05$. First, the flow response was studied by comparing the reattachment lengths behind multiple perturbations to that of a single bar roughness. An asymptotic trend was observed in the reattachment lengths for placement of three or more square bar roughness elements. This was followed by investigating the effect of separation pattern between roughness elements on the flow recovery and response. In this case, the separation distance between consecutive elements was a function of the recirculation length of their upstream element. A sharp reduction in the reattachment lengths was observed due to the staggered separation pattern, hinting towards the impinging effect of upstream elements on subsequent roughness elements downstream. These observations suggest that upstream flow history plays an important role in reattachment of the flow.

Increasing the number of elements raised the rate of transport of stresses towards the centerline, hinting at a higher rate of turbulence production. However, there exists an asymptotic point at which increasing the number of elements beyond three does not significantly change the recovery of turbulent pipeflow. The separation pattern between the elements had negligible effects on the overall recovery process with the flow approaching the equilibrium value of stresses in far downstream region. Despite slight differences close to the bar roughness element, the flow diffuses towards the wall earlier with a staggered separation pattern compared to the periodic pattern. This leads to a faster recovery between $80 \leq x/h \leq 100$. However, the trend in recovery downstream of this point is similar to the periodic separation pattern.

The applications of multiple tandem roughness elements are myriad in the industry, especially in energy transport and sewage pipelines. It was observed that the pressure gradients increased downstream of the roughness element due to the sudden contraction-expansion of the flow in response to perturbation. Increased pressure gradients leads to increased turbulence behind the roughness element, as observed from the contours of turbulence production (P_k). Such increased turbulence behind the roughness element hints at enhanced turbulence mixing downstream. Thus the flow over roughness elements can be applied to the sewage transport pipelines to enhance mixing downstream of the roughness element and reduce slogging or blockages in the pipes due to accumulation of sludge in these pipelines. Also, it was observed that periodically initiating such changes led to transport of stresses away from the walls, hinting at a long region of low skin friction downstream of the roughness elements. The low skin friction leads to lower wall friction on the pipe walls. Thus, periodically initiating such perturbations could reduce the work requirements in energy transport pipelines as well as reduce the erosion of pipe walls.

Chapter 4

VISCOELASTIC TURBULENT PIPEFLOW

4.1 Introduction

The influence of viscoelastic polymer additives on response and recovery of turbulent pipeflow over square bar roughness elements are examined using Direct Numerical Simulations at Reynolds number of 5×10^3. Two different bar heights for the square bar roughness elements are examined, $h/D = 0.05$ and 0.1. Finitely Extensible Non-linear Elastic -Peterlin (FENE-P) rheological model is employed for modeling viscoelastic fluid features. The rheological parameters for the simulation correspond to high concentration polymer of $160ppm$. This chapter addresses the final objectives of the thesis outlined in Section 1.2. This chapter is prepared in such a way that the problem description in Section 4.3 is followed by discussion of results in Section 4.4, and conclusions in Section 4.5.

4.2 Background

Response and recovery of turbulent pipeflow to abrupt surface variations, i.e., roughness elements, is a fundamental study of non-equilibrium flow behavior with various industrial and engineering

applications. For example, extraction and transport of various heavy crude and petroleum products are routinely carried out using pipelines (Hart, 2014). The flow in most crude transport pipelines experience small eddies and near-wall turbulence, which increases frictional drag. This incurs heavy energy loses in transport of highly viscous fluids like crude or heavy-oil bitumen (Abdul-Hadi and Khadom, 2013). Thus, techniques for frictional drag reduction are of significant practical interest. It has been established that the addition of high molecular-weight non-Newtonian polymers in turbulent pipeflow produces upward of 80% drag reduction, and it significantly reduces turbulent frictional drag on the pipe walls (White and Mungal, 2008; White et al., 2004). This phenomenon was first reported by Toms (1948) and such polymer additives were named Drag-Reducing Agents (DRAs). Addition of such polymers causes the fluid to have elastic viscosity, as well as Newtonian viscosity, thus called viscoelastic fluids (Hanks, 2003). Polymer additives for purposes of drag reduction have been used successfully in many applications like transport of crude in pipelines (Burger et al., 1982), energy saving transport medium in residential heating devices (Takeuchi, 2012), as well as sewer (Sellin, 1978) and firefighting systems (Fabula, 1971).

Transport of energy related fluids through pipes and channels involve high Reynolds number, and in most practical cases includes turbulent flows over rough surfaces. Abrupt surface variations at high Reynolds numbers constitute a class of non-equilibrium or perturbed flows, which have been the focus of extensive research using Newtonian fluids. The behaviour of such flows is typically complex because the perturbations or step changes cause contraction in the flow, particularly at high Reynolds number. There are several studies that investigate different aspects of Newtonian fluid flow past wall-mounted obstacles or perturbations, and non-equilibrium flow conditions. Smits et al. (1979) studied the effects of abrupt surface variations on flow recovery and observed a second-order response, which led to long-lasting changes in the turbulent structures in the flow. This was followed by the study of Durst and Wang (1989), who investigated, experimentally and numerically, the flow response to an axisymmetric perturbation. They found an overshoot of flow response in the vicinity of the perturbation due to the mixed effects of sudden contraction and expansion, as opposed to sudden expansion in the flow over a backward facing step. Dimaczek et al.

(1989) observed similar effects for wall mounted axisymmetric perturbations over a wide range of Reynolds numbers. Studies of Jiménez (2004) and Smits et al. (2019) focused on turbulent flow over small step conditions or roughness elements, defined by the ratio of the lateral width of the object (h) with respect to the boundary layer width (δ_o), given as $h/\delta_o \ll 1$. These small step conditions were unique in terms of their effects on the overall flow response and downstream recovery. Smits et al. (2019) studied the flow response and recovery over two roughness heights of $h/D = 0.05$ and 0.1 at Reynolds number of 1.56×10^5 using Particle Image Velcotimetry (PIV). This study identified that the sudden contraction and expansion of the incoming flow resulted in longer reattachment lengths and amplification of the Reynolds stresses near the vicinity of the roughness element. For larger roughness elements, the downstream collapse of Reynolds stresses was sudden, whereas it extended far downstream for smaller roughness elements.

Extensive studies have looked at the effects of multiple, tandem wall mounted structures on flow response and overall flow dynamics. Leonardi et al. (2003) studied the flow response over tandem wall-mounted square bars, over a range of periodic separation ratios. It was determined that for large separation between two obstacles, the recirculation length was altered by the adverse pressure gradient imposed by the upstream wall of the subsequent object. Such flow behaviour was analogous to the study of wake characteristics behind flat plate by Hemmati et al. (2019). This was followed by the study of Goswami and Hemmati (2020) in Chapter 3, who investigated the effects of turbulent flow over multiple roughness elements and different separation patters on the flow response and recovery. They considered two roughness element heights of $h/D = 0.05$ and 0.1, as well as two separation patterns: periodic and staggered. It was determined that the flow recovery was prolonged by the use of smaller roughness element, while the separation patterns had negligible effects on the overall response and recovery as long as the elements are positioned outside the impinging zone of the upstream element. While the study on Newtonian flow past wall-mounted obstacles are abundant, viscoelastic fluid flow over such conditions have received limited attention despite its extensive industrial applications.

The numerical studies on viscoelastic flows mainly use Direct Numerical Simulations (DNS) (Favero et al., 2010; Tsukahara et al., 2011; Holmes et al., 2012; Azaiez et al., 1996; Dubief et al., 2013) and Reynolds-Averaged-Navier-Stokes (RANS) turbulence models (Resende et al., 2011, 2013). Experimentally, Particle Image Velocimetry (PIV) (Tsukahara et al., 2013b; Shaban et al., 2018) and Laser-Doppler-Velocimetry (LDV) (Samanta et al., 2013; Quinzani et al., 1994) are used to characterize the flow. Experimental studies mainly focus on investigating turbulence statistics, structure of polymeric flow, and the study of elastic instabilities over a wide range of sub-critical Reynolds numbers. DNS studies use one or more non-linear differential models such as Oldroyd-B model (Oldroyd, 1950), Giesekus model (Giesekus, 1982), Phan-Thein-Tanner (PTT) model (Phan-Thien, 1978), and Finitely Extensible Non-linear Elastic-Peterlin (FENE-P) model (Bird et al., 1987). These studies are limited to lower Reynolds numbers because of the complexities in terms of modeling various rheological behavior of the fluid and resolving various non-linear viscous and elastic effects (Macosko, 1994). Earlier numerical studies using DNS and several viscoelastic models were limited to smooth pipes, plane channel, and boundary layers. Azaiez et al. (1996) studied Giesekus, PTT and FENE-P models in simulating flow through 4:1 planar contraction. By comparing the performance of different rheological models with experimental results, it was determined that FENE-P model performed the best overall in terms of predicting the pressure drop, shear and normal stresses and drag reduction. This was followed by the work of Sureshkumar et al. (1997), who demonstrated the first DNS channel flow using viscoelastic fluid and FENE-P constitutive model. This study was performed at lower Reynolds numbers and a range of Weissenberg numbers (Wi, a dimensionless number characterizing the flow elasticity), to benchmark a set of criteria for onset of drag reduction in plane channel flows. The Finitely Extensible Non-linear Elastic (FENE) model was first proposed by Warner Jr (1972), as a solution to the gaps in linear spring model that had no restriction on deformation of polymer chain. This was further extended by Bird et al. (1987), who proposed the FENE-P model with Peterlin closure approximation. Here, the finite extension of the polymer chains were restricted by the parameter L^2, which is the dimensionless extensibility of the polymer chain. Since many such studies have

complimented its accuracy and compatibility with numerical simulations, FENE-P constitutive model is currently the most appropriate model for complex flow simulations.

Rothstein and McKinley (2001) investigated the flow of polystyrene-added fluid through contraction-expansion geometry of varying expansion ratio using LDA. They studied the effects of contraction-expansion geometries on the pressure drop due to flow contraction and wake characteristics. They determined that while the addition of polymer-additive in the fluid does reduce the overall pressure and skin-friction drag, the intensity of such reduction vastly depends on the concentration of the added polymer. This was followed by Poole and Escudier (2003), who investigated the influence of different polymer concentrations on the turbulent flow through planar sudden expansion using transverse LDA with a linear expansion ratio of 1.43. They observed that the reattachment lengths by low polymer-concentration fluids increased, while for higher concentrations it decreased significantly. The lower reattachment length was accompanied by a large reduction in turbulent intensity occurring at the point of flow separation for higher concentration solutions. Oliveira (2003) further numerically investigated the effects of axisymmetric abrupt expansion geometries using FENE rheological models for low Reynolds numbers and a range of Wi, polymer extensibility and concentrations. The results showed similarities with the findings of Poole and Escudier (2003), combined with a reduced pressure and skin-friction distribution along the walls. Further, Poole et al. (2007) performed experiments on viscoelastic flow over a backward-facing step with varying polyacrylamide-concentration solutions at Reynolds numbers of $10-100$. It was determined that as the polymer concentration increases, the combined effects of shear-thinning and viscoelasticity lead to reduced reattachment lengths behind the step, while an overshoot of velocity was observed compared to Newtonian fluid.

In recent years, there have been several studies that investigate the the effects of viscoelastic polymer additives on flow past bluff bodies and wall-mounted obstacles, as well as on the implications of viscoelasticity on Large-scale and Very-large scale motions. Xiong et al. (2013) carried out numerical simulations of two-dimensional flow past a circular cylinder using multiple rheological models and varying Reynolds number, Weissenberg number and polymer concentrations. An

overshoot of velocity gradients and stresses were observed in the vicinity of the cylinder at high polymer conversations, while the intensities of the overshoot was very low compared to Newtonian fluid. Further, as the Reynolds number increased, vortex shedding was observed for the Newtonian fluid, which reduced gradually with increasing polymer concentrations and Wi numbers. Tsukahara et al. (2014) performed DNS simulations of turbulent viscoelastic flows in a channel with wall mounted plates and studied the influence of viscoelasticity on turbulent structures and Large-scale motions behind the wall-mounted plates. They observed that for the Newtonian fluid, three pairs of large-scale vortices occur behind the plates, which was significantly weakened in the viscoelastic fluid. This suppression of vortices were influenced by the elastic and viscous forces, which resulted in a significant reduction of drag behind the plate and a decreased skin-friction on the surface of the plate. They also observed a slight increase in reattachment lengths behind the plate with lower polymer concentrations and a reduction at higher concentrations. These findings were in agreement with those of Tsukahara et al. (2013a) and Poole and Escudier (2003), who provided evidence of the mixed effects of elastic and viscous forces.

While investigations such as Dubief et al. (2013) and Shaban et al. (2018) extensively study the mechanisms of turbulent viscoelastic plane channel flows and smooth pipes, limited studies exist that investigate these effects with abrupt surface variations at high Reynolds numbers. Furthermore, viscoelastic flows past roughness elements and small-step ($h/\delta_o \ll 1$) conditions have not gained sufficient attention. Here, we examine the effects of viscoelastic fluid on flow over square bar roughness elements using DNS and FENE-P rheological constitutive model at Reynolds number of 5×10^3. Particularly, we investigate the influence of higher-polymer concentration viscoelastic fluid on the flow response and recovery over perturbed flow conditions. For clarity, the results are compared with Newtonian flow over roughness element at the same Reynolds number.

4.3 Problem Description

We examined the response and recovery of Newtonian and non-Newtonian turbulent fluid flow over square bar roughness elements of two different height using DNS at Reynolds number of 5×10^3. First, the simulations were carried out using water, a Newtonian fluid, as a benchmark simulation. This was followed by examining the effects of viscoelastic polymer additives using FENE-P rheological model incorporated into DNS. Finally, the results of viscoelastic simulations were compared with those of Newtonian DNS simulations to study the implications of viscoelastic fluid on the overall flow dynamics, response and recovery.

The governing equations for incompressible fluids are the continuity equation and the momentum equation, given by

$$\frac{\partial \boldsymbol{u_i}}{\partial x_i} \;=\; 0, \tag{4.1}$$

$$\rho\left(\frac{\partial \boldsymbol{u_i}}{\partial t} \;+\; \boldsymbol{u_j}\frac{\partial \boldsymbol{u_i}}{\partial x_j}\right) \;=\; \frac{\partial}{\partial x_j}\left[-p\delta_{ij} \;+\; \boldsymbol{\tau}_{ij}\right], \tag{4.2}$$

where u is the velocity vector, ρ is the fluid density, p is the isotropic pressure and $\boldsymbol{\tau}$ is the stress tensor. For Newtonian DNS simulations, the continuity (Equation 4.1) and momentum (Equation 4.2) equations were solved directly. For viscoelastic simulations, however, the stress tensor was split into a solvent or Newtonian stress component ($\boldsymbol{\tau}_s$) and a non-Newtonian or polymeric stress component ($\boldsymbol{\tau}_p$), such that

$$\boldsymbol{\tau} = \boldsymbol{\tau}_s + \boldsymbol{\tau}_p.$$

The Newtonian stress component is defined as $\boldsymbol{\tau}_s = 2\mu_s \boldsymbol{D}$, where μ_s is the solvent viscosity and $\boldsymbol{D}$ is the rate-of-strain tensor given by

$$\boldsymbol{D} = \frac{1}{2}\left(\nabla \cdot \boldsymbol{u} + \mid \nabla \cdot \boldsymbol{u} \mid^T\right).$$

Substituting this into Equation 4.2 gives a modified momentum equation:

$$\rho\left(\frac{\partial \boldsymbol{u_i}}{\partial t} \;+\; \boldsymbol{u_j}\frac{\partial \boldsymbol{u_i}}{\partial x_j}\right) \;-\; \frac{\partial}{\partial x_j}\left(\mu_s\left(\frac{\partial \boldsymbol{u_i}}{\partial x_j}+\frac{\partial \boldsymbol{u_j}}{\partial x_i}\right)\right) = \;\frac{\partial}{\partial x_j}\left[-p\delta_{ij} \;+\; \tau_{p,ij}\right], \tag{4.3}$$

where τ_p is defined in the multimode from ($\sum_{k=1}^{n}\tau_{pk}=0$) as a symmetric tensor (τ_{pk}) obtained by the sum of the contributions of individual relaxation modes. Majority of viscoelastic material are composed of molecular structures of different sizes, and therefore they have different relaxation times. The multimode formulation enables inclusion of a vast spectrum of relaxation times to obtain more realistic results. The expression of τ_{pk} depends on the viscoelastic constitutive equations employed. For viscoelastic simulations here, the polymeric stress tensor is computed using FENE-P model constitutive equation (Bird et al., 1987) as follows,

$$\left(1+\frac{\frac{3}{1-3/{L_k}^2}+\frac{\lambda_k}{\mu_{pk}}tr(\tau_{pk})}{{L_k}^2}\right)\tau_{pk} \;+\; \lambda_k\overset{\nabla}{\tau}_{pk} \;=\; 2\left(\frac{1}{1-3/{L_k}^2}\right)\mu_{pk}\cdot D, \tag{4.4}$$

where λ is the polymer relaxation time, L^2 is the extensibility of the polymer molecule, $\mathbf{tr}(\tau_p)$ is the trace of polymer stress tensor, and $\overset{\nabla}{\tau}_{pk}$ is the upper convected derivative given as

$$\overset{\nabla}{\tau}_{pk} = \frac{D\tau_{pk}}{Dt} - [\nabla\cdot\boldsymbol{u}\cdot\tau_{pk}] - [\nabla\cdot\boldsymbol{u}\cdot\tau_{pk}]^T, \tag{4.5}$$

and $\frac{D\tau_{pk}}{Dt}$ is the total derivative of the polymer-stress tensor, defined as

$$\frac{D\tau_{pk}}{Dt} = \frac{\partial\tau_{pk}}{\partial t} + \boldsymbol{u}\cdot\nabla\tau_{pk} \tag{4.6}$$

The simulation setup in the current study mimicked those of Favero et al. (2010) and Holmes et al. (2012), incorporating FENE-P rheological model in DNS using OpenFOAM, who have verified and validated the accuracy of the model. The FENE-P model was further validated by Dubief et al. (2013) in studying elasto-inertial turbulence.

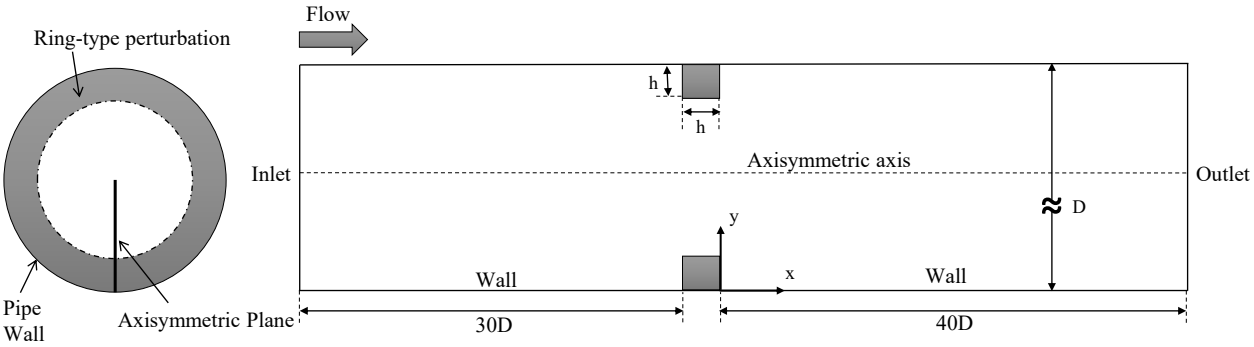

Figure 4.1: Schematic of the computational domain. (not to scale)

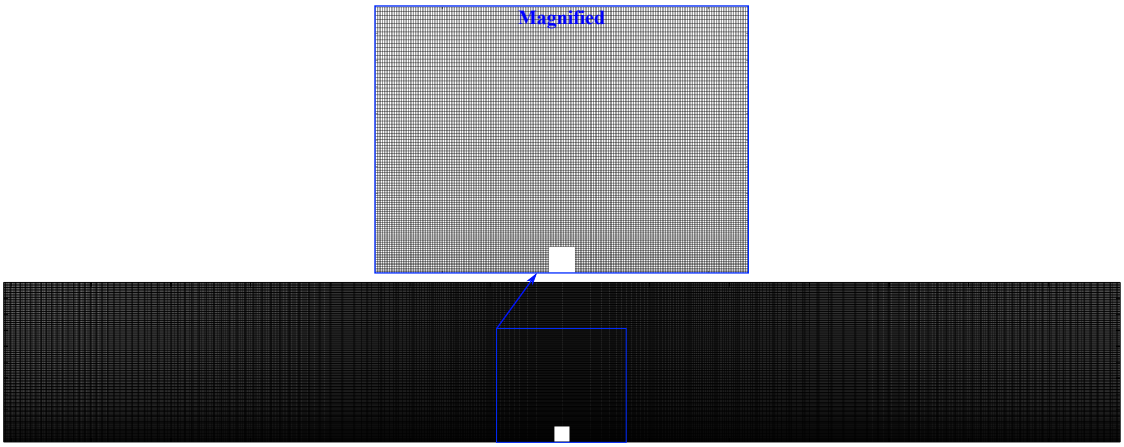

Figure 4.2: The spatial grid distribution with magnified box around the bar roughness element.

The schematics of the computational domain, as shown in Figure 4.1, was designed following the setup of Smits et al. (2019) and Yamagata et al. (2014), and it suitability is verified in Chapter 3 and Goswami and Hemmati (2020). All simulations are performed in an axisymmetric plane. The domain extends from $-30D$ to $+40D$ in $x-$direction, and $R = D/2$ in $y-$direction. The spatial grid is shown in Figure 4.2. The minimum spatial grid requirement for a DNS simulation was satisfied by coinciding the order of magnitude of element size, $O[\Delta x]$, with the order of magnitude of the kolmogorov length scales, $O[\eta]$, at the pipe walls and in the vicinity of the roughness element. Kolmogorov length scales are calculated using $\eta = (\nu_s{}^3/\varepsilon)^{1/4}$, based on Newtonian fluid viscosity, where ε is the mean dissipation rate. Table 4.1 shows the grid resolution of the current grid as a variation of $\Delta x/\eta$ in the axial direction upto $x/D = 8$. The $\Delta x/\eta$ was less than 4 at least upto $x/D = 8$, while near the vicinity of roughness element they were below ~ 2.06. These ratios

Table 4.1: Grid resolution, $\Delta x/\eta$, for current DNS study.

Case $x/D =$	**1**	**2**	**5**	**8**
Current Case	2.06	2.27	2.90	3.54
Hemmati et al. (2018)	1.85	2.59	3.24	3.97
Ashrafian et al. (2004)	≈ 3.2	–	–	–
Dubief et al. (2013)	≈ 2.3	–	–	–

Table 4.2: Parameters space for the current study.

Parameter	**Value**
Extensibility of the polymer, L^2	200
Ratio of solvent to zero-shear viscosity, β	0.22
Polymer relaxation time, λ (s)	0.023
Weissenberg number, Wi	0.65
Pipe radius-base Weissenberg number, Wi_R	0.16
Reynolds number, Re_D	5000
Frictional Reynolds number, Re_τ	682

were comparable to other DNS studies on wakes (Hemmati et al., 2018) and viscoelastic pipeflows (Ashrafian et al., 2004; Dubief et al., 2013).

The parameters used in the simulations are given in Table 4.2. For all viscoelastic simulations, the non-dimensional extensibility (L^2) and parameter β are fixed at 200 and 0.22, where β is defined as the ratio of solvent viscosity to the zero-shear viscosity of the polymer solution, given by $\beta = \mu_s/(\mu_s + \mu_p)$. The parameter β is selected to obtain a shear-thinning solution behaviour. λ is the polymer relaxation time, which is obtained experimentally by Shaban et al. (2018) for a solution of polyacrylamide polymer at 160 ppm. The Weissenberg number defined based on wall-shear is $Wi = \lambda\dot{\gamma} = 0.65$, and based on pipe radius is $Wi_R = \lambda U_b/R = 0.16$. All simulations are performed at $Re_D = \rho D U_b/\mu_s = 5 \times 10^3$, defined by pipe diameter (D) and Newtonian viscosity (μ_s). Using the friction factor correlation given by McKeon et al. (2004), the Newtonian upstream friction velocity corresponded to the friction Reynolds number of $Re_\tau = \rho D u_\tau/\mu_s = 682$. The Reynolds number based on the square bar height and solvent viscosity was 250 and 500, and the linear expansion ratios are 1.11 and 1.25, for $h/D = 0.05$ and 0.1, respectively.

Identical boundary conditions were used for all the simulations. The inlet boundary condition was a constant uniform velocity, $u = U_b$. The separation distance between the inlet and the roughness element was kept sufficiently long to satisfy the hydrodynamic entrance length condition at this Reynolds number. A Neumann-type outflow condition based on $\partial\varphi/\partial n = 0$, where φ is any flow variable, was imposed at the outlet, and a no-slip type boundary condition was imposed at the walls and the roughness element. The timestep, Δt, for all simulations was set so that the maximum Courant-Friedrichs-Lewy (CFL) number remains below 0.5 for Newtonian simulations and 0.2 for viscoelastic simulations. The smaller timestep requirement for viscoelastic simulations guarantee the boundedness of $\boldsymbol{\tau}_{pk}$. All simulations were performed using OpenFOAM, an open-source finite-volume-method platform. All discretized equations were solved using PimpleFoam, a transient solver for incompressible, turbulent flow. PimpleFoam solver incorporates the PIMPLE algorithm (OpenCFD, 2019), which is the combination of PISO (Pressure Implicit with Splitting of Operator) and SIMPLE (Semi-Implicit Method for Pressure-Linked Equations) algorithms. The second-order accurate and bounded numerical discritization schemes for spatial, and backward Euler scheme for temporal discritization were employed for the simulations. The convective term was descritized using second-order central difference schemes. The convergence criterion of 10^{-6} was set for the root-mean-square of momentum residuals, for each timestep. The convergence was guaranteed by running all simulations for ten through-times, where a through-time is defined as the time fluid takes to travel from inlet to outlet without any disturbance. All simulations were completed using 48 CPUs and 192 GB of memory on Compute Canada clusters.

4.4 Results And Discussion

We begin by looking at the viscoelastic fluid flow response over the square bar roughness element. The Newtonian fluid flow simulation is our base flow to establish the differences due to non-Newtonian fluid effects. This is followed by investigation of flow recovery and the distributions of pressure and wall shear stresses by the viscoelastic fluid.

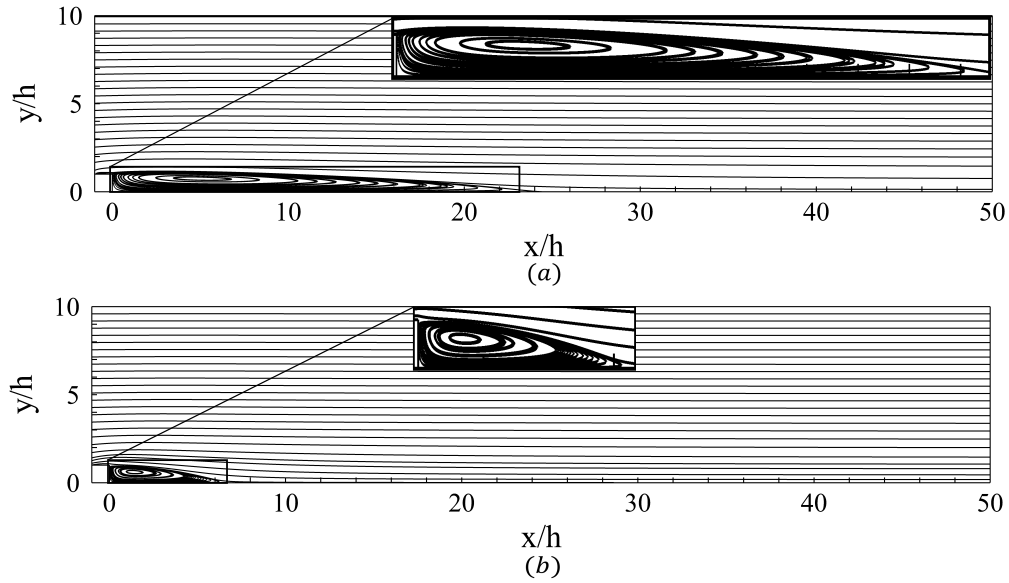

Figure 4.3: Streamline plot of time-averaged (mean) axial velocity for the (a) Newtonian fluid and (b) Viscoelastic fluid flow past roughness element of bar height $h/D = 0.05$.

4.4.1 Flow Response

The flow response is evaluated by studying the nature of the mean wake features behind the roughness element. Figures 4.3 and 4.4 show the mean streamline plots for Newtonian and viscoelastic fluid, for two roughness heights. For all cases, the flow separation occurs at the upstream edge of the roughness element, followed by the formation of a recirculation bubble before the flow reattaches to the bulk flow in the downstream region of the roughness element. From the first glance, it is evident that the longitudinal width (length) of the separation bubble for viscoelastic fluid in Figures 4.3b and 4.4b is significantly smaller than to that of the Newtonian fluid in Figures 4.3a and 4.4a, respectively. Furthermore, the lateral width (height) of the recirculation bubble, in case of the Newtonian fluid, exceeds that of the roughness element by $\sim 5\%$ for $h/D = 0.05$ and $\sim 15\%$ for $h/D = 0.1$. For viscoelastic fluid, however, the lateral width of the recirculation bubble does not exceed the height of the roughness element for both bar heights.

A quantitative comparison of the recirculation lengths obtained from Newtonian and viscoelastic flow past roughness element is shown in Table 4.3. For the smaller roughness height, the mean recirculation length formed by the viscoelastic fluid exhibits a difference of $\sim 73\%$ from that of

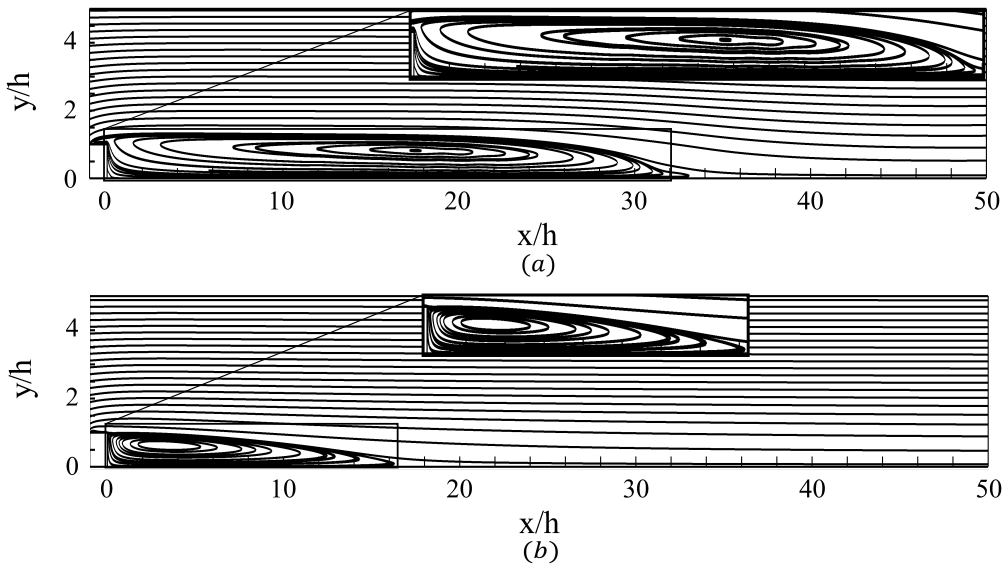

Figure 4.4: Streamline plot of time-averaged (mean) axial velocity for the (a) Newtonian fluid and (b) Viscoelastic fluid flow past roughness element of bar height $h/D = 0.1$.

Table 4.3: The recirculation length for Newtonian and non-Newtonian flows over roughness elements.

Study	h/D	$\overline{L_r}/h$	$\Delta\overline{L_r}(\%)$
Newtonian	0.05	23.28	–
Viscoelastic	0.05	6.28	73
Newtonian	0.1	34.18	–
Viscoelastic	0.1	17.18	49.74

the Newtonian fluid. For the larger roughness height, the difference observed is $\sim 50\%$. For Newtonian fluid, the reattachment length differs between the two bar heights by $\sim 32\%$. Since the larger bar element ($h/D = 0.1$) creates a larger contraction in the flow, it leads to a larger pressure gradient compared to that of the smaller square element. Thus, both the recirculation bubble and the reattachment length are larger for Newtonian flow over roughness element of height $h/D = 0.1$ compared to the smaller element. Viscoelastic fluid, on the contrary, creates larger pressure losses due to mixed effects of viscous and elastic forces. Thus even for larger roughness element, the effects of pressure gradients are not significant, leading to shorter recirculaiton lengths compared to that of the Newtonian fluid. These observations are consistent with the findings of Tsukahara et al. (2013a) and Poole and Escudier (2003) for higher concentration of polymer additives.

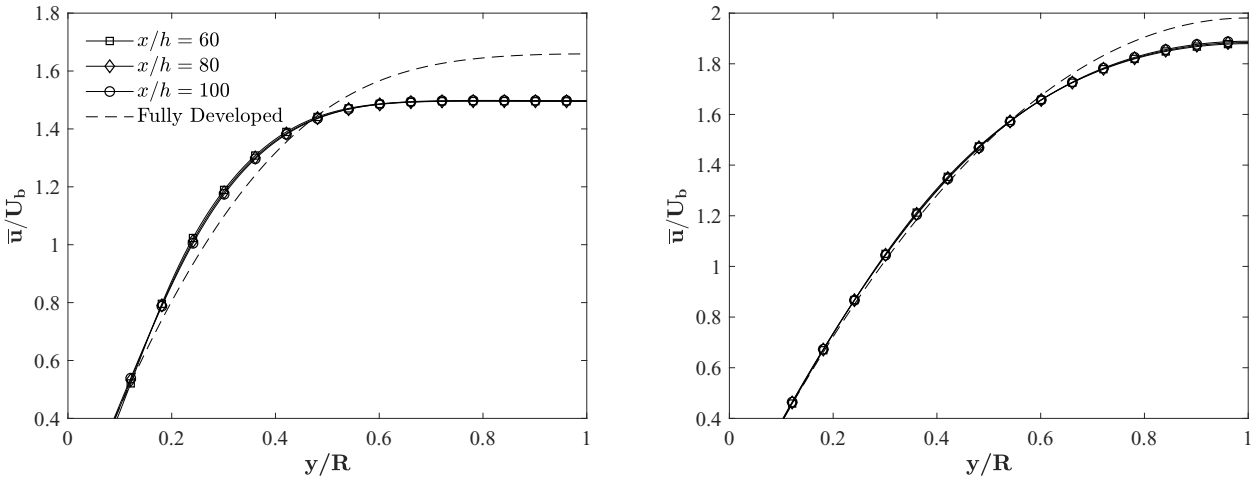

(a) Newtonian Flow

(b) Viscoelastic Flow

Figure 4.5: Mean axial velocity profiles at different axial locations ($x/h = 60, 80$ and 100) for bar height $h/D = 0.05$

The profiles of mean axial velocity obtained from Newtonian and viscoelastic fluids are shown in Figures 4.5 and 4.6 for $h/D = 0.05$ and 0.1, respectively. Profiles are plotted at three different axial locations downstream of the roughness elements: $x/h = 60, 80$ and 100. For Newtonian fluid (Figures 4.5a and 4.6a), the profiles for different bar height cases are quiet distinct. In case of $h/D = 0.05$, the velocity near the centre at $x/h = 60$ is $\sim 8\%$ below the fully developed profile. As the flow progresses, the variations at $x/h = 100$ become negligible near the centre. This is while slight variations ($\sim 0.2\%$) are observed close to the wall. In contrast, the velocity profiles for $h/D = 0.1$ show faster progression towards the fully developed profiles with $\sim 5\%$ difference at the centre between $x/h = 60$ and 100. Smits et al. (2019) state that the velocity for smaller roughness element exceeds the fully developed profile, while that of a larger roughness element is over-flattened by Reynolds shear stresses. The trends of velocity profiles observed here contrast the trends observed by Smits et al. (2019) at $Re = 1.56 \times 10^5$, which hints at the effects of Reynolds number on the flow dynamics and scaling. This finding agrees with experiments of Hultmark et al. (2012), who recorded similar effects in pipeflow with velocity in the centre of the pipe scaling with increasing Reynolds number.

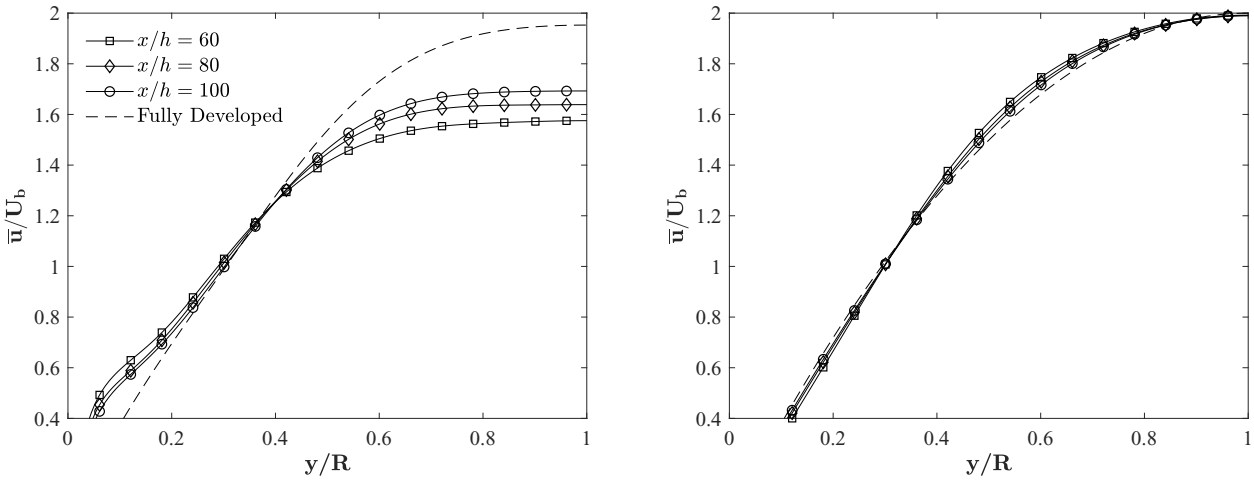

(a) Newtonian Flow

(b) Viscoelastic Flow

Figure 4.6: Mean axial velocity profiles at different axial locations ($x/h = 60, 80$ and 100) for bar height $h/D = 0.1$

In case of Viscoelastic fluids (Figures 4.5b and 4.6b), the velocity profiles vastly differ from the trends observed for Newtonian cases. For both bar heights, the velocities appear to have recovered close to fully developed profiles as early as $x/h = 60$. For $h/D = 0.05$, the velocity at $y = R$ is slightly ($\sim 2.5\%$) below that of the fully developed profile. As the flow progresses between $x/h =$ 60 and 100, the variation in velocity is negligible, showing a trend similar to that of Newtonian flow over the smaller roughness element ($h/D = 0.05$). In the case of larger square bar, the velocity close to $y = R$ appears to have recovered to fully developed profile, while slight variations are observed in $0.2 \ll y/R \ll 0.8$. For viscoelastic fluid, the bulk Reynolds number based on fluid viscosity ($\mu_o = \mu_s + \mu_p$) has reduced to $Re_o = \rho D U_b/\mu_o = 1060$ from $Re_D = 5000$ based on Newtonian solvent viscosity. Thus, the profiles of velocity appear to have a laminar nature, while the peak velocities remain high.

4.4.2 Flow Recovery

The recovery of mean flow is analyzed by tracing the transport of Reynolds shear stresses ($-\overline{u'v'}$), tubrulence kinetic energy production (P_k) and turbulence dissipation (ε). Figures 4.7 and 4.8 show the profiles of Reynolds shear stresses obtained from Newtonian and Viscoelastic fluids for $h/D =$

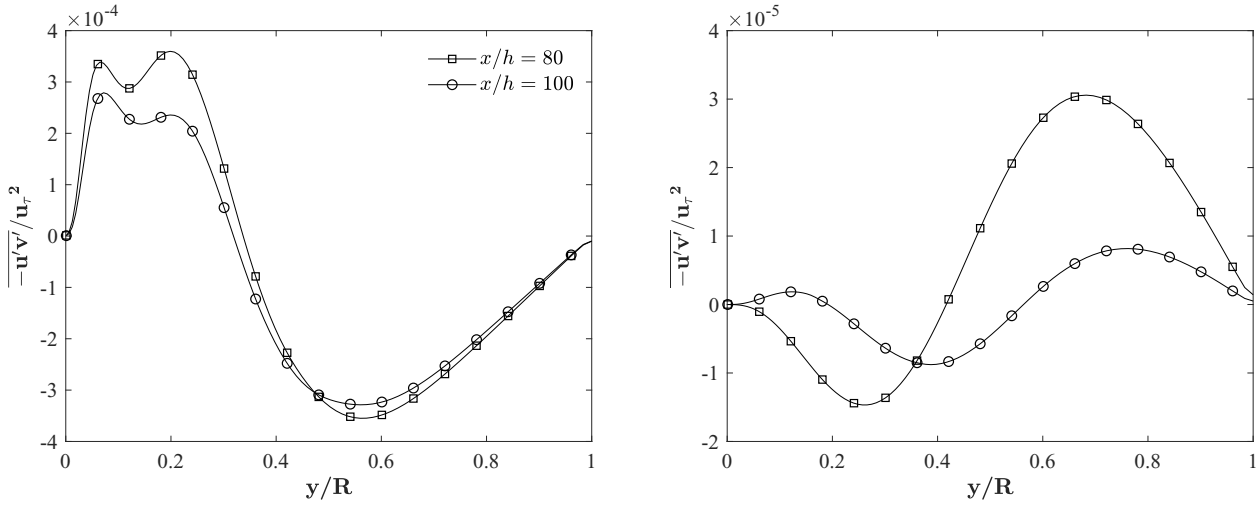

(a) Newtonian Flow (b) Viscoelastic Flow

Figure 4.7: Comparison of Reynolds shear stresses at different axial locations behind a roughness height of $h/D = 0.05$.

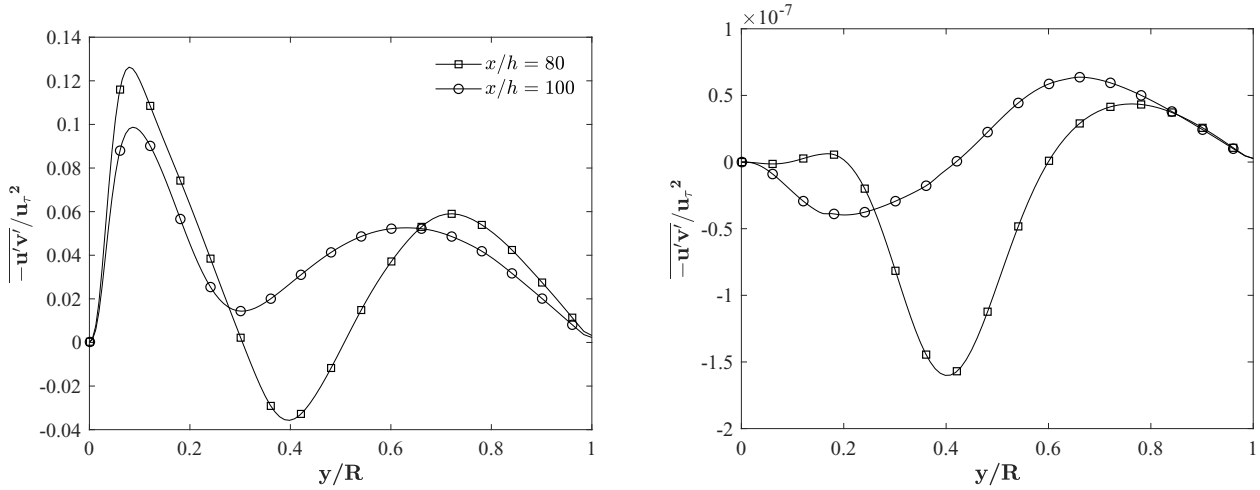

(a) Newtonian Flow (b) Viscoelastic Flow

Figure 4.8: Comparison of Reynolds shear stresses at different axial locations behind a roughness height of $h/D = 0.1$.

0.05 and 0.1, respectively. The profiles of $-\overline{u'v'}$ are traced at two streamwise locations, $x/h = 80$ and 100. Stresses are normalized by the Newtonian shear velocity ($u_\tau{}^2$). In case of Newtonian fluid (Figures 4.7a and 4.8a), high intensity of Reynolds shear stresses occur close to the wall for both roughness heights. As the flow progresses between $x/h = 80$ and 100, the stresses close to the wall start to dissipate. For viscoelastic fluid (Figures 4.7b and 4.8b), the trend is opposite. The

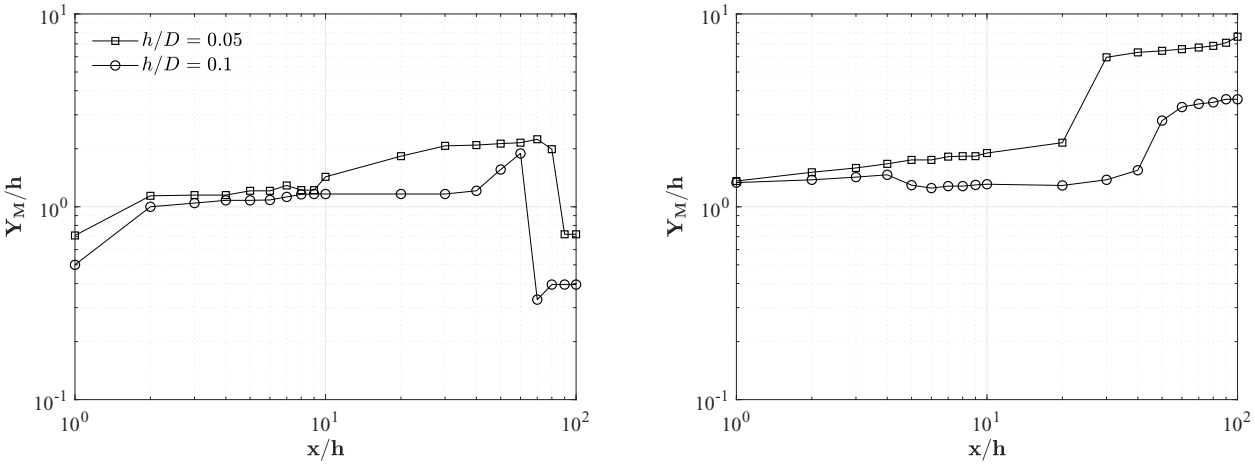

(a) Newtonian Flow

(b) Viscoelastic Flow

Figure 4.9: Location of the maximum Reynolds shear stress downstream of the roughness element. Y_M is normalized by roughness height h.

higher intensity of stresses appear to be away from the wall, close to $y/R \approx 0.8$, while in near-wall region the stresses are highly diminished. This suggests a loss of near-wall turbulence that induces frictional drag on the walls of the pipe. As the flow progresses to $x/h = 100$, a collapse of stresses close to the wall is observed, while the intensity of stresses near the center of the pipe remain high. Furthermore, it is apparent from the profiles that the overall intensity of Reynolds stresses for viscoelastic fluid flow is significantly lower compared to that of Newtonian fluid for both bar heights. This is an indicator of the overall stress reduction in the flow.

The recovery behaviour is quantified by tracing location of the maximum Reynolds shear stress (Y_M) as a function of streamwise axial locations (x/h). Figure 4.9 shows the profiles of Y_M normalized by roughness height (h). Initially, the high intensity of $-\overline{u'v'}$ remain close to $y = h$ for Newtonian fluid cases. As the flow progresses further downstream, in the region $10 \ll x/h \ll 60$, stresses start to dissipate away from the wall for $h/D = 0.05$, while they remain flat for $h/D = 0.1$. A sudden collapse of stresses towards the walls is observed for larger square bar at $x/h = 60$, while for smaller roughness the collapse is prolonged by a small distance, occurring at $x/h = 80$. This sudden collapse of Reynolds shear stresses towards the wall suggests a second-order response. While this phenomenon is well documented in Chapter 3 as well as by Smits et al. (2019) and

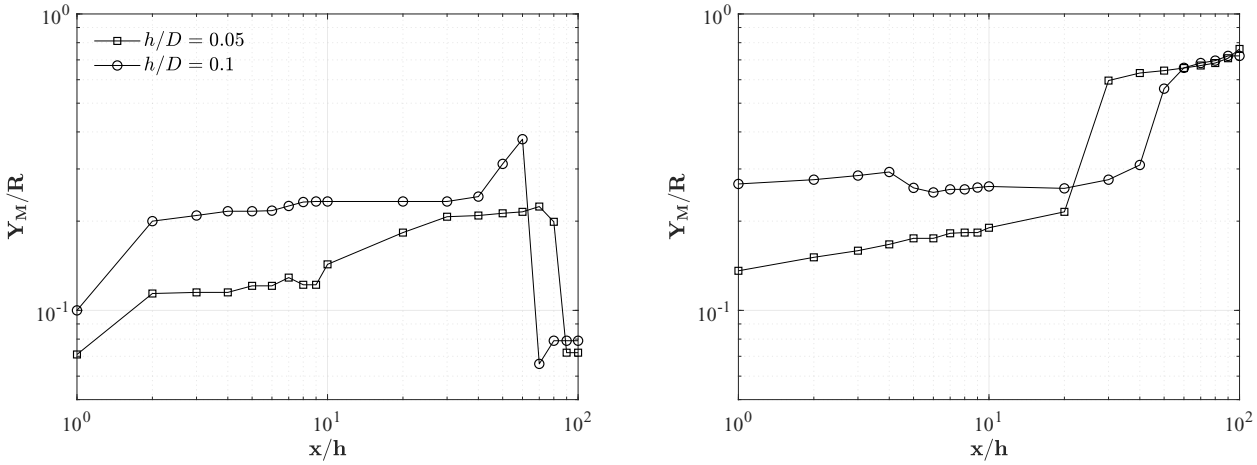

(a) Newtonian Flow

(b) Viscoelastic Flow

Figure 4.10: Location of the maximum Reynolds shear stress downstream of the roughness element. Y_M is normalized by roughness height R.

Goswami and Hemmati (2020) at $Re = 1.56 \times 10^5$, the collapse of stresses in the current study is confined within $x/h = 100$, suggesting a strong dependence of the recovery behaviour on the Reynolds number. In case of viscoelastic fluid cases, higher intensity stresses in the vicinity of the roughness remain further away from the wall, close to $y \approx 1.5h$. As the flow progresses further downstream, a sudden diffusion of high intensity stresses towards the centre of the pipe is observed. For the smaller square bar, this sudden climb towards the centre occurs close to $x/h = 20$, while it is prolonged to $x/h = 50$ for the larger roughness. Following the abrupt climb, the stresses remain at an equilibrium location past $x/h = 100$.

Normalizing Y_M by the pipe radius (R) in Figure 4.10 shows that the data collapses in the far-downstream region. For Newtonian fluid, this collapse is consistent with the observations from Chapter 3 and the findings of Smits et al. (2019) and Goswami and Hemmati (2020). A similar collapse is attained with viscoelastic fluid. The collapse in data suggests that the roughness height (h) is the dominant length scale in the vicinity of the roughness element. As the flow progresses further in the far-downstream region, the pipe radius comes into effect, and R becomes the dominant length scale for recovery. In case of viscoelastic fluid, as observed earlier, the location of maximum Reynolds shear stresses appears to be at equilibrium near the centre of the pipe. Further

downstream data will be required to confirm the effects of the dominant length scale (R) on the recovery of $-\overline{u'v'}$ by viscoelastic fluid. However, it is apparent that the recovery and response is delayed by the viscoelastic effects of the non-Newtonian fluid.

Since the behaviour of Reynolds stress is significantly different between Newtonian and viscoelastic cases, we focus on tracing the energy budget terms to further examine the turbulence fields. For Newtonian fluid, the production and dissipation terms based on definitions of Pope (2001) are:

$$P_k = -\overline{u_i' u_j'} \frac{\partial \overline{u_i}}{\partial x_j}, \tag{4.7}$$

$$\varepsilon = \nu_s \overline{\frac{\partial u_i}{\partial x_j} \frac{\partial u_i}{\partial x_j}}, \tag{4.8}$$

and for viscoelastic fluid, the production term remains the same as Newtonian fluid, while the dissipation term (Dubief et al., 2013) changes to:

$$\varepsilon = \nu_s \beta \overline{\frac{\partial u_i}{\partial x_j} \frac{\partial u_i}{\partial x_j}}. \tag{4.9}$$

Here, β is the ratio of solvent viscosity (μ_s) and zero-shear viscosity (μ_o) of the solution.

The profiles from turbulence kinetic energy production (P_k) and dissipation (ε) are shown in Figure 4.11 for $h/D = 0.05$. The profiles are drawn along the wake centreline, as a function of downstream axial locations (x/h). Although the turbulence budget terms for $h/D = 0.1$ are not shown here for brevity, a similar and expected trend is observed for both bar height cases using Newtonian and non-Newtonian fluids alike. Here, an initial drop in production near the vicinity of the roughness element is followed by a peak at the stagnation point. The intensity of the peak in production for the Newtonian fluid appears to be significantly larger and farther downstream, compared to that of viscoelastic fluid. This hints at the difference in prediction of reattachment lengths by both fluids. As the flow progresses downstream, P_k for the viscoelastic fluid subsides to equilibrium. For Newtonian fluid, the recovery prolongs farther downstream past $x/h = 100$, till

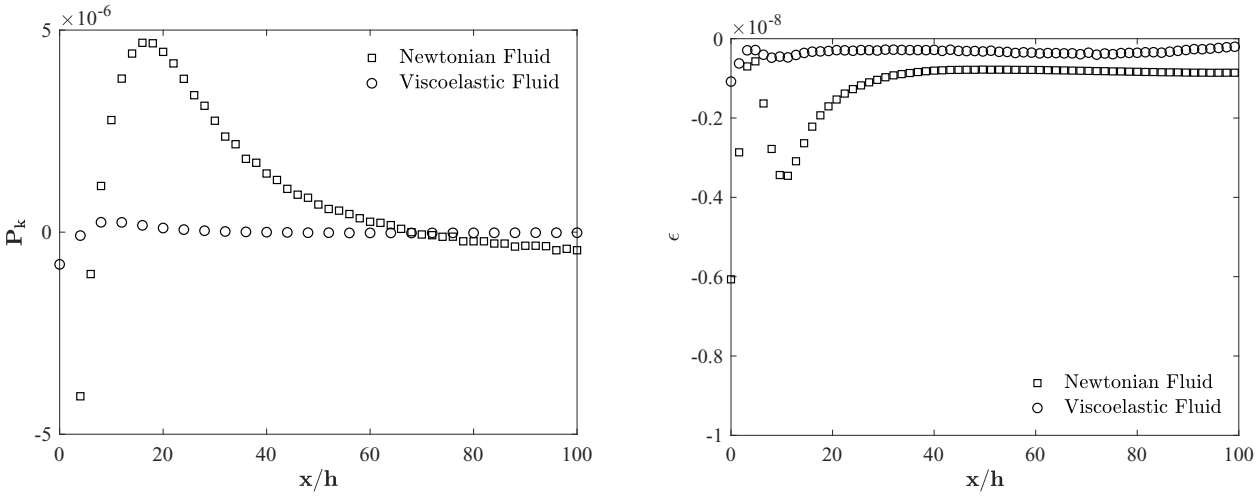

(a) Production (b) Dissipation

Figure 4.11: Turbulence kinetic energy production and dissipation in the wake of $h/D = 0.05$ roughness element along the wake centreline.

the end of the domain at $x/h = 400$. In the same manner, a higher rate of dissipation in the vicinity of the roughness element is followed by a negative peak for dissipation at the stagnation point. The dissipation for the viscoelastic fluid subsides earlier than the Newtonian fluid case, while another rise in dissipation is observed at $x/h = 10$ for the Newtonian fluid. In both bar height cases, the production and dissipation by viscoelastic fluid approach equilibrium values faster. Moreover, the intensity of turbulence production and dissipation is significantly lower for the viscoelastic fluid compared to the Newtonian fluid. This highlights another major effect of viscoelasticity on the response and recovery of the flow.

4.4.3 Distribution of pressure and wall shear stresses

Effects of viscoelasticity on the flow characteristics and the roughness element are more clearly illustrated in the distributions of pressure and skin friction. This begins by analyzing the contribution of skin friction and pressure drag on the overall local drag acting on the perturbation surfaces. The distribution of pressure and wall shear stresses are defined by pressure coefficient (C_p) and

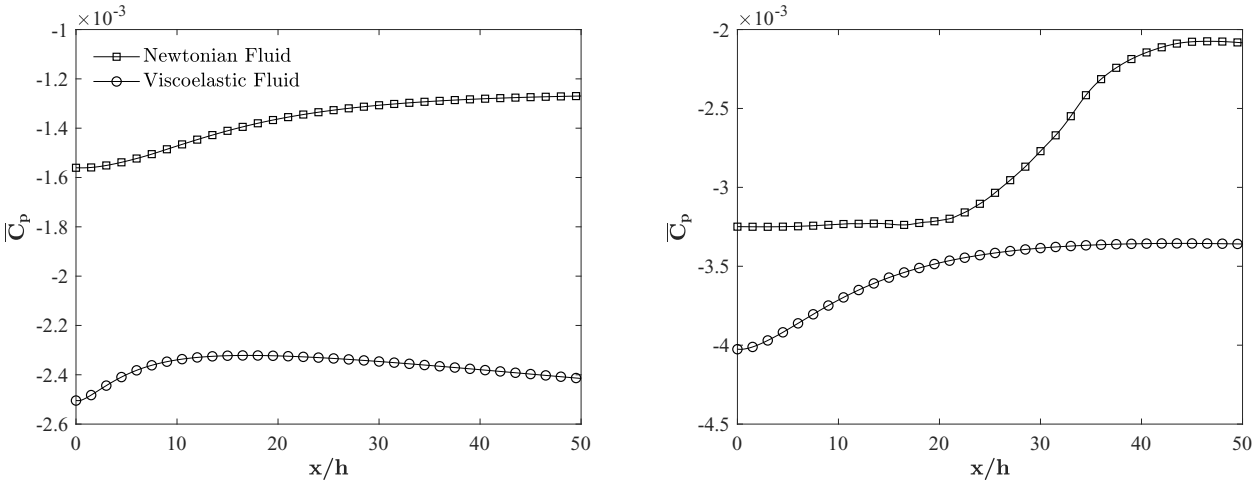

(a) $h/D = 0.05$ (b) $h/D = 0.1$

Figure 4.12: Pressure distribution on the pipe all behind both bar heights at $x/h = 0 - 50$.

skin friction coefficients (C_f), respectively. Coefficient of pressure is given as

$$C_p = (p - p_\infty)/\frac{1}{2}\rho {U_b}^2,$$

where p_∞ is the static pressure of the incoming flow. Similarly, the skin friction coefficient is given as

$$C_f = \tau_w/\frac{1}{2}\rho {U_b}^2,$$

where τ_w is the wall shear stress.

The distribution of mean pressure coefficient ($\overline{C_p}$) is examined in Figures 4.12 for both roughness heights. The profiles are drawn along the wall for $x/h = 0 - 50$ downstream of the roughness elements. For the Newtonian fluid, the pressure rises abruptly after $x/h \sim 5$ in case of $h/D = 0.05$, while for $h/D = 0.1$, the sudden increase in pressure occurs at $x/h \sim 20$. These locations roughly determine the locations of the centre of the recirculation bubble behind the roughness element. This is in good agreement with Leonardi et al. (2003) and Hemmati et al. (2019), who state that the flow starts experiencing the adverse pressure gradients downstream of the centre of the recirculation bubble. In the case of viscoelastic fluid, however, the initial increase in the pressure is

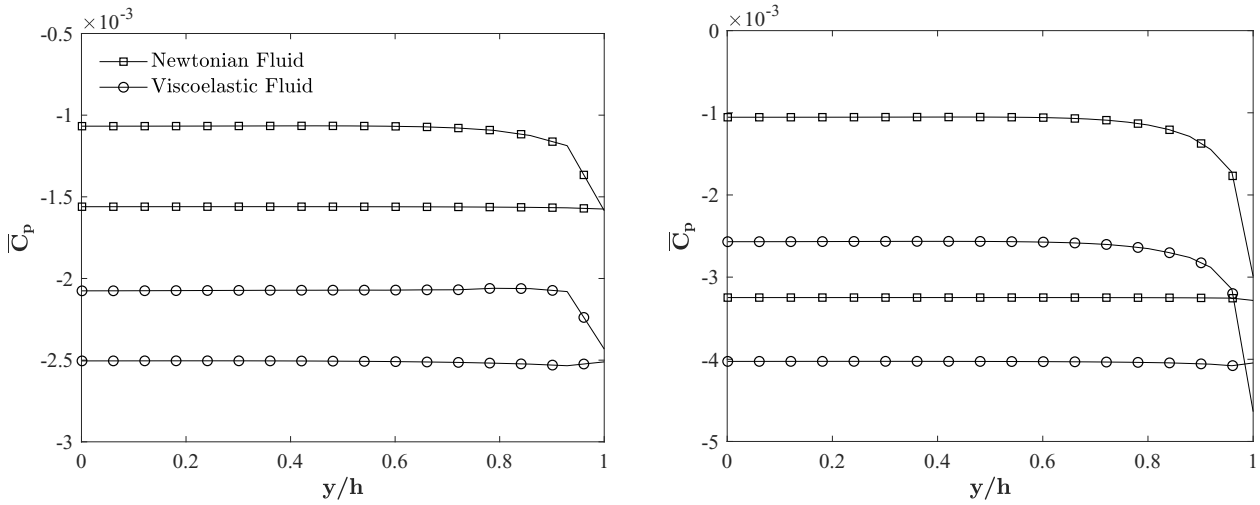

(a) $h/D = 0.05$ (b) $h/D = 0.1$

Figure 4.13: Mean pressure coefficient along the roughness element upstream and downstream surfaces.

noted near the stagnation point. Farther downstream, pressure reduces for the smaller bar height ($h/D = 0.05$), while it stabilizes for $h/D = 0.1$. For the latter, the pressure will drop as the flow progresses downstream. This suggests that the high pressure gradients formed due to the increased near-wall turbulence for Newtonian flow dissipate quickly in case of viscoelastic fluid. Thus, it facilitates the flow recovery towards an equilibrium state faster.

The profiles of mean skin friction coefficient on the upstream and downstream faces of the roughness element are shown in Figure 4.13. Here, it is apparent that the larger roughness element produces greater pressure loss with Newtonian fluid. This observation is consistent with the work of Liu et al. (2019) on Newtonian flow over an array of periodic roughness elements. Similarities are observed with viscoelastic fluid, where the pressure losses for a larger element is higher than that of the smaller element. Furthermore, pressure on the surfaces of the roughness element is significantly smaller for the Viscoelastic fluid compared to the Newtonian fluid for both bar height cases. This hints at a reduction in generated drag on the perturbation surfaces due to the Viscoelastic fluid effects.

The distribution of pressure and skin friction on the top surface of the perturbation is shown in Figures 4.14 and 4.15. There is an initial drop in pressure predicted for all cases, followed by

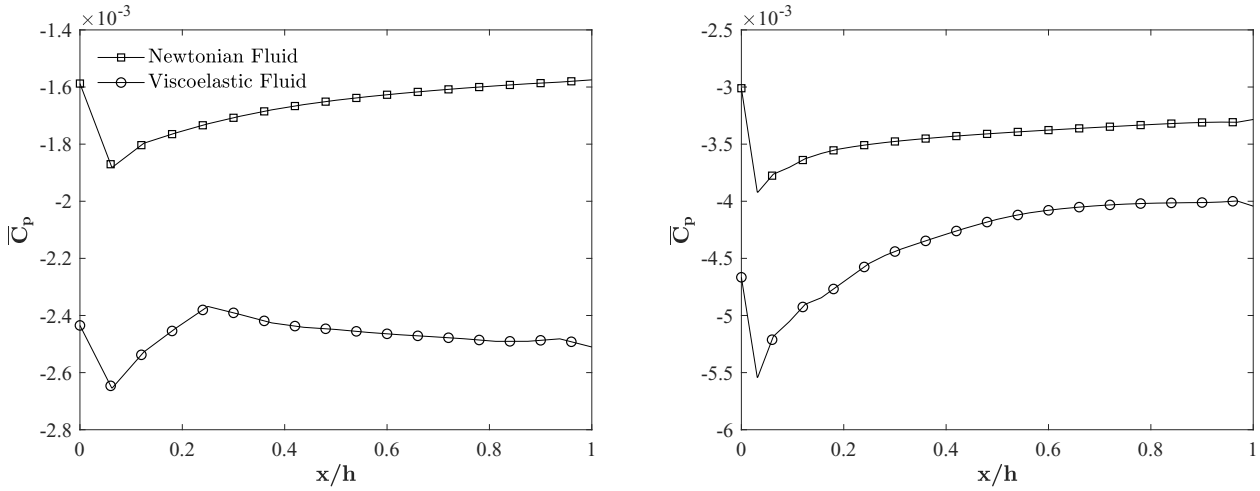

(a) $h/D = 0.05$ (b) $h/D = 0.1$

Figure 4.14: Mean pressure coefficient along the top surface of the roughness element.

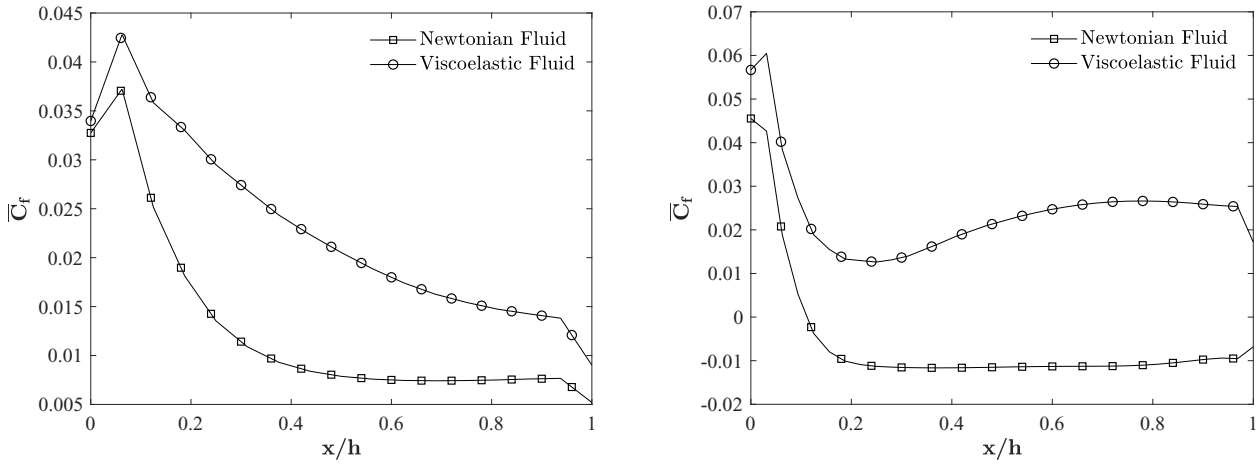

(a) $h/D = 0.05$ (b) $h/D = 0.1$

Figure 4.15: Wall shear stress distribution along the top surface of the roughness elements.

a gradual increase. The location of initial collapse in pressure suggests a strong average pressure gradient formed by flow separation on the leading edge of the roughness element. This suggest a local flow acceleration, which is evident by the sharp initial rise in skin friction from Figure 4.15. As the flow progresses forward, a sudden increase in pressure near the walls (see Figures 4.12) and a drop in skin friction indicate that the effects of viscosity become an important parameter affecting the response and recovery. Furthermore, the pressure losses are higher for the larger roughness

element in both fluids. The pressure losses for the viscoelastic fluid is significantly lower than that observed for the Newtonian fluid. In case of Newtonian fluid, the pressure coefficient increases again upto $x/h = 1$ for both element heights. The skin friction (Figure 4.15) is initially large, but then it experiences a rapid reduction to an equilibrium constant value for both bar heights, reflecting the acceleration of the flow near the leading edge. Negative skin friction occurs for $h/D = 0.1$, indicating the existence of a recirculating region on the top of the roughness.

For viscoelastic fluid, the initial drop in pressure is followed by a gradual increase to becoming relatively constant near the downstream edge of the roughness element. The pressure losses for the larger bar is higher compared to the smaller bar, following the trend of the Newtonian fluid. The skin friction for $h/D = 0.05$ drops gradually upto $x/h = 0.9$, before an abrupt drop is observed near the downstream face of the roughness. For the larger bar element ($h/D = 0.1$), it increases to achieve a constant value suggesting that the flow is accelerating near the downstream edge. This may be due to fact that, as mentioned before, the larger bar element extends outside the boundary layer, where as the smaller bar height is submerged in the boundary layer. The magnitude of the skin friction is higher in the Viscoelastic flow, which hints at higher contribution of viscous stresses to the local drag induced on the roughness. This is while the contribution of pressure drag due to the larger pressure losses on the front and back surfaces of the roughness element is lowered. Thus the overall induced drag on the roughness element is reduced with viscoelastic fluid, leading to smaller a recirculation region and a faster recovery.

4.5 Summary

The implications of viscoelastic fluid on the response and recovery of turbulent flow over two roughness element heights ($h/D = 0.05$ and 0.1) are examined using Direct Numerical Simulations at $Re = 5 \times 10^3$. For viscoelastic simulations, Finitely Extensible Non-linear Elastic-Peterlin (FENE-P) rheological model is considered and the rheological parameters correspond to a high-molecular weight polymer additive with concentration of $160ppm$. The response behaviour was

evaluated by studying the mean wake features behind the roughness element. The streamline contours for viscoelastic fluid showed a shorter recirculating region for both bar heights compared to that of the Newtonian fluid. The lateral width of the recirculating bubble did not extend above the height of the roughness element contrary to the Newtonian flow. The reattachment length was significantly reduced by $\sim 73\%$ and $\sim 50\%$ for $h/D = 0.05$ and 0.1, respectively. The larger roughness element created larger contraction in the flow, which was noticeable from the Newtonian fluid case. Due to larger pressure losses as a result of mixed effects of viscous and elastic forces in viscoelastic fluid, the effects of pressure gradients are not significant, even for the larger roughness element. Thus, it leads to a shorter reattachment length. Looking at the velocity field, the progression of velocity was slower for the smaller bar height compared to the larger element in Newtonian flow. For viscoelastic fluid, the velocity near the centre of the pipe appeared to have recovered close to the fully developed profile for the smaller roughness element, while a full recovery was observed for the larger element with only slight variations.

The profiles of Reynolds shear stresses ($-\overline{u'v'}$) for viscoelastic fluid were significantly diminished near the walls, indicating the loss of near-wall turbulence structure. Furthermore, the overall stress for both roughness heights was lower compared to the Newtonian fluid. For viscoelastic fluid, large stresses in the vicinity of the roughness element remained farther away from the wall compared to the Newtonian fluid. A collapse of stresses towards the wall was noted for the latter in the far-downstream region, while the stresses remained close to the centre of the pipe in the case of viscoelastic flow. In the far-downstream, the recovery depended on the pipe radius, which was determined to be the dominant length scale. The turbulence production and dissipation subside to equilibrium in viscoelastic cases, while their recovery is prolonged by the Newtonian fluid. The difference in prediction of production and dissipation terms by both fluids provided more evidence of the shorter reattachment lengths in the vicinity of the roughness element. It also indicated a different behaviour for the Reynolds shear stresses in the wake.

The distribution of pressure on the pipe wall downstream of the roughness element determined the location of the centre of the separation region, after which the flow starts experiencing adverse

pressure gradient effects. The pressure for viscoelastic fluid appeared to subside to an equilibrium state faster than the Newtonian fluid cases. The distribution of pressure on the front and back surfaces of the roughness element indicated a larger pressure loss by the viscoelastic fluid compared to the Newtonian fluid. Furthermore, the pressure loss by larger element with viscoelastic fluid flow was greater than that of the smaller element, an observation similar to that of Newtonian cases. This suggests the dominance of the roughness height as a prominent parameter in perturbed flows.

The contribution of viscous stresses to the overall local drag in viscoelastic flow was higher on the top surface of the roughness element, while that of pressure drag was lowered due to large pressure losses. Thus, the overall localized drag on the roughness element was greatly reduced for viscoelastic fluid, which led to a faster recovery.

Chapter 5

CONCLUSIONS

The main objectives of this thesis involved characterization of the response and recovery of turbulent pipeflow perturbed by different configurations of roughness elements at moderate to high Reynolds number. Particularly, this thesis first considered the effect of multiple roughness elements, with different sizes and separation patterns, on flow recovery and response. Then, it examined the implications of viscoelasticity on the flow response and recovery past roughness elements of different sizes. Using computational fluid dynamics simulations, this thesis focused on turbulent pipeflow dynamics with axisymmetric perturbations introduced through square (cross-sectional ring type) roughness elements of height $h/D = 0.05$ and 0.1. The simulations were performed at a range of Reynolds numbers, $Re = 5 \times 10^3 - 1.56 \times 10^5$. Direct numerical simulation (DNS) was employed at lower Reynolds numbers, while RANS-based simulations were performed for higher Reynolds number.

A validation study was carried out to benchmark the performance of four RANS-based turbulence models, including the Standard k$-\varepsilon$, Realizable k$-\varepsilon$, Standard k$-\omega$ and SST k$-\omega$ models, in predicting the high pressure gradient flow past the roughness elements. It was determined that, while all turbulence models show discrepancy in prediction of the flow features, Standard k$-\varepsilon$ model performed the best overall, showing the closest results to the experiments. This was followed by analysis of the flow response and recovery due to a single square bar roughness elements

of two different heights using the best performing turbulence model. It was observed that the smaller roughness element, $h/D = 0.05$, prolonged the recovery, while that of $h/D = 0.1$ was faster. A second order response was noted in the transport of stresses. The hypothesis stated in the study of Smits et al. (2019) was confirmed through this work, observing that the dominant length scale of recovery in the vicinity of the roughness element was the bar height (h), while in the far-downstream region, pipe radius (R) affected the recovery.

The flow response and recovery to multiple tandem roughness elements were examined using the smaller roughness height of $0.05D$. The novelty of this work was on investigating the effects of increasing number of roughness elements in flow recovery, and the influence of different separation patterns between them. It was determined that the the flow response became asymptotic with placement of three or more roughness elements in periodic arrangement. The reattachment lengths behind each roughness element was different. The asymptotic response was attributed to such upstream history arising from the geometry. The flow recovery remained constant after three elements or more, and with increasing number of elements, the rate of transport of Reynolds shear stresses towards the centre of the pipe increased.

Periodic and staggered separation patterns were also investigated. While the effect of staggered pattern on recovery was negligible, the flow response showed distinct differences. The separation ratios between each element in staggered pattern was a function of the reattachment length observed from the periodic placement. A sharp reduction of reattachment lengths were observed due to the staggered pattern between four roughness elements, which suggested the impinging influence on the subsequent element placed in close proximity of the upstream element.

The later portion of this work studied the implications of viscoelastic or non-Newtonian fluid flow perturbed by square bar roughness element. The novelty of this study was to understand the implications of viscoelastic fluid features on the response and recovery of perturbed flow. This work added to the narrow pool of literature concerning viscoelastic fluid flows at turbulent, perturbed, high Reynolds number flow conditions.

The analysis was carried out using FENE-P rheological model incorporated to DNS for examining the effects of viscoelasticity at $Re = 5 \times 10^3$. Similar to the previous investigation, two roughness heights of $0.05D$ and $0.1D$ were considered. The results showed significant differences in the response behaviour of the viscoelastic flow over roughness elements. The reattachment lengths were significantly reduced behind the roughness element, compared to Newtonian flow, attributing to the mixed effects of viscous and elastic forces in viscoelastic fluid. The centreline velocity appeared to have recovered close to the fully developed profile, while that of Newtonian flow was slower. Reynolds stresses close to the wall, in case of viscoelastic flow, were significantly diminished, which suggested the loss of near-wall turbulence structures. The Recovery behaviour was further examined by comparing the transport of Reynolds shear stresses in the downstream region of the roughness elements, with that of the Newtonian fluid. The high intensity of Reynolds stresses remained close to the centre of the pipe, while for Newtonian flow, they appeared to be close to the wall. Further analysis of the turbulence kinetic energy production (P_k) and dissipation (ε) shed light on the different response and recovery behaviour of both fluids.

Lastly, the distributions of pressure coefficient and skin friction on the roughness element surfaces and downstream walls were studied. A large pressure loss was observed on the front and back surfaces of the roughness element with viscoelastic flow. Further, the distribution of pressure on the pipe walls showed that the pressure by viscoelastic fluid normalized to equilibrium faster than Newtonian flow. Skin friction deficits in the same region confirmed the shorter reattachment lengths by viscoelastic flow.

5.1 Future Work

The observations of this study provide a framework to improve our understanding of the perturbed non-equilibrium turbulent flows. While a significant analysis was provided on the behavior of flow response and recovery, with both Newtonian and viscoelasic fluid, some remaining unchallenged questions require further research, mainly:

(1) The Reynolds number scaling of the recovery by perturbed flows. Here the investigations of scaling behaviour of recovery mechanism will be performed over a range of Reynolds numbers, incorporating laminar, transition and turbulence regimes. As an extension, the scaling of recovery mechanism based on roughness height will also be considered;

(2) Differences in the wake response of axisymmetric versus plane perturbation;

(3) Analysis of flow recovery in a fully-rough turbulent flow. The study of Liu et al. (2019) defined a fully rough laminar flow by periodically initiating small-step, tandem perturbations over a long region to analyze the fully-developed state with such roughness. Similar study can be performed at turbulent Reynolds numbers, with varying separation gaps and roughness heights to analyze the flow resover over fully rough turbulent flows.

Further investigations are thus required in these areas using DNS.

Bibliography

Abdul-Hadi, A. A. and Khadom, A. A. (2013). Studying the effect of some surfactants on drag reduction of crude oil flow. *Chinese Journal of Engineering*, 2013:6.

Adams, E. and Johnston, J. (1988). Effects of the separating shear layer on the reattachment flow structure part 2: Reattachment length and wall shear stress. *Experiments in Fluids*, 6(7):493–499.

Akbari, O. A., Toghraie, D., and Karimipour, A. (2015). Impact of ribs on flow parameters and laminar heat transfer of water–aluminum oxide nanofluid with different nanoparticle volume fractions in a three-dimensional rectangular microchannel. *Advances in Mechanical Engineering*, 7(11):1687814015618155.

Ashrafian, A., Andersson, H. I., and Manhart, M. (2004). Dns of turbulent flow in a rod-roughened channel. *International Journal of Heat and Fluid Flow*, 25(3):373–383.

Azaiez, J., Guénette, R., and Ait-Kadi, A. (1996). Numerical simulation of viscoelastic flows through a planar contraction. *Journal of non-newtonian fluid mechanics*, 62(2-3):253–277.

Bai, H., Zhan, Z., Liu, J., and Ren, Z. (2019). From local structure to overall performance: An overview on the design of an acoustic coating. *Materials*, 12(16):2509.

Balachandar, R. (1990). *Characteristics of separated flows including cavitation effects*. PhD thesis, Concordia University.

Balakumar, B. and Adrian, R. (2007). Large-and very-large-scale motions in channel and boundary-layer flows. *Philosophical Transactions of the Royal Society A: Mathematical, Physical and Engineering Sciences*, 365(1852):665–681.

Balasubramanya, A., Kohlstädt, S., and Nilsson, H. (2016). Viscoelasticity and constitutive relations.

Barman, K., Debnath, K., and Mazumder, B. (2019). Turbulence over chains of hemispherical ribs under waves in a current. *Water Resources Research*, 55(1):55–75.

Baskaran, A. and Kashef, A. (1996). Investigation of air flow around buildings using computational fluid dynamics techniques. *Engineering Structures*, 18(11):861–875.

Bird, R. B., Armstrong, R. C., and Hassager, O. (1987). Dynamics of polymeric liquids. vol. 1: Fluid mechanics.

Bradshaw, P. and Wong, F. (1972). The reattachment and relaxation of a turbulent shear layer. *Journal of Fluid Mechanics*, 52(1):113–135.

Burger, E. D., Munk, W. R., Wahl, H. A., et al. (1982). Flow increase in the trans alaska pipeline through use of a polymeric drag-reducing additive. *Journal of petroleum Technology*, 34(02):377–386.

CAPP, R. (2019). 2019 crude oil forecast, markets and transportation.

Cappelli, D. and Mansour, N. N. (2013a). Performance of reynolds averaged navier-stokes models in predicting separated flows: study of the hump flow model problem. In *31st AIAA Applied Aerodynamics Conference*, page 3154.

Cappelli, D. and Mansour, N. N. (2013b). Performance of reynolds averaged navier-stokes models in predicting separated flows: study of the hump flow model problem. In *31st AIAA Applied Aerodynamics Conference*, page 3154.

Chan, L., MacDonald, M., Chung, D., Hutchins, N., and Ooi, A. (2018). Secondary motion in turbulent pipe flow with three-dimensional roughness. *Journal of Fluid Mechanics*, 854:5–33.

Choi, H., Lee, J., and Park, H. (2014). Aerodynamics of heavy vehicles. *Annual Review of Fluid Mechanics*, 46:441–468.

Corten, G. P. (2001). Flow separation on wind turbine blades. *University of Utrecht*.

Cui, J., Patel, V. C., and Lin, C.-L. (2003). Large-eddy simulation of turbulent flow in a channel with rib roughness. *International Journal of Heat and Fluid Flow*, 24(3):372–388.

Diaz-Daniel, C., Laizet, S., and Vassilicos, J. (2017). Direct numerical simulations of a wall-attached cube immersed in laminar and turbulent boundary layers. *International Journal of Heat and Fluid Flow*, 68:269 – 280.

Dimaczek, G., Tropea, C., and Wang, A.-B. (1989). Turbulent flow over two-dimensional, surface-mounted obstacles: plane and axisymmetric geometries. In *Advances in Turbulence 2*, pages 114–121. Springer.

Dominy, R. (1992). Aerodynamics of grand prix cars. *Proceedings of the Institution of Mechanical Engineers, Part D: Journal of Automobile Engineering*, 206(4):267–274.

Doolan, C. J. and Moreau, D. J. (2016). Flow-induced noise generated by sub-boundary layer steps. *Experimental Thermal and Fluid Science*, 72:47–58.

Dubief, Y., Terrapon, V. E., and Soria, J. (2013). On the mechanism of elasto-inertial turbulence. *Physics of Fluids*, 25(11):110817.

Durst, F., Founti, M., and Wang, A.-B. (1989). Experimental investigation of the flow through an axisymmetric constriction. In *Turbulent Shear Flows 6*, pages 338–350. Springer.

Durst, F. and Tropea, C. (1983). Flows over two-dimensional backward—facing steps. In *Structure of Complex Turbulent Shear Flow*, pages 41–52. Springer.

Durst, F. and Wang, A.-B. (1989). Experimental and numerical investigations of the axisymmetric, turbulent pipe flow over a wall-mounted thin obstacle. In *7th Symposium on Turbulent Shear Flows, Volume 1*, volume 1, pages 10–4.

Dutta, P., Saha, S. K., Nandi, N., and Pal, N. (2016). Numerical study on flow separation in 90 pipe bend under high reynolds number by k-ε modelling. *Engineering Science and Technology, an International Journal*, 19(2):904–910.

Eiamsa-ard, S., Ridluan, A., Somravysin, P., Promvonge, P., and Chok, N. (2008). Numerical investigation of turbulent flow through a circular orifice. *KMITL Sci. J*, 8(1):44–50.

Eshghinejadfard, A., Sharma, K., and Thévenin, D. (2017). Effect of polymer and fiber additives on pressure drop in a rectangular channel. *Journal of Hydrodynamics*, 29(5):871–878.

Fabula, A. G. (1971). Fire-fighting benefits of polymeric friction reduction.

Farhadi, M. and Rahnama, M. (2006). Large eddy simulation of separated flow over a wall-mounted cube.

Favero, J., Secchi, A., Cardozo, N., and Jasak, H. (2010). Viscoelastic flow analysis using the software openfoam and differential constitutive equations. *Journal of non-newtonian fluid mechanics*, 165(23-24):1625–1636.

Fogaing, M. B. T., Hemmati, A., Lange, C. F., and Fleck, B. A. (2019). Performance of turbulence models in simulating wind loads on photovoltaics modules. *Energies*, 12(17):3290.

George, W. K. (2013). Lectures in turbulence for the 21st century. *Chalmers University of Technology*.

Giesekus, H. (1982). A simple constitutive equation for polymer fluids based on the concept of deformation-dependent tensorial mobility. *Journal of Non-Newtonian Fluid Mechanics*, 11(1-2):69–109.

Goswami, S. and Hemmati, A. (2020). Response of turbulent pipeflow to multiple square bar roughness elements at high reynolds number. *Physics of Fluids*, 32(7):075110.

Gursul, I., Cleaver, D., and Wang, Z. (2014). Control of low reynolds number flows by means of fluid–structure interactions. *Progress in Aerospace Sciences*, 64:17–55.

Hanks, R. W. (2003). Fluid dynamics (chemical engineering). In Meyers, R. A., editor, *Encyclopedia of Physical Science and Technology (Third Edition)*, pages 45 – 70. Academic Press, New York, third edition edition.

Hart, A. (2014). A review of technologies for transporting heavy crude oil and bitumen via pipelines. *Journal of Petroleum Exploration and Production Technology*, 4(3):327–336.

Hemmati, A., Wood, D. H., and Martinuzzi, R. J. (2018). On simulating the flow past a normal thin flat plate. *Journal of Wind Engineering and Industrial Aerodynamics*, 174:170–187.

Hemmati, A., Wood, D. H., and Martinuzzi, R. J. (2019). Wake dynamics and surface pressure variations on two-dimensional normal flat plates. *AIP Advances*, 9(4):045209.

Holmes, L., Favero, J., and Osswald, T. (2012). Numerical simulation of three-dimensional viscoelastic planar contraction flow using the software openfoam. *Computers & chemical engineering*, 37:64–73.

Hooke, R. (1678). *De Potentia Restitutiva*, or of spring. explaining the power of springing bodies, london.

Hucho, W. and Sovran, G. (1993). Aerodynamics of road vehicles. *Annual review of fluid mechanics*, 25(1):485–537.

Hultmark, M., Vallikivi, M., Bailey, S. C. C., and Smits, A. (2012). Turbulent pipe flow at extreme reynolds numbers. *Physical review letters*, 108(9):094501.

Hussein, H. J. and Martinuzzi, R. (1996). Energy balance for turbulent flow around a surface mounted cube placed in a channel. *Physics of Fluids*, 8(3):764–780.

Ilman, M. et al. (2014). Analysis of internal corrosion in subsea oil pipeline. *case studies in Engineering Failure Analysis*, 2(1):1–8.

Jasak, H. (1996). Error analysis and estimation for the finite volume method with applications to fluid flows.

Jiménez, J. (2004). Turbulent flows over rough walls. *Annu. Rev. Fluid Mech.*, 36:173–196.

Johnson, D. A. and King, L. (1985). A mathematically simple turbulence closure model for attached and separated turbulent boundary layers. *AIAA journal*, 23(11):1684–1692.

Jovic, S. and Driver, D. (1995). Reynolds number effect on the skin friction in separated flows behind a backward-facing step. *Experiments in Fluids*, 18(6):464–467.

Kaneda, M., Yu, B., Ozoe, H., and Churchill, S. W. (2003). The characteristics of turbulent flow and convection in concentric circular annuli. part i: flow. *International Journal of Heat and Mass Transfer*, 46(26):5045–5057.

Katz, J. (2006). Aerodynamics of race cars. *Annu. Rev. Fluid Mech.*, 38:27–63.

Kim, J., Kline, S., and Johnston, J. (1980). Investigation of a reattaching turbulent shear layer: flow over a backward-facing step.

Kim, T., Kato, S., and Murakami, S. (2001). Indoor cooling/heating load analysis based on coupled simulation of convection, radiation and hvac control. *Building and Environment*, 36(7):901–908.

Kiya, M. and Sasaki, K. (1983). Structure of a turbulent separation bubble. *Journal of Fluid Mechanics*, 137:83–113.

Langelandsvik, L. I., Kunkel, G. J., and Smits, A. J. (2008). Flow in a commercial steel pipe. *Journal of Fluid Mechanics*, 595:323–339.

Launder, B. E. and Spalding, D. B. (1983). The numerical computation of turbulent flows. In *Numerical prediction of flow, heat transfer, turbulence and combustion*, pages 96–116. Elsevier.

Leonardi, S., Orlandi, P., and Antonia, R. A. (2007). Properties of d-and k-type roughness in a turbulent channel flow. *Physics of fluids*, 19(12):125101.

Leonardi, S., Orlandi, P., Smalley, R., Djenidi, L., and Antonia, R. (2003). Direct numerical simulations of turbulent channel flow with transverse square bars on one wall. *Journal of Fluid Mechanics*, 491:229–238.

Lin, J., Howard, F., and Selby, G. (1991). Exploratory study of vortex-generating devices for turbulent flow separation control. In *29th aerospace sciences meeting*, page 42.

Liu, F. (2016). A thorough description of how wall functions are implemented in openfoam. In Nilsson, H., editor, *Proceedings of CFD with OpenSource Software*.

Liu, Y., Li, J., and Smits, A. J. (2019). Roughness effects in laminar channel flow. *Journal of Fluid Mechanics*, 876:1129–1145.

Macosko, C. W. (1994). Rheology principles. *Measurements and Applications*.

Martinuzzi, R. and Tropea, C. (1993). The flow around surface-mounted, prismatic obstacles placed in a fully developed channel flow (data bank contribution).

Martinuzzi, R. J. and Havel, B. (2000). Turbulent flow around two interfering surface-mounted cubic obstacles in tandem arrangement. *J. Fluids Eng.*, 122(1):24–31.

McKeon, B., Swanson, C., Zagarola, M., Donnelly, R., and SMITS, A. J. (2004). Friction factors for smooth pipe flow. *Journal of Fluid Mechanics*, 511:41–44.

Mendes, P. S., Braga, A., Azevedo, L., and Correa, K. (1999). Resistive force of wax deposits during pigging operations.

Menter, F. and Esch, T. (2001). Elements of industrial heat transfer predictions. In *16th Brazilian Congress of Mechanical Engineering (COBEM)*, volume 109, page 650.

Menter, F. R., Kuntz, M., and Langtry, R. (2003). Ten years of industrial experience with the sst turbulence model. *Turbulence, heat and mass transfer*, 4(1):625–632.

Miyake, Y., Tsujimoto, K., and Nakaji, M. (2001). Direct numerical simulation of rough-wall heat transfer in a turbulent channel flow. *International Journal of Heat and Fluid Flow*, 22(3):237–244.

Mollicone, J.-P., Battista, F., Gualtieri, P., and Casciola, C. M. (2017). Effect of geometry and reynolds number on the turbulent separated flow behind a bulge in a channel. *Journal of Fluid Mechanics*, 823:100–133.

Morrison, G. L., Deotte Jr, R. E., Nail, G. H., and Panak, D. L. (1993). Mean velocity and turbulence fields inside a β= 0.50 orifice flowmeter. *AIChE journal*, 39(5):745–756.

Nagano, Y., Hattori, H., and Houra, T. (2004). Dns of velocity and thermal fields in turbulent channel flow with transverse-rib roughness. *International Journal of Heat and Fluid Flow*, 25(3):393–403.

Nygård, F. and Andersson, H. (2013). Numerical simulation of turbulent pipe flow through an abrupt axisymmetric constriction. *Flow, turbulence and combustion*, 91(1):1–18.

Okamoto, S., Seo, S., Nakaso, K., and Kawai, I. (1993). Turbulent shear flow and heat transfer over the repeated two-dimensional square ribs on ground plane. *Journal of Fluids Engineering*, 115(4).

Oldroyd, J. G. (1950). On the formulation of rheological equations of state. *Proceedings of the Royal Society of London. Series A. Mathematical and Physical Sciences*, 200(1063):523–541.

Oliveira, P. J. (2003). Asymmetric flows of viscoelastic fluids in symmetric planar expansion geometries. *Journal of non-newtonian fluid mechanics*, 114(1):33–63.

OpenCFD, O. (2019). The open source computational fluid dynamics (cfd) toolbox.

Paik, J., Sotiropoulos, F., and Porté-Agel, F. (2009). Detached eddy simulation of flow around two wall-mounted cubes in tandem. *International Journal of Heat and Fluid Flow*, 30(2):286 – 305.

Paterson, D. and Apelt, C. (1989). Simulation of wind flow around three-dimensional buildings. *Building and Environment*, 24(1):39–50.

Perić, M. and Tropea, C. (1993). Turbulent flow over surface-mounted obstacles in plane and axisymmetric geometries. In *Physics of Separated Flows—Numerical, Experimental, and Theoretical Aspects*, pages 18–26. Springer.

Phan-Thien, N. (1978). A nonlinear network viscoelastic model. *Journal of Rheology*, 22(3):259–283.

Poole, R. and Escudier, M. (2003). Turbulent flow of non-newtonian liquids over a backward-facing step: Part ii. viscoelastic and shear-thinning liquids. *Journal of non-newtonian fluid mechanics*, 109(2-3):193–230.

Poole, R., Escudier, M., Afonso, A., and Pinho, F. (2007). Laminar flow of a viscoelastic shear-thinning liquid over a backward-facing step preceded by a gradual contraction. *Physics of Fluids*, 19(9):093101.

Pope, S. B. (2001). Turbulent flows.

Ptasinski, P., Nieuwstadt, F., Van Den Brule, B., and Hulsen, M. (2001). Experiments in turbulent pipe flow with polymer additives at maximum drag reduction. *Flow, Turbulence and Combustion*, 66(2):159–182.

Quinzani, L. M., Armstrong, R. C., and Brown, R. A. (1994). Birefringence and laser-doppler velocimetry (ldv) studies of viscoelastic flow through a planar contraction. *Journal of Non-Newtonian Fluid Mechanics*, 52(1):1–36.

Ravindran, S. (1999). Active control of flow separation over an airfoil.

Resende, P., Kim, K., Younis, B., Sureshkumar, R., and Pinho, F. (2011). A fene-p k–ε turbulence model for low and intermediate regimes of polymer-induced drag reduction. *Journal of Non-Newtonian Fluid Mechanics*, 166(12-13):639–660.

Resende, P., Pinho, F., Younis, B., Kim, K., and Sureshkumar, R. (2013). Development of a low-reynolds-number k-ω model for fene-p fluids. *Flow, turbulence and combustion*, 90(1):69–94.

Roache, P. J. (1982). Scaling of high-reynolds-number weakly separated channel flows. In *Numerical and Physical Aspects of Aerodynamic Flows*, pages 87–98. Springer.

Rothstein, J. P. and McKinley, G. H. (2001). The axisymmetric contraction–expansion: the role of extensional rheology on vortex growth dynamics and the enhanced pressure drop. *Journal of non-newtonian fluid mechanics*, 98(1):33–63.

Roussinova, V. (2009). Turbulent structures in smooth and rough open channel flows: effect of depth.

Samanta, D., Dubief, Y., Holzner, M., Schäfer, C., Morozov, A. N., Wagner, C., and Hof, B. (2013). Elasto-inertial turbulence. *Proceedings of the National Academy of Sciences*, 110(26):10557–10562.

Schlichting, H. and Gersten, K. (2016). *Boundary-layer theory*. Springer.

Schofield, W. and Logan, E. (1990). Turbulent shear flow over surface mounted obstacles.

Sellin, R. (1978). Drag reduction in sewers: First results from a permanent installation. *Journal of Hydraulic Research*, 16(4):357–371.

Senturk, U. and Smits, A. J. (2019). Roughness effects in laminar pipe flow. *arXiv preprint arXiv:1905.12479*.

Shaban, S., Azad, M., Trivedi, J., and Ghaemi, S. (2018). Investigation of near-wall turbulence in relation to polymer rheology. *Physics of Fluids*, 30(12):125111.

Shah, M. S., Joshi, J. B., Kalsi, A. S., Prasad, C., and Shukla, D. S. (2012). Analysis of flow through an orifice meter: Cfd simulation. *Chemical engineering science*, 71:300–309.

Shih, T.-H., Liou, W. W., Shabbir, A., Yang, Z., and Zhu, J. (1994). A new k-epsilon eddy viscosity model for high reynolds number turbulent flows: Model development and validation.

Sifferman, T. R., Kemp, L., and Chilingarian, G. V. (1989). Flow rate measurements. In *Developments in Petroleum Science*, volume 19, pages 13–59. Elsevier.

Simpson, R. L. (1989). Turbulent boundary-layer separation. *Annual Review of Fluid Mechanics*, 21(1):205–232.

Smits, A., Ding, L., and Van Buren, T. (2019). Flow over a square bar roughness. In *Proc. Turbulence and Shear Flow Phenomena*, volume 11.

Smits, A. J., Young, S., and Bradshaw, P. (1979). The effect of short regions of high surface curvature on turbulent boundary layers. *Journal of fluid mechanics*, 94(2):209–242.

Sureshkumar, R., Beris, A. N., and Handler, R. A. (1997). Direct numerical simulation of the turbulent channel flow of a polymer solution. *Physics of Fluids*, 9(3):743–755.

Takeuchi, H. (2012). Demonstration test of energy conservation of central air conditioning system at the sapporo city office building. *Synthesiology English edition*, 4(3):136–143.

Toms, B. A. (1948). Some observations on the flow of linear polymer solutions through straight tubes at large reynolds numbers. *Proc. of In. Cong. On Rheology, 1948*, 135.

Tsukahara, T., Kawase, T., and Kawaguchi, Y. (2011). Dns of viscoelastic turbulent channel flow with rectangular orifice at low reynolds number. *International Journal of Heat and Fluid Flow*, 32(3):529–538.

Tsukahara, T., Kawase, T., and Kawaguchi, Y. (2013a). Dns on turbulent heat transfer of viscoelastic fluid flow in a plane channel with transverse rectangular orifices. *Progress in Computational Fluid Dynamics, an International Journal 03*, 13(3-4):212–223.

Tsukahara, T., Motozawa, M., Tsurumi, D., and Kawaguchi, Y. (2013b). Piv and dns analyses of viscoelastic turbulent flows behind a rectangular orifice. *International Journal of Heat and Fluid Flow*, 41:66–79.

Tsukahara, T., Tanabe, M., and Kawaguchi, Y. (2014). Effect of fluid viscoelasticity on turbulence and large-scale vortices behind wall-mounted plates. *Advances in Mechanical Engineering*, 6:823138.

Van Buren, T., Hellström, L., and Smits, A. (2019). Turbulent pipe flow response to rough-to-smooth step change in roughness: flow structure. In *Proc. Turbulence and Shear Flow Phenomena*, volume 11.

Van Buren, T., Marusic, I., and Smits, A. J. (2017). Turbulent pipe flow response to wall changes targeting specific azimuthal modes. *gen*, 1000:3.

Van Den Bergh, S., Hart, R., Jelle, B. P., and Gustavsen, A. (2013). Window spacers and edge seals in insulating glass units: A state-of-the-art review and future perspectives. *Energy and Buildings*, 58:263–280.

Verma, S. and Hemmati, A. (2020). Performance of overset mesh in modeling the wake of sharp-edge bodies. *Computation*, 8(3):66.

Versteeg, H. K. and Malalasekera, W. (2007). *An introduction to computational fluid dynamics: the finite volume method*. Pearson education.

Vogel, J. and Eaton, J. (1985). Combined heat transfer and fluid dynamic measurements downstream of a backward-facing step.

Vold, M. (2017). Three-dimensional numerical modeling of water flow in a rock-blasted tunnel.

Von Kármán, T. (1963). *Aerodynamics*. McGraw-Hill paperbacks : Science, mathematics and engineering. McGraw-Hill.

Wang, F. and Lam, K. M. (2019). Geometry effects on mean wake topology and large-scale coherent structures of wall-mounted prisms. *Physics of Fluids*, 31(12).

Wang, X., Hao, Z., Zhang, J.-X., and Tan, S. (2014). Flow around two tandem square cylinders near a plane wall. *Experiments in Fluids*, 55(10):1818.

Warner Jr, H. R. (1972). Kinetic theory and rheology of dilute suspensions of finitely extendible dumbbells. *Industrial & Engineering Chemistry Fundamentals*, 11(3):379–387.

Weller, H. G., Tabor, G., Jasak, H., and Fureby, C. (1998). A tensorial approach to computational continuum mechanics using object-oriented techniques. *Computers in physics*, 12(6):620–631.

White, C., Somandepalli, V., and Mungal, M. (2004). The turbulence structure of drag-reduced boundary layer flow. *Experiments in fluids*, 36(1):62–69.

White, C. M. and Mungal, M. G. (2008). Mechanics and prediction of turbulent drag reduction with polymer additives. *Annu. Rev. Fluid Mech.*, 40:235–256.

Wilcox, D. C. et al. (1998a). *Turbulence modeling for CFD*, volume 2. DCW industries La Canada, CA.

Wilcox, D. C. et al. (1998b). *Turbulence modeling for CFD*, volume 2. DCW industries La Canada, CA.

Xiong, Y. L., Bruneau, C.-H., and Kellay, H. (2013). A numerical study of two dimensional flows past a bluff body for dilute polymer solutions. *Journal of Non-Newtonian Fluid Mechanics*, 196:8–26.

Yamagata, T., Ito, A., Sato, Y., and Fujisawa, N. (2014). Experimental and numerical studies on mass transfer characteristics behind an orifice in a circular pipe for application to pipe-wall thinning. *Experimental thermal and fluid science*, 52:239–247.

Yin, G., Andersen, M., and Ong, M. C. (2020). Numerical simulations of flow around two tandem wall-mounted structures at high reynolds numbers. *Applied Ocean Research*, 99:102124.

Zagarola, M. V. and Smits, A. J. (1998). Mean-flow scaling of turbulent pipe flow. *Journal of Fluid Mechanics*, 373:33–79.